Solutes and Ions
at Biological Interfaces:
Interactions and Kinetics

Dissertation

zur Erlangung des akademischen Grades eines Doktors der
Naturwissenschaften (Dr. rer. nat.)

am Fachbereich Physik der Freien Universität Berlin

vorgelegt von
Amanuel Wolde-Kidan

Berlin, 2021

Contents

Chapter 1

Introduction

The term interfacial science can be interpreted two-fold, either as the study of properties and interactions of certain interfaces or as the combination of methods from different branches of science, such as biology and physics, meeting at one common interface. This thesis, studying the interactions of solutes and ions with biological interfaces using a physics approach, thus encapsulates both meanings of the word interfacial science.
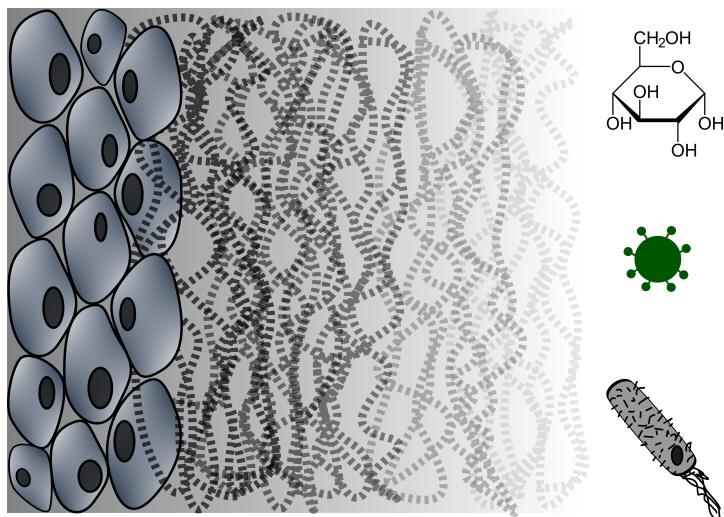
Figure 1.1: Schematic depiction of nutrients such as glucose or pathogens like virions or bacteria, penetrating a mucous membrane. The first interface the diffusors have to overcome is mucus, an example for a biological hydrogel. Subsequently, the underlying epithelial cells are the next barrier to overcome by the diffusors. Since cellular membranes consist of lipid bilayers, interactions of the diffusors with the lipid interface are crucially determining the penetration process.

Biological interfaces are ubiquitously encountered when analyzing processes where organisms interact with each other or with their environment. During the uptake of nutrients (or pathogens for that matter) the compound of interest has to pass several layers of biological barriers. Regardless of it being a virus that penetrates the human lung or a glucose molecule that is being absorbed by the small intestine, interactions of these compounds with biological interfaces are the fundamental events governing the

penetration process. As depicted in fig. 1.1, the first layer these diffusors have to pass commonly consists of mucus, which lines almost all epithelial tissues and is the most abundant biological hydrogel [1]. It acts as a selective diffusion barrier, which is one of the reasons why the study of hydrogels, being the topic of Chapter 2 of this thesis, is of significant interest not only for engineering and industrial applications [2, 3] but also in the medical context [4, 5].

If the diffusor successfully passed the mucus barrier, it either has to pass the intercellular space between, or directly through the cells of the underlying epithelial tissues (cf. fig. 1.1). In both scenarios interactions of the compounds with the cellular membranes of the epithelial cells are of importance, with cellular membranes being the prime example of a lipid bilayer interface. Phosphatidylcholine (PC) is among the most predominant lipid types in cellular membranes [6] and, due to its zwitterionic but net neutral headgroup structure, displays a range of characteristic electrostatic properties. To this day, the interactions of the PC-lipid headgroup with ions, as well as the repulsive lipid-lipid interactions in water termed *hydration repulsion* [7, 8] are phenomena which are not fully understood. This is why the study of PC-lipid bilayer-bilayer interactions, covered in Chapter 3, and lipid-ion interactions, the topic of Chapter 4 of this thesis, are of broad interest in the physical chemistry community.

The following three Chapters of this thesis are concerned with interactions between solutes and interfaces, and analyze in detail how these interactions are influenced by the specific compositions of the interface or the solutes. Two of the most common biological interfaces are studied, hydrogels and lipid bilayers, both also being fundamental penetration barriers.

1.1 Penetration through Hydrogels

Hydrogels are ubiquitous not only in biological systems in the form of mucus or biofilms [1, 9] but also in the realm of industrial applications as lubricants or vehicles in drug delivery [5]. The key component for all hydrogels is a cross-linked hydrophilic polymeric substance which takes up water, thus providing the characteristic hydrogel properties. In the biological context, the penetration of compounds through hydrogels is of particular interest in processes like infections with pathogens [10], uptake of nutrients [11] or cervical passage of sperm cells [12]. The barrier function of mucus can be broadly distinguished into two different mechanisms, a *size-filtering* and an *interaction-filtering* type [13]. As the name suggests the former mechanism leads to selective permeability based on the diffusor size, while the latter is governed by mucus-diffusor interactions and thus allows passage based on specific diffusor properties such as charge or chemical composition [14]. *Interaction-filtering* is suggested to be the predominant way in which mucus provides its barrier function [15, 16].

From a physics point of view, the efficiency of the penetration processes is quantified by the permeability, which is for a one-dimensional penetration barrier computed as

$$\frac{1}{P(z_1, z_2)} = \int_{z_1}^{z_2} \frac{e^{\beta F(z)}}{D(z)}\, dz. \tag{1.1}$$

A detailed derivation of eq. (1.1) is shown in Chapter 2, Section 2.4.7. The permeability $P(z_1, z_2)$, where z_1 and z_2 denote the positions at the two sides of the penetration barrier so that the thickness of the interface is defined as $L := z_2 - z_1$, is a function of the diffusivity and the free energy profiles, $D(z)$ and $F(z)$ respectively. As is apparent from eq. (1.1) and as is also intuitively clear, a large diffusion constant and a low value of the free energy across the barrier, in combination with small values of L, lead to increased permeabilities. The permeability as well as the diffusivity and free energy are quantities which are determined not purely by the diffusor, but rather by the specific diffusor-barrier combination. In physics terms, selective permeability, as observed in mucus, can thus also be distinguished into either a diffusive barrier (displaying a reduced diffusivity) or an energetic barrier (with a large value of the free energy) [17–19].

The free energy profile $F(z)$ is determined by the interactions between diffusor and environment and uniquely defines the equilibrium distribution and thus the partitioning of the diffusor. For the case of a two-phase system, e.g. a layer of mucus on top of epithelial tissue, the partitioning between the two layers can be quantified by the partition coefficient K defined as

$$K = e^{-\beta \Delta F}, \tag{1.2}$$

where ΔF is the difference in the free energy between the two layers and $\beta = 1/k_{\mathrm{B}}T$ is the inverse thermal energy. A system composed of several layers, such as the one shown in fig. 1.1, can be approximated as displaying piecewise constant free energy and diffusivity profiles, which according to eq. (1.1) means that the total permeability P_{tot} is the inverse sum of the permeabilities of the individual layers

$$\frac{1}{P_{\mathrm{tot}}} = \sum_i \frac{1}{P_i} = \sum_i \frac{e^{\beta \Delta F_i}}{D_i} L_i = \sum_i \frac{L_i}{D_i K_i}, \tag{1.3}$$

where the index of the sum extends over all layers. Equations (1.1) and (1.3) show that both, the free energy difference and the diffusion constant are important for the barrier function of hydrogels.

The diffusivity profile $D(z)$, contrary to the free energy profile $F(z)$, describes the mobility of the diffusor and thus governs the temporal evolution of the distribution of diffusors $c(z, t)$. The so-called Smoluchowski equation is a generalized form of the diffusion equation which defines the diffusor distribution $c(z, t)$, it reads

$$\frac{\partial c(z, t)}{\partial t} = \frac{\partial}{\partial z} \left[D(z) e^{-\beta F(z)} \frac{\partial}{\partial z} \left(c(z, t) e^{\beta F(z)} \right) \right]. \tag{1.4}$$

Analytical solutions to eq. (1.4) exist only for limited cases, an example of which is presented in Section 2.4.2 of Chapter 2. For a specific diffusivity and free energy profile,

the solution of eq. (1.4) describes the spatial distribution of the diffusors at each point in time and in the case of a constant free energy landscape and constant diffusivity it reduces to Fick's well known second law of diffusion

$$\frac{\partial c(z,t)}{\partial t} = D\frac{\partial^2 c(z,t)}{\partial z^2}.$$

(1.5)

Equation (1.5) has been known for two centuries and was originally derived by Joseph Fourier to describe the flow of heat in materials [20]. As the name "Fick's law of diffusion" suggests, Adolf Fick was the first to apply eq. (1.5) to the phenomenon of diffusion, about thirty years after the initial derivation by Fourier [21]. Only more than fifty years later did Marian Smoluchowski derive the generalized version of the diffusion equation in the form of eq. (1.4) [22].

The numerical solution of the Smoluchowski equation (1.4) is the basis of Chapter 2, in which the penetration behavior of fluorescently labeled dextran molecules into polyethylene-glycol (PEG) based hydrogels is studied. Based on non-normalized concentration profiles measured by our experimental collaborators from the Haag group (FU Berlin), eq. (1.4) is numerically inverted to obtain the free energy and diffusivity profiles, which describe the diffusion process best. Chapter 2 thus showcases a novel method for the extraction of values for the free energy and diffusion constants of diffusors in hydrogels based on arbitrarily normalized concentration data. The partition coefficients obtained from the free energy differences according to eq. (1.2) are subsequently modeled theoretically in Section 2.2.3 by employing an elastic free volume model, which additionally incorporates hydrogel and dextran flexibility. The model results reveal a broad pore-size distribution of the hydrogels and suggest that larger pores dominate the partitioning process.

1.2 Interactions between Lipid Membranes

In addition to their abundance in biological systems, lipids, just like hydrogels, are important vehicles for drug delivery because of their lipophilicity and high biocompatibility [23]. Lipid molecules, driven by hydrophobic forces due to their amphiphilic nature, spontaneously form bilayers in water. These lipid bilayers behave as cohesive liquids and display phase transitions as a function of temperature and hydration [24, 25]. Cellular membranes are composed of lipid bilayers and contain a plethora of different lipid types, with phosphatidylcholine (PC) lipids being the most predominant ones [6]. The net-neutral zwitterionic headgroup of PC-lipids shown in fig. 1.2 is their defining component and determines interactions with the surrounding water or solute molecules. The distribution of the negative and positive charge gives rise to the specific electrostatic properties of PC-lipids. In a study related to this thesis [26] (Ref. [vi]), we, together with experimental collaborators from the Bonn group (Max Planck Institute for Polymer Research, Mainz), investigated the importance of the positioning of the headgroup charges on the induced water orientation. A reversal of the head group

charges has indeed been observed to significantly change the properties of bilayers composed of these inverted PC-lipid molecules, leading to potentially new applications for drug delivery [27].
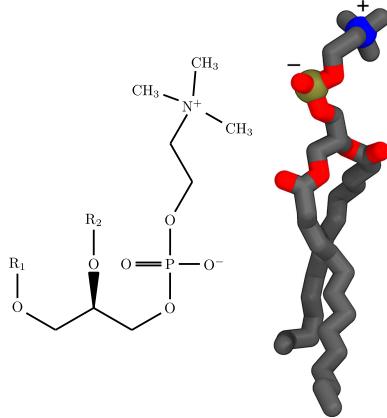
Figure 1.2: Chemical composition of the phosphatidylcholine (PC) lipid headgroup and a screenshot from atomistic molecular dynamics simulations. The positively charged choline group protrudes further into the water than the negatively charged phosphate, which is located closer to the carbon tails of the lipid molecule.

PC-lipid bilayers and other biological colloids repel each other at short distances in water in a characteristic fashion. This phenomenon is termed *hydration repulsion* [28, 29] and is defined by an exponential decay of the interaction pressure Π with the separation of the surfaces D_w according to

$$\Pi(D_w) = \Pi_0 \cdot e^{-D_w/\lambda}, \tag{1.6}$$

where Π_0 denotes the pressure amplitude and λ is the decay length. The parameters Π_0 and λ are determined by the specific biological system and have, for lipids, been shown to even depend on the phase of the lipid bilayer [30]. Even-though exponentially decaying interaction pressures between lipid surfaces have been observed almost fifty years ago by Adrian Parsegian [31], there are still many open questions regarding this phenomenon until today. The repulsion is, however, fundamental for the correct functioning of lipid membranes in water and prevents unwanted fusion of cellular membranes [32].

Chapter 3 is concerned with the influence of small polar co-solutes, also termed compatible solutes, on the *hydration repulsion* and specifically investigates the importance of their properties and interactions with the lipid interface. All solutes are observed to consistently increase the interaction pressure of eq. (1.6) at the same separation D_w, or, in other words, increase the separation and thus the hydration level at the same interaction pressure Π. This showcases an important function that compatible solutes fulfil in biological systems, namely combating high osmotic pressures [33]. Especially in situations of high pressures, sufficient hydration of lipid surfaces is important, since

otherwise unwanted phase transitions occur. This is also the reason for altered barrier functions at low hydration, which have been observed for the stratum corneum [34], the outermost layer of the human skin, being mainly composed of lipids [35].

For charged solutes and ions, the interaction with lipid surfaces is usually studied in electrophoresis measurements [36]. In these experiments, lipid vesicles are placed in a solution containing the co-solute of interest. The velocity of the vesicles in response to an externally applied electric field then provides information about their effective surface charge due to co-solute adsorption. The so-called ζ-potential approximates the surface potential, thus quantifying the adsorption process and is computed as

$$\zeta = \frac{\eta u}{\varepsilon \varepsilon_0 E},\tag{1.7}$$

where E is the applied field strength, u is the vesicle velocity, ε_0 is the vacuum permittivity and η and ε are the viscosity and the relative dielectric constant of the solution respectively.

In Chapter 4 of this thesis, ζ-potentials are computed from atomistic molecular dynamics simulations of lipid bilayers in different salt solutions according to eq. (1.7) and the obtained results are compared to experimental data from the literature. For all salts, the ζ-potentials from simulations are significantly more positive than the corresponding results from experiments. In analogy to previous studies performed on hydrophobic surfaces [37] this disagreement is explained with the presence of minute amounts of anionic surface active impurities in the experimental setups. An electrostatic continuum model of the simulation data developed in Section 4.2.2 of this thesis accounts for impurities and indeed leads to ζ-potentials that agree nicely with experimental values.

Chapter 2

Framework for Studying Hydrogel Permeabilities based on Time Resolved Penetration Profiles

Bibliographic information:
Parts of this Chapter have been published under Ref. [i].

The permeability of diffusors into and through hydrogels has been studied in several contexts, ranging from industrial applications [3, 4] to specific biological questions regarding biofilms [9], the extracellular matrix [38] or mucus [39]. The study of hydrogels has important medical implications, e.g. as a means for tissue engineering or drug delivery [4]. Mucus, which is the most common biological hydrogel, lines the epithelial tissues of many organs, such as the respiratory, gastrointestinal or urogenital tracts. It is mainly composed of mucins, glycoproteins of varying lengths which take up water, giving mucus its hydrogel nature, and additional components such as enzymes and ions [40]. In addition to its function as a permeation barrier for harmful pathogens, mucus, or more specifically the constituting mucins, are relevant in the cell signaling context and presumably also play a role in the development of cancer [41]. The main context in which mucus is studied, however, is the penetration of pathogens, e.g. a virus entering the respiratory tract, or non-pathogens, e.g. nutrients being absorbed through the mucosa of the small intestine [10]. As mentioned in Chapter 1, one typically distinguishes steric *size-filtering* mechanisms from *interaction-filtering* mechanisms [14, 39], the latter presumably play a major role in the defense of organisms against pathogens since they allow for precise regulation of the passage of wanted and unwanted particles and molecules [15, 16]. A completely different mechanism consists of advective transport of pathogens away from the epithelium through mucus shedding [42]. Recent reports indicate a wider prevalence for the mechanism of *interaction-filtering*, making it the major contribution to the biological defense against pathogens [15, 43–46].

Penetration processes in mucus are commonly studied by means of single particle tracking [39, 47] but also in terms of ensemble averages over many diffusors, e.g. using fluorescence microscopy [48, 49]. In terms of a continuum description, the diffusion process of a specific probe is completely determined by its free energy and mobility landscape across the hydrogel. Extraction of these quantities from experimental data

allows for detailed analysis and prediction of the penetration process as a function of different diffusor and hydrogel materials. Traditionally, experiments focus either on the determination of the diffusor mobility inside the hydrogel [14, 16] or on the partitioning between the gel and the solution [50]. However, for assessing the efficacy of permeation, both the diffusion constant, and the energy jump across the barrier (manifested in terms of the partition coefficient) are of major importance.

This Chapter is concerned with synthetic hydrogels, provided by our experimental collaborators from the Haag group (FU Berlin), that consist of polyethylene-glycol (PEG) linkers of different molecular masses which are permanently cross-linked by hyperbranched polyglycerol (hPG) hubs [3]. Such synthetic hydrogels can be regarded as simple models for mucus, since they display size-dependent particle permeabilities [14, 51], similar to mucus. As diffusing particles our collaborators employ fluorescently labelled dextran molecules of varying sizes. When using confocal laser-scanning fluorescence microscopy to investigate particle penetration into hydrogels, the sample can be oriented such that the hydrogel-bulk interface is either parallel [16] or perpendicular [52] to the optical axis, which makes no significant difference from a scanning perspective. However, for laterally extended samples like cell cultures that grow on a substrate, the parallel alignment causes the light path to span substantially larger distances, making this setup more prone to distortions in the imaging process. A perpendicular alignment, as employed by our experimental collaborators and sketched in fig. 2.1, is therefore preferable for biological samples [52] and is also compatible with future extensions of such penetration assays to mucus-producing cell cultures.

This Chapter studies the filtering function of hydrogels by theoretical analysis of time-resolved concentration profiles of the labelled dextran molecules as they penetrate into the hydrogel, obtained by our experimental collaborators from the Haag group. The employed numerical method allows for simultaneous extraction of free-energy and diffusivity profiles from relative concentration profiles at different times and is a significant extension of earlier methods [17, 18, 53] (Ref. [iv]), since it requires in the form presented in this Chapter only raw non-normalized fluorescence intensity data as input. This circumvents the complicated and at times impossible conversion of measured intensity data into an actual concentration of diffusors. Based on the exemplary application shown in this Chapter, this method could be used in a wide range of different setups, facilitating the study of penetration into hydrogels. As a check on the robustness of the method, the extracted dextran bulk diffusivities are shown to agree well with fluorescence-correlation spectroscopy (FCS) data that are obtained separately by our collaborators from the Gradzielski group (TU Berlin). The obtained particle free-energies and diffusivities inside the hydrogel are shown to obey empirical scaling laws as a function of the dextran mass. The dextran free-energy inside the hydrogel is described by a free-volume model based on repulsive steric interactions between the dextran molecules and the hydrogel linkers, which includes dextran as well as hydrogel linker flexibility. This model constitutes a modified *size-filtering* mechanism for repulsive particle-hydrogel interactions, according to which particle penetration into hydrogel pores is assisted by the elastic widening of pores and the elastic shrinking
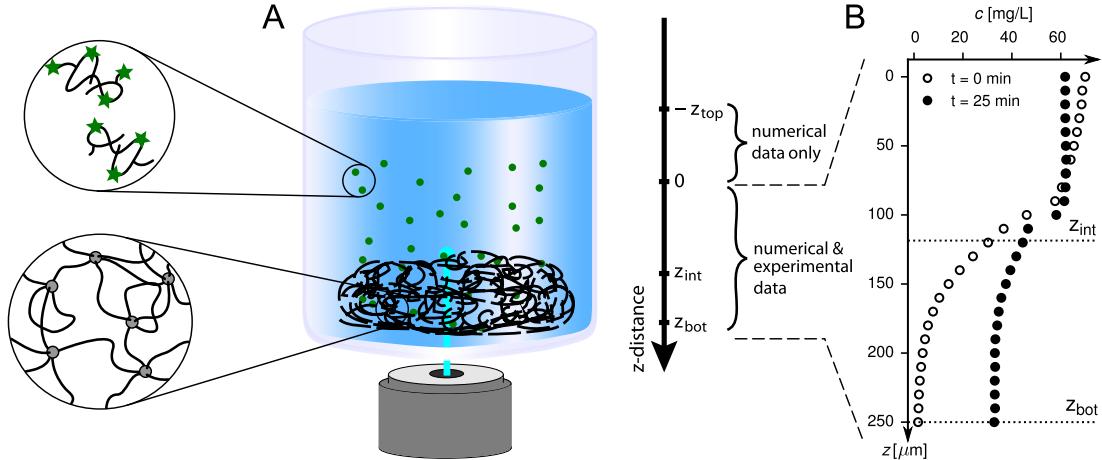
Figure 2.1: A: Schematic drawing of the experimental setup employed by our collaborators. Concentration profiles of fluorescently labeled dextran molecules (green) are measured as they penetrate from the bulk solution (blue) into the hydrogel (black). The origin of the z-axis is positioned such that experimentally measured profiles range from $z = 0$ to $z = z_{bot}$. The hydrogel-bulk solution interface is located at $z = z_{int}$. In the range from $z = -z_{top}$ to $z = 0$ only numerically determined concentration profiles are available. B: Exemplary experimental concentration profiles for two different penetration times for $M_{dex} = 4$ kDa dextran diffusing into the *hPG-G10* hydrogel, positions of the hydrogel-bulk solution interface z_{int} and the hydrogel-glass bottom interface z_{bot} are indicated.

of dextran molecules, and matches the extracted particle free-energies in the hydrogel quantitatively. The model furthermore suggests that the hydrogel mesh size distribution is rather broad and that particle penetration is dominated by the fraction of large pores in the hydrogel.

2.1 Methodology

2.1.1 Sample Preparation

Our collaborators from the Haag group formed the hydrogel by cross-linking end-functionalized polyethylene glycol-bicyclo[6.1.0] non-4-yne (PEG-BCN) linkers with hyperbranched polyglycerol azide (hPG-N$_3$) hubs via strain-promoted azide-alkyne cycloaddition (SPAAC) [3, 54]. The linkers and hubs were mixed in a ration of 3:1. Two different sizes of PEG-BCN linkers are employed, having a molecular weight of either $M_{PEG} = 6$ or $M_{PEG} = 10$ kDa, the hydrogels are denoted as *hPG-G6* and *hPG-G10*, respectively. Even though both hydrogel solutions are adjusted to have the same mass concentration, after drying and re-swelling on the glass substrate volumes of the formed hydrogels differed. They were measured as $V_{tot}^{hPG-G6} = 0.42 \pm 0.03$ μL and

$V_{\text{tot}}^{\text{hPG-G10}} = 0.31 \pm 0.04 \ \mu$L for *hPG-G6* and *hPG-G10*, respectively. This results in a final hydrogel concentration of 9 wt% (≈ 90 mg/mL) for *hPG-G6* and 12 wt% (≈ 120 mg/mL) for *hPG-G10*.

The Haag group used dextrans conjugated with the dye fluorescein isothiocyanate (FITC), which are obtained from *Sigma-Aldrich* as d4-FITC, d10-FITC, d20-FITC, d40-FITC and d70-FITC, the number stating the molecular weight in kDa of the commercial product.

2.1.2 Mean Mesh Size Estimate

Assuming an idealized cubic hydrogel network structure, the mean mesh size can be easily estimated. The length of a cubic unit cell $l_{0,\text{ideal}}$ follows from the total gel volume V_{tot} and the total number of hPG hubs $n_{\text{hPG}}^{\text{tot}}$ in mol as

$$l_{0,\text{ideal}} = \sqrt[3]{\frac{V_{\text{tot}}}{n_{\text{hPG}}^{\text{tot}} N_{\text{A}}}}, \tag{2.1}$$

where $n_{\text{hPG}}^{\text{tot}}$ is the total number of hPG hubs and N_{A} is the Avogadro constant. The total volumes for the re-hydrated gels are $V_{\text{tot}}^{\text{hPG-G6}} = 0.42 \ \mu$L and $V_{\text{tot}}^{\text{hPG-G10}} = 0.31 \ \mu$L. This results in rough estimates for the mesh size of $l_{0,\text{ideal}}^{\text{hPG-G6}} = 7.1$ nm and $l_{0,\text{ideal}}^{\text{hPG-G10}} = 7.5$ nm, which shows that even though PEG linkers of significantly different masses were used, the mesh sizes of the two gels differ only slightly.

In deriving eq. (2.1) one assumes an ideal hydrogel pore connectivity that corresponds to a perfect cubic lattice. There is no reason why the hydrogel should consist of a perfect cubic lattice, on the contrary, entropy favors a disordered network topology. For cubic pores with lower connectivity, fig. 2.2 illustrates how the pore size l_0 can increase for a fixed PEG end-to-end distance R_{PEG}. Thus, except for the case of an ideal cubic lattice, the pore size l_0 will be larger than the estimate of eq. (2.1), as indeed suggested by our elastic free-volume model.

2.1.3 Penetration Assay

After preparation of the hydrogel solutions and the dextrans (see above), penetration assays were performed by our collaborators from the Haag group with five different dextran solutions and two different gels. For this, a volume of 35 μL of the dextran solution (0.07 mg/mL for all dextrans) was placed on top of the hydrogel in a cylindrical cavity, which was then used to measure the penetration process with a confocal laser scanning microscope (CLSM) (see fig. 2.1). This fixes the total length from the bottom of the glass dish at $z = z_{\text{bot}}$ to the air-water interface at $z = -z_{\text{top}}$, where $z = 0$ corresponds to the end of the measurement region (see fig. 2.1A). The total length of the solution is thus $z_{\text{tot}} = z_{\text{top}} + z_{\text{bot}} = 1780 \ \mu$m. The individual contributions to z_{tot} vary, due to different gel thicknesses, changing the extent of the measured region, ranging from $z = 0$ to $z = z_{\text{bot}}$ (cf. also fig. 2.1A).
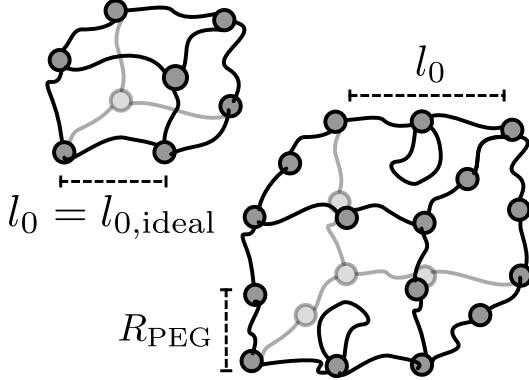
Figure 2.2: A cubic pore with lower connectivity to the right, containing two instead of one PEG linker per edge, leads to an effectively larger unit cell length l_0 at the same PEG end-to-end distance R_{PEG}. Only for a perfect cubic lattice to the left, is the estimate of eq. (2.1) valid and $l_0 = l_{0,\mathrm{ideal}} = R_{\mathrm{PEG}}$.

About 10 seconds after the application of the dextran solution, the spatial distribution of the FITC-based fluorescence intensity is measured using a z-stack that starts 30 μm below and ends 410 μm above the glass-hydrogel interface (with 10 μm increments). The recorded intensities are afterwards truncated to probe the spatial FITC distribution within the hydrogel starting from the glass bottom (located at z_{bot}) and extending about 100 μm into the bulk solution, away from the gel-water interface located at $z = z_{\mathrm{int}}$ (cf. fig. 2.1A). For the $M_{\mathrm{dex}} = 4$ kDa to the $M_{\mathrm{dex}} = 40$ kDa dextrans, one z-stack is recorded every $\Delta t = 10$ s, yielding time-resolved FITC distributions following the penetration of the dextran molecules into the hydrogel network over time. For the $M_{\mathrm{dex}} = 70$ kDa dextrans a period of $\Delta t = 30$ s is used instead, in order to account for the much smaller diffusion coefficient of the larger dextran molecules. The employed temporal resolutions can be easily estimated to be larger than time scales on which effects of anomalous diffusion are present: For diffusion over lengths scales larger than the mesh size of the hydrogel, normal diffusion is expected. An upper bound for the corresponding crossover timescale can be estimated as $\tau = l_0^2/D_{\mathrm{gel}}$, where $l_0 = 24$ nm is an upper estimate for the hydrogel mesh size and $D_{\mathrm{gel}} = 0.15$ μm^2/s is the smallest obtained diffusion constant in the hydrogel (see below for explicit results). The resulting value of $\tau \approx 0.2$ ms, beyond which normal diffusion is expected, is several orders of magnitude lower than the experimental temporal resolution. Thus anomalous diffusion cannot be observed in the experimental data and the normal diffusion equation that is used to model the time-dependent experimental concentration profiles should be valid.

For all dextran types our collaborators from the Haag group performed measurements at least three times with total measurement times of about 30 minutes, with the exception of the $M_{\mathrm{dex}} = 70$ kDa dextrans. Here only one measurement is performed for each gel but with a longer recording time of about 1 hour.

2.1.4 Numerical Model and Discretization

Extending a previously introduced method [17, 18, 53] (Ref. [iv]), spatially resolved diffusivity and free-energy profiles are estimated from experimentally measured concentration profiles. Numerical profiles are computed by discretizing the entire experimental setup from the glass bottom of the substrate to the air-water interface (z_{bot} to $-z_{\text{top}}$ in fig. 2.1A). In the regime where concentration profiles are measured ($z = 0$ to $z = z_{\text{bot}}$), the experimental resolution is used as the numerical discretization width $\Delta z = 10$ μm. For the range without experimental data ($z = 0$ to $z = -z_{\text{top}}$) in total six bins are employed. Two of those bins are spaced with $\Delta z = 10$ μm, for the other four bins, discretization spacings between $\Delta z = 300$ - 400 μm are used, depending on the z-length measured in the respective experiment z_{bot}. The z-dimension of the total system is the same for all experiments and given as $z_{\text{tot}} = z_{\text{top}} + z_{\text{bot}} = 1780$ μm. The experimentally measured region always extends from the glass bottom through the gel and at least 100 μm into the bulk solution, away from the hydrogel-bulk interface, which leads to values of $z_{\text{bot}} \approx 300$ μm, depending on the exact thickness of the hydrogel in the respective measurement.

The numerical optimization problem is given by the cost function, which is defined as

$$\sigma^2(D, F, \vec{f}) := \frac{1}{N \cdot M} \sum_{j=1}^{\text{N}} \sum_{i=1}^{\text{M}} \left[c_i^{\text{num}}(t_j) - f_{\text{j}} \cdot c_i^{\text{exp}}(t_j) \right]^2, \tag{2.2}$$

with N the total number of experimental profiles, M the total number of experimental data points per concentration profile and $\sigma^2(D, F, \vec{f})$ being the mean squared deviation between the experimental and numerical profiles. The diffusivity profile $D = D(z)$, the free-energy landscape $F = F(z)$ and the vector containing all scaling factors $\vec{f} = (f_1, ..., f_j, ..., f_N)$ (see below for details) are all optimized to find the minimal value of σ^2. This non-linear regression is performed using the trust region method implemented in python's *scipy* package [55].

The numerical profiles

$$\vec{c}_{\text{num}}(t_{\text{j}}) = (c_1^{\text{num}}(t_{\text{j}}), ..., c_i^{\text{num}}(t_{\text{j}}), ..., c_M^{\text{num}}(t_{\text{j}}))^T$$

are computed from the diffusivity and free-energy profiles as

$$\vec{c}_{\text{num}}(t_{\text{j}}) = e^{Wt_{\text{j}}} \cdot \vec{c}_{\text{init}}, \tag{2.3}$$

where the rate matrix $W(D, F)$ is defined as

$$W_{i,k} = \frac{D_i + D_k}{2\Delta z^2} e^{-\frac{F_i - F_k}{2k_{\text{B}}T}}, \quad \text{with} \quad k = i \pm 1$$

in analogy to previous studies [17]. Numerical profiles at time t_j depend on the initial profile $\vec{c}_{\text{init}}$ at $t = 0$, which is determined as explained below.

The numerically computed profiles are fitted to the re-scaled experimental profiles $\vec{c}_{exp}(t_j)$ at time $t_j > 0$. The scaling factors $\vec{f}$ are obtained simultaneously from the fitting procedure and correct drifts in the experimentally measured fluorescence intensity profiles (see Section 2.4.1 of the Appendix to this Chapter). As a check, the numerical model is compared to the analytical solution for a model with piece-wise constant values of the diffusivity and free-energy in the respective regions. Results from the numerical model agree perfectly with those from the analytical solution (see Section 2.4.2 of the Appendix).

2.1.5 Construction of the Initial Concentration Profile

The initial profile $\vec{c}_{init}$, used for the computation of all later profiles according to eq. (2.3), needs to cover the entire computational domain and is generated by extending the first experimentally measured profile $\vec{c}_{exp}(t = 0)$ (ranging from $z = z_{bot}$ to $z = 0$) into the bulk regime (from $z = 0$ to $z = -z_{top}$, cf. fig. 2.1A). The value $t = 0$ is defined as the time of the first measurement, which is performed approximately 10 seconds after application of the dextran solution onto the gel-loaded substrate. For the spatial extension of the profile, a constant initial concentration is assumed in the bulk, the value of which is taken as the experimentally measured value furthest into the bulk $c_0 := c_1^{exp}(t = 0)$ at $z = 0$. This leads to the following expression used for the initial profile

$$c_i^{init} := \begin{cases} c_0, & \text{if } -z_{top} \leq z_i \leq 0 \\ c_i^{exp}(t = 0), & \text{if } 0 < z_i \leq z_{bot} \end{cases} \tag{2.4}$$

which by construction is continuous at $z = 0$. The initial profiles used for the fit procedure are shown for their respective measurements in fig. 2.3B and F as black lines. In order to obtain concentration profiles in physical units, the first measured value furthest into the bulk is set equal to the applied dextran bulk concentration of $c_0 = 70$ mg/L.

2.1.6 Free Energy and Diffusivity Profiles

Since the experimental system consists of two regions, namely the hydrogel and the bulk solution, and in order to reduce the number of parameters of the numerical model to avoid overfitting, sigmoidal profiles for the diffusivity $D(z)$ and free-energy $F(z)$ are employed, which transition continuously from the value in the bulk solution to their values in the hydrogel. This sigmoidal shape is modeled using the following expressions

$$D(z) = \frac{D_{sol} + D_{gel}}{2} - \frac{D_{sol} - D_{gel}}{2} \, \text{erf}\left(\frac{z - z_{int}}{\sqrt{2}d_{int}}\right),$$

$$F(z) = \frac{\Delta F_{gel}}{2} + \frac{\Delta F_{gel}}{2} \, \text{erf}\left(\frac{z - z_{int}}{\sqrt{2}d_{int}}\right), \tag{2.5}$$

where $\mathrm{erf}(z) := 1/\sqrt{\pi} \int_{-z}^{z} e^{-z'^2} \, dz'$ is the error function. The fit parameters z_{int} and d_{int} determine the transition position and width, respectively, and are the same for the free-energy and diffusivity profiles. Since only free-energy differences carry physical meaning, the free-energy in the bulk solution is set to zero. The values of the diffusivity and free-energy in the hydrogel and in the bulk solution are thus determined by fitting the five parameters of eqs. (2.5), namely D_{gel}, ΔF_{gel}, D_{sol}, z_{int} and d_{int}, to the experimentally measured concentration profiles.

Confidence intervals for the obtained parameters of D_{sol}, D_{gel} and ΔF_{gel} are estimated by determining the parameter values that change σ by not more than 50% (for details see Section 2.4.3 of the Appendix). The error bars shown in fig. 2.5 are then obtained by averaging the confidence intervals over all measurements.

2.2 Results and Discussion

Fluorescence intensity profiles of fluorescein isothiocyanate (FITC)-labeled dextran molecules penetrating into PEG-based hydrogels obtained by our experimental collaborators from the Haag group (FU Berlin) are analyzed using the procedure explained in Section 2.1. The analysis is based on numerical solutions of the one-dimensional generalized diffusion equation [56]

$$\frac{\partial c(z,t)}{\partial t} = \frac{\partial}{\partial z}\left[D(z)e^{-\beta F(z)}\frac{\partial}{\partial z}\left(c(z,t)e^{\beta F(z)}\right)\right], \tag{2.6}$$

where $c(z,t)$ is the concentration at time t and depth z (see fig. 2.1), $D(z)$ and $F(z)$ are the spatially resolved diffusivity and free-energy profiles which the dextran molecules experience and $\beta = 1/k_{\mathrm{B}}T$ is the inverse thermal energy. While the diffusivity $D(z)$ describes the mobility of dextran molecules at position z, the free-energy profile $F(z)$ uniquely determines the equilibrium partitioning of dextran molecules. The numerical solution of eq. (2.6) provides a complete model of the penetration process into the hydrogel and at the same time allows for extraction of the diffusivity and free-energy profiles by comparison with experimentally measured concentration profiles. A direct conversion of measured fluorescence intensities into absolute concentrations is often difficult due to drifts of various kinds. The method developed here circumvents this problem and allows for in-depth analysis of arbitrarily normalized concentration profiles, as explained in Section 2.1.4. Complete profiles of free-energies and diffusivities, both in the bulk and in the PEG hydrogel, are obtained and the results for different hydrogels and dextran molecules of varying sizes will be analyzed in the following.

2.2.1 Comparing Experimental and Modeled Profiles

Figure 2.3A&E shows exemplary concentration profiles for dextran molecules with molecular masses of $M_{\mathrm{dex}} = 4$ kDa and $M_{\mathrm{dex}} = 40$ kDa penetrating into the *hPG-G10* hydrogel (see Section 2.1.1). Our experimental collaborators from the Haag group
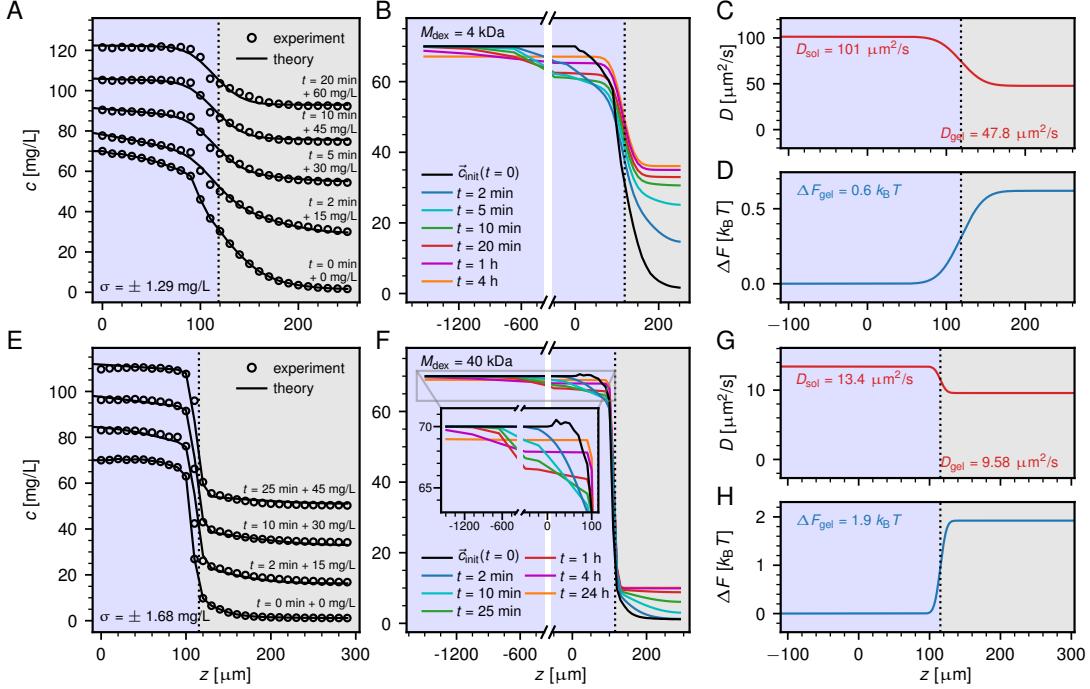
Figure 2.3: Exemplary time-dependent dextran concentration profiles from experimental measurements (circles) and numerical modeling (solid lines) for the *hPG-G10* hydrogel. Results for the smallest dextran with $M_{\mathrm{dex}} = 4$ kDa in A-D are compared to results for $M_{\mathrm{dex}} = 40$ kDa in E-H. A&E: Experimental and modeled concentration profiles agree very accurately, note that concentration profiles are shifted vertically for better visibility. The initial bulk concentration of dextran is $c_0 = 70$ mg/L. B&F: Modeled concentration profiles are presented for a wide range of penetration times. The initial profile $\vec{c}_{\mathrm{init}}$ (black line) is based on experimental data (see Section 2.1.5). C&G: Extracted diffusivity profiles, showing that the diffusivity in the hydrogel is only slightly reduced compared to the bulk solution. D&H: Extracted free-energy profiles. Significant exclusion of dextran from the hydrogel is observed, with a stronger effect for the larger dextran.

performed measurements over a total time span of about 30 minutes and recorded concentration profiles every 10 seconds, leading to a total of about 180 concentration profiles as input for the numerical extraction of the diffusivity and free-energy profiles. The first measured concentration profile at $t = 0$ min represents the start of the experiment, approximately 10 seconds after the dextran solution was applied onto the gel (see Section 2.1.3). The numerically determined concentration profiles (lines) reproduce the experimental data (data points) very accurately, as seen in fig. 2.3A&E. The deviation is estimated from the normalized sum of residuals, σ (according to eq. (2.2)) which is below 2 mg/L for both measurements. A stationary concentration profile is obtained

in the theoretical model only after 4 hours of penetration for the smaller 4 kDa dextran
(see fig. 2.3B) for the larger dextran molecule the stationary profile is reached only
after an entire day (see fig. 2.3F). These times significantly exceed the duration of the
experiments.

The diffusivity and free energy profiles in fig. 2.3C, D, G, H, reveal the intricate
details of the selective permeability of the hydrogel. The free-energy difference in the
hydrogel is positive, $\Delta F_{\text{gel}} > 0$, for both dextran sizes, indicating that the dextran is
repelled from the hydrogel. The dextran partition coefficient K_{gel} between the hydrogel
and the bulk solution is related to the change in the free-energy ΔF_{gel} as

$$K_{\text{gel}} = e^{-\beta \Delta F_{\text{gel}}}. \tag{2.7}$$

According to eq. (2.7), the obtained free-energy differences $\Delta F_{\text{gel}} = 0.6 \ k_{\text{B}}T$ and
$\Delta F_{\text{gel}} = 1.9 \ k_{\text{B}}T$, correspond to partition coefficients of about $K_{\text{gel}} \approx 1/2$ and $K_{\text{gel}} \approx$
1/7 for the smaller and the larger dextran molecules, respectively, which illustrates a
significant exclusion in particular for the larger dextran. The difference in the observed
partition coefficients showcases the apparent size dependence of the hydrogel-diffusor
repulsion. The slight difference in the broadness of the transition width observed in the
free energy and diffusivity curves for the two exemplary measurements can be explained
by sample variance, which is also apparent in the different gel thicknesses. Compared to
the partition coefficients, the diffusion constants in the hydrogel decrease only slightly
as a function of the dextran mass. This suggests that the dextran molecules are only
modestly hindered in their motion, a conclusion that will be rationalized by our elastic
free-volume model further below.

Figure 2.4 shows the temporal evolution of the average dextran concentration $\bar{c}$ in
three different regions, namely inside the gel for $z_{\text{int}} < z < z_{\text{bot}}$, in the *near solution*
for $0 < z < z_{\text{int}}$, and in the *far solution* for $-z_{\text{top}} < z < 0$ for the same data as
shown in fig. 2.3. The lines show the predictions based on the extracted diffusivity and
free-energy profiles, the circles the experimental data, which are not available in the *far
solution* range. The average concentration in the gel (black) increases monotonically
and saturates after about one hour for both dextran sizes. Note that the stationary final
concentration in the hydrogel is considerably less for the larger dextran with $M_{\text{dex}} =$
40 kDa. In contrast, the average concentration in the *far solution* saturates more
slowly and shows a slight non-monotonicity for both dextran masses (blue). This non-
monotonicity is more pronounced in the *near solution* (red) and is caused by the fact
that dextran molecules diffuse quickly into the hydrogel from the *near solution* in the
beginning of the experiment, while the replenishment from the bulk solution takes
a certain time, as also seen in the concentration profiles in fig. 2.3B&F. Very good
agreement between experiments and modeling results is observed.

2.2.2 Influence of the Dextran Size on Penetration

The same analysis as described above is performed for dextran molecules of different
molecular masses ranging from $M_{\text{dex}} = 4$ kDa to $M_{\text{dex}} = 70$ kDa penetrating PEG
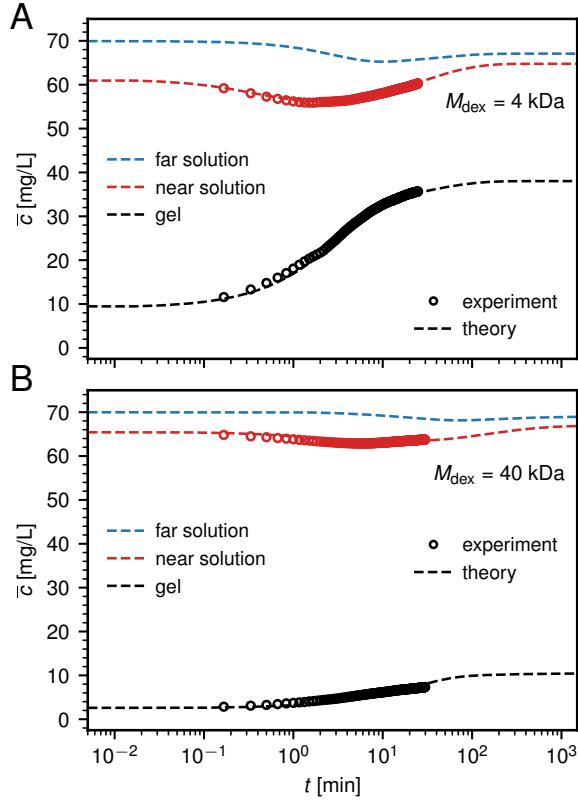
Figure 2.4: Comparison of experimental results (circles) and modeling results based on the extracted diffusivity and free-energy profiles (lines) for the average dextran concentration $\bar{c}$ over time in three different regions, the *far solution* $(-z_{\text{top}} < z < 0)$, the *near solution* $(0 < z < z_{\text{int}})$ and the gel $(z_{\text{int}} < z < z_{\text{bot}})$, see fig. 2.1. The systems are the same as shown in fig. 2.3. A non-monotonic dextran concentration is measured over time in the near and far solution regions.

hydrogels with two different linker lengths, namely *hPG-G6* with a PEG linker size of $M_{\text{PEG}} = 6$ kDa and *hPG-G10* with $M_{\text{PEG}} = 10$ kDa. Figure 2.5 shows the extracted diffusivities and free-energies, which result from averages over at least three experiments for each system, except for $M_{\text{dex}} = 70$ kDa dextran, where only one experiment was performed.

Figure 2.5A shows the obtained values for the bulk diffusivities D_{sol} as colored symbols. In general, there is no reason why a difference between the results for *hPG-G6* and *hPG-G10* is to be expected. A power law relation between the dextran mass and the diffusivity according to $D_{\text{sol}} \propto M_{\text{dex}}^{-\nu}$ is shown as straight lines for $\nu = 1$ (broken line) and for $\nu = 1/2$ (dotted line). An exponent of $\nu = 1/2$ agrees nicely with the FCS data from our collaborators (solid black triangles) as well as with literature FRAP measurements [57] (open black triangles). The value $\nu = 1/2$ follows from combin-
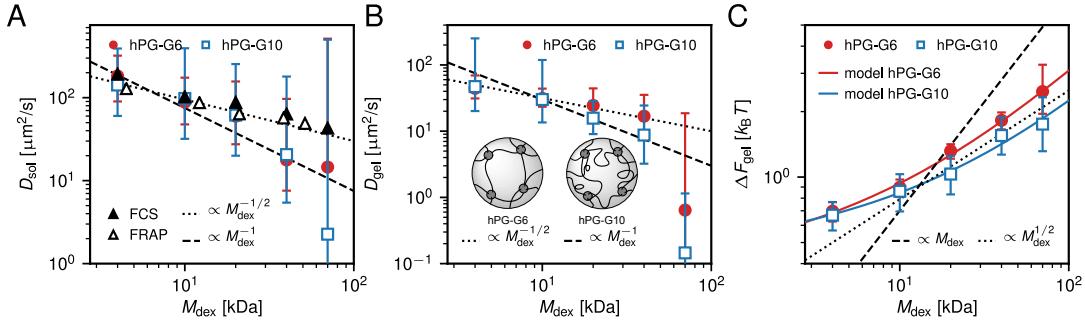
Figure 2.5: Results for the diffusivity and free-energy obtained from the experimental measurements as a function of dextran mass. A: Fitted diffusivities in the bulk solution (squares and circles) agree within the error with FCS data measured by our collaborators from the Gradzielski group (solid black triangles) and with FRAP measurements from the literature [57] (open black triangles). B: Fitted diffusivities in the hydrogel are reduced relative to the bulk values and are compared to different power laws. C: Dextran molecules are excluded from the hydrogel and $\Delta F_{gel} > 0$ for all dextran masses. For larger dextran molecules, $\Delta F_{gel}$ increases as a square root with the dextran mass. The results from the free-volume model of eq. (2.12) (continuous lines) agree nicely with the measurements. Error bars have been estimated as explained in Section 2.4.3 of the Appendix. The inset in panel B presents a schematic depiction of the two different gels. Even though the *hPG-G10* gel is composed of larger linkers, the mass density is larger than in the *hPG-G6* gel, which results in an effectively smaller pore size.

ing the Stokes-Einstein relation $D_{sol} = k_B T/6\pi\eta_w r_0$ with the scaling of the dextran hydrodynamic radius according to $r_0 \propto M_{dex}{}^\nu$ [58, 59] when assuming that the bulk solution is a theta solvent for dextran polymers [60, 61] (see Section 2.4.4 in the Appendix to this Chapter for details). The dextran hydrodynamic radii estimated from the FCS measurements of our collaborators compare well with the values reported by the supplier, see Table 2.1. The data for D_{sol} obtained from the time-dependent dextran concentration profiles show rather large uncertainties, which is due to the fact that the concentration profiles are rather insensitive to the bulk diffusivities; they are within error bars consistent with the FCS results but do not allow extraction of the power-law scaling with any reasonable confidence.

Values for the diffusion constant in the hydrogel D_{gel} are compared to power laws with exponents $\nu = 1/2$ and $\nu = 1$ in fig. 2.5B. The difference of the diffusion constants between the two different hydrogels is within the error bars, which reflects the fact that the estimated mean hydrogel mesh-sizes, using a very simplistic hydrogel network model with a perfect cubic structure, are $l_{0,ideal}^{hPG-G6} = 7.1$ nm and $l_{0,ideal}^{hPG-G10} = 7.5$ nm (see Section 2.1.2) and thus quite similar to each other. It is to be noted that for $M_{dex} \leq$ 20 kDa, the estimated mesh sizes are larger than twice the dextran hydrodynamic radii from Table 2.1, which would not suggest any dramatic confinement effect on the

Table 2.1: Dextran hydrodynamic radius r_0 as reported by the supplier, in comparison to the estimated hydrodynamic radius r_{FCS} based on the FCS measurements performed by the Gradzielski group using the Stokes-Einstein relation and the viscosity of water as $\eta_{\text{w}} = 0.8 \cdot 10^{-3}$ Pas.

M_{dex}	r_0	r_{FCS}
4 kDa	1.4 nm	1.5 nm
10 kDa	2.3 nm	2.7 nm
20 kDa	3.3 nm	3.2 nm
40 kDa	4.5 nm	4.3 nm
70 kDa	6.0 nm	6.4 nm

diffusion constant [62]. Interestingly, for the data where $M_{\text{dex}} \gtrsim 20$ kDa, the hydrogel with the larger linker length (*hPG-G10*), which has a slightly larger mesh size, is seen to reduce the diffusion constant slightly more, which at first sight is counterintuitive. This finding can be rationalized by the fact that the *hPG-G10* gel has a higher mass density compared to the *hPG-G6* gel (see Section 2.1.1), and thus the effective pore size is presumably substantially smaller. This is schematically illustrated in the inset in fig. 2.5B. A diffusivity scaling with an exponent $\nu = 1$, which describes the data for *hPG-G10* slightly better, could be rationalized by screened hydrodynamic interactions. In fact, a cross-over in the scaling of the diffusivity in the hydrogel with increasing hydrogel density from $\nu = 1/2$ to $\nu = 1$ is in agreement with previous studies on dextran penetration into hydroxypropylcellulose [59]. However, because of the large error bars, extraction of the diffusivity scaling with respect to dextran mass in the two gels is not uniquely possible. This is mostly due to the fact that the diffusivities change rather mildly with varying dextran mass. This is why there is no attempt in this Chapter to model the scaling of the extracted diffusivities, as was done elsewhere before [44, 45, 63], but rather a focus is set on the mechanism behind the extracted free-energy differences in the following.

Figure 2.5C shows the extracted values of ΔF_{gel} for the two hydrogels as a function of the dextran mass. In all measurements one finds $\Delta F_{\text{gel}} > 0$, which suggests exclusion of the dextran molecules from the hydrogel. Also the value of ΔF_{gel} increases with the dextran mass. Since dextran as well as the PEG-hPG based hydrogels are uncharged [64], this exclusion must be due to steric repulsion, possibly enhanced by *hydration repulsion* [65, 66].

2.2.3 Elastic Free-Volume Model

For the larger dextran molecules, the hydrogel with the smaller PEG linkers, *hPG-G6*, displays a slightly stronger exclusion. The power law relation between the hydrogel free-energy and dextran mass according to $\Delta F_{\text{gel}} \propto M_{\text{dex}}{}^{\alpha}$ with an exponent of $\alpha = 1/2$ describes the data well for larger dextran masses $M_{\text{dex}} \gtrsim 20$ kDa, as shown by the dotted black line in fig. 2.5C. This power law behavior is in fact compatible with a simple elastic
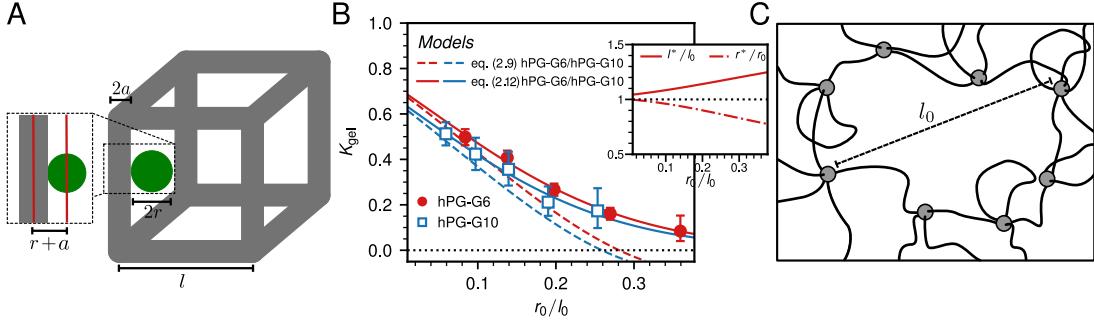
Figure 2.6: Elastic free-volume model for the partitioning of a particle in a hydrogel. A: Schematic sketch of the cubic unit-cell model for the hydrogel, made up of connected linkers of length l and a finite radius of a. The diffusing particle is modeled as a sphere of radius r. Both the particle and the linkers are elastic and can stretch or contract. B: Partition coefficient K_{gel} extracted from the experimentally measured dextran concentration profiles (symbols) in comparison to the elastic free-volume model predictions according to eq. (2.12) (solid lines). The results of the non-elastic model according to eq. (2.9) are shown as dashed lines. The inset shows the equilibrium values of l^* and r^* obtained for the *hPG-G6* gel. C: Illustration of a disordered pore in the hydrogel which has a mesh size l_0 and consists of more than four linkers (see also fig. 2.2).

free-volume model for the penetration of dextran molecules into a hydrogel, which yields the solid lines and will be derived in the following.

The model geometry is sketched in fig. 2.6A and consists of a single dextran molecule of radius r (green sphere) inside a cubic unit cell of the PEG based hydrogel (grey cylinders), similar to previous coarse-grained hydrogel models [44–46]. The presence of the hPG hubs connecting the PEG linkers is neglected in the following. The dextran experiences a reduction of its free-volume compared to the bulk solution, due to steric interactions with the PEG linkers. In the simple model geometry, the PEG linkers are located at the edges of the cubic unit cell and are modeled as impenetrable cylinders of radius a and length l. Conformational fluctuations of the PEG linkers are not treated explicitly in this model, instead the linker length l and radius a are to be understood as average values over different confirmations of the linker chains. The excluded volume V_{ex} for dextran in the cubic unit cell consists of a quarter of each of the twelve cylinders at the edges. The accessible or free-volume in the hydrogel V_{free} depends on the sum of sphere radius r and cylinder radius a and is given by

$$
\begin{aligned}
V_{\text{free}} &= V_{\text{unit}} - V_{\text{ex}} \\
&= l^3 - \frac{12}{4}\pi(r+a)^2 l + 2V_{\text{cyl}}.
\end{aligned}
\tag{2.8}
$$

Here, $V_{\mathrm{unit}} = l^3$ is the volume of the unit cell and $V_{\mathrm{cyl}} = \frac{16}{3}(r+a)^3$ is the volume of two intersecting cylinders [67], which is subtracted from the excluded volume to avoid over-counting of the unit-cell corners. The entropic contribution to the total free-energy is then given by

$$\Delta F_{\mathrm{vol}} = -k_{\mathrm{B}}T \, \ln\left(\frac{V_{\mathrm{free}}}{V_{\mathrm{unit}}}\right)$$
$$= -k_{\mathrm{B}}T \, \ln\left(1 - 3\pi\left[\frac{r+a}{l}\right]^2 + \frac{32}{3}\left[\frac{r+a}{l}\right]^3\right). \qquad (2.9)$$

Since dextran and the PEG linkers are elastic polymers, they are both flexible and can deform. For small deformations, the polymers behave like Gaussian chains [60, 61]. The elastic deformation free-energy for a cubic unit cell consisting of 12 equally deformed PEG linkers can be written as (for a detailed derivation see Section 2.4.5 in the Appendix)

$$\Delta F_{\mathrm{PEG}} = \frac{12}{2}k_{\mathrm{B}}T\left(\left[\frac{l}{l_0}\right]^2 + \frac{1 - 4\left[\frac{l}{l_0}\right]^2}{2 + \left[\frac{l}{l_0}\right]^2}\right). \qquad (2.10)$$

Here l/l_0 is the relative stretching of the PEG linkers, where l_0 denotes the edge length of the unit cell in the absence of dextran molecules. The elastic deformation energy of dextran is obtained in the same fashion and reads

$$\Delta F_{\mathrm{dex}} = \frac{3}{2}k_{\mathrm{B}}T\left(\left[\frac{r}{r_0}\right]^2 + \left[\frac{r_0}{r}\right]^2 - 2\right), \qquad (2.11)$$

where r denotes the deformed dextran radius and the equilibrium dextran radius is denoted by r_0 and is taken from Table 2.1. The complete free-energy follows as

$$\Delta F_{\mathrm{gel}}(r,l) = \Delta F_{\mathrm{vol}}(r,l) + \Delta F_{\mathrm{PEG}}(l) + \Delta F_{\mathrm{dex}}(r). \qquad (2.12)$$

The equilibrium free-energy is given by the minimal value of this free-energy expression, obtained for the optimally stretched unit cell length l^* and the optimal dextran radius r^*, which are determined numerically. The values of the unit cell length l_0 and the PEG linker thickness a are adjusted by fits to the experimental data. The model results are shown in fig. 2.6B in terms of the partition coefficient as solid lines and compared to the experiments (circles and squares) as a function of the length ratio r_0/l_0. The inset shows the obtained equilibrium values for l^* and r^* for the *hPG-G6* gel. A considerable stretching of PEG-linkers and compression of dextran is observed, which shows that elasticity effects of both PEG linkers and dextran molecules are important and cannot be neglected when estimating the free-volume.

The fit to the experimental data yields $l_0^{\mathrm{hPG\text{-}G6}} = 16.7$ nm, $l_0^{\mathrm{hPG\text{-}G10}} = 23.7$ nm, $a_{\mathrm{hPG\text{-}G6}} = 3.4$ nm and $a_{\mathrm{hPG\text{-}G10}} = 5.4$ nm. The fit values of a certainly represent an

effective PEG linker radius and include the layer of tightly bound hydration water. They are indeed, close to the respective equilibrium PEG radii $R_{\text{PEG}} = b_{\text{fl}} N_{\text{PEG}}^{3/5}/\sqrt{3}$, given as $R_{\text{PEG}}^{\text{hPG-G6}} = 4.4$ nm and $R_{\text{PEG}}^{\text{hPG-G10}} = 5.99$ nm, where $b_{\text{fl}} = 0.4$ nm denotes the Flory monomer length [68] and N_{PEG} is the respective number of PEG monomers. In fact, the free-volume model yields estimates of the number of hydration waters per PEG monomer that scatter around 8, in rough agreement with literature values (see fig. 2.12 and Section 2.4.6 in the Appendix).

The fit values for the unit cell length l_0 are significantly larger than the mean mesh size estimated based on eq. (2.1), which for a perfectly ordered cubic lattice predicts $l_{0,\text{ideal}}^{\text{hPG-G6}} = 7.1$ nm and $l_{0,\text{ideal}}^{\text{hPG-G10}} = 7.5$ nm, but still considerably shorter than the PEG contour lengths $L = b_0^{\text{PEG}} N_{\text{PEG}}$, which are $L_{\text{hPG-G6}} = 48.5$ nm and $L_{\text{hPG-G10}} = 80.9$ nm, where $b_0^{\text{PEG}} = 0.356$ nm is the PEG monomer length [68]. While the large unit cell lengths obtained from the fit to the elastic free-volume model could reflect a substantial stretching of individual PEG polymers, there is no a priori reason why the linkers should be stretched to such a considerable fraction of their contour length. This surprising results is therefore rationalized in terms of a broad distribution of pore sizes that exhibit different topologies. To illustrate this, a random pore is schematically shown in fig. 2.6C. Based on the 3:1 number ratio of linkers and cross linkers in the hydrogel formulation (cf. Section 2.1.1 and fig. 2.2), a perfectly cubic lattice could form, where each hub is connected to 6 different linkers. Such an ideal cubic connectivity is of course entropically highly unfavorable and the connectivity distribution of hubs, i.e. the distribution of the number of linkers that connect to one hub, will be rather broad and the network topology will be disordered, in which case the PEG end-to-end distance R_{PEG} will be significantly smaller than the pore size l_0 (cf. also Section 2.1.2). While in a cubic lattice each cubic facet consists of four hubs and four linkers, the pores present in the actual hydrogel will show a broad distribution of the number of participating linkers. For illustration, the pore shown in fig. 2.6C consists of eight linkers. Clearly, dextran molecules will tend to be located in larger pores in order to maximize their free-volume, and therefore the fit parameters of our model will be dominated by the tail of the pore size distribution, which explains the large fit values for l_0. This finding also allows to rationalize the larger extracted free-energy in the hydrogel in the case of the *hPG-G6* gel, even though the *hPG-G10* gel mass density is higher (cf. fig. 2.5C). The tail of the pore size distribution of the *hPG-G10* gel presumably contains larger pores which can stretch even further to minimize the unfavorable dextran-PEG interactions. Clearly, the precise topology and compositional distribution of pores cannot be predicted by our analysis, our results should thus be merely interpreted as an indication of the presence of large pores and a disordered network topology.

An approximate non-elastic version of the free-volume model is obtained by neglecting the polymer deformation term and just keeping the excluded volume term, eq. (2.9), which becomes accurate in the limit of $l_0 \gg r_0$, where $r^* \approx r_0$ and $l^* \approx l_0$. These approximate results are shown as broken lines in fig. 2.6B and describe the experimental data only for small values of r_0/l_0. When additionally approximating the logarithm in

eq. (2.9), the obtained expression for the free-energy is similar to results derived for a random fiber network [69]. Our free-volume model is valid only for short-ranged steric and hydration repulsive interactions between diffusor and linkers, if long-ranged and in particular attractive interactions are present, for example electrostatic interactions for low salt concentrations, the model would need to be adjusted accordingly.

2.2.4 Derivation of Hydrogel Permeabilities

A quantity commonly used to analyze penetration through biological barriers is the so-called permeability coefficient P which is defined as [70]

$$P(z_1, z_2) = \frac{J}{c(z_1) - c(z_2)},$$ (2.13)

where $c(z_1)$ and $c(z_2)$ are the particle concentrations at the two sides z_1 and z_1 of the barrier, and J denotes the particle flux through the barrier. Based on the diffusion eq. (2.6), the inverse permeability can be written as (for a detailed derivation see Section 2.4.7 of the Appendix)

$$\frac{1}{P(z_1, z_2)} = \int_{z_1}^{z_2} \frac{e^{\beta F(z)}}{D(z)} \, dz.$$ (2.14)

For a step-like barrier one obtains

$$\frac{1}{P} = \frac{e^{\beta \Delta F_{\text{gel}}}}{D_{\text{gel}}} L.$$ (2.15)

Here ΔF_{gel} and D_{gel} are the particle free-energy relative to the solution and the diffusivity inside the hydrogel and L denotes the width of the hydrogel barrier.

Figure 2.7A shows normalized permeability coefficients $P \cdot L$, which have been made independent of the thickness of the barrier L. Permeabilities are shown as a function of the free energy barrier and the diffusion constant in the gel. The values obtained for the different dextran molecules in the two gels are indicated in the figure. The highest permeability is observed for a low energy barrier and a high diffusor mobility, as is the case for the smallest dextran molecules (lower right corner in Figure 2.7A). On the other hand, permeation is hindered by either a high energy barrier or a low mobility in the hydrogel, both of which are observed for dextran molecules with larger molecular weights. Due to counterbalancing effects of stronger exclusion in the *hPG-G6* gel and increased immobilization in the case of *hPG-G10*, both hydrogels display comparable permeability coefficients for the analyzed dextran molecules.

2.3 Conclusions

The method introduced in this Chapter allows for the simultaneous extraction of diffusivity and free-energy profiles of particles that permeate into spatially inhomogeneous
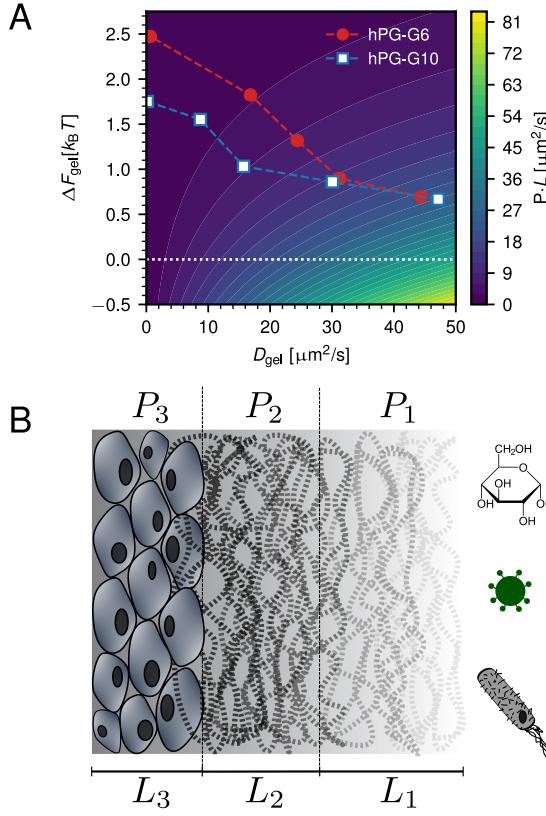
Figure 2.7: A: Normalized permeability coefficient PL through a single box-like hydrogel barrier of width L as a function of the hydrogel free-energy ΔF_{gel} and the hydrogel diffusivity D_{gel} from eq. (2.15). High permeability is observed for low free-energy barriers and high diffusivities in the hydrogel. The symbols denote the experimental data from fig. 2.5. Due to opposing trends in the free-energy barrier and the diffusivity, both hydrogels display comparable permeability coefficients. B: Schematic layered structure of a mucous membrane, as found in the stomach. Examples for different diffusors are shown, including nutrients such as glucose and pathogens such as virions or bacteria. The diffusors have to penetrate different layers of varying permeabilities to enter the tissue below the mucous membranes, the total permeability of a layered structure follows from eq. (2.16).

hydrogel systems. The method is demonstrated using concentration profile measurements of fluorescently labeled dextran molecules permeating into PEG-hPG-based hydrogels. The advantage over established ways of studying penetration processes is that both quantities can be obtained straightforward from a single experiment of an ensemble of diffusors. As these two properties physically determine the complete diffusion process, obtaining them from experiments is important for a better understanding of biological barriers.

The extracted diffusivities and free-energies are analyzed in terms of empirical scaling laws as a function of the dextran mass and a modified elastic free-volume model is developed that accounts for the particle free-energy in the hydrogel. Our modified free-volume model additionally includes the elasticity of linkers and of the diffusing molecules and thereby quantitatively reproduces the free-energies extracted from experimental data of dextran diffusing in PEG-based hydrogels. This demonstrates that elastic deformations of both the diffusor and the hydrogel network are important, in line with previous computational [71–73] and experimental studies [74]. Our model furthermore unveils significant topological disorder of the hydrogel pores and suggests that the dextran molecules preferentially partition into exceptionally large pores, which are locally even more enlarged due to PEG strand elasticity.

Diffusional barriers in biological systems often show a layered structure, as previously demonstrated for skin [17, 18, 53] (Ref. [iv]) and also known to be true for mucous membranes, which are found for instance in the gastrointestinal tract, schematically indicated in fig. 2.7B. For a layered system, eq. (2.14) shows that the individual piecewise constant permeability coefficients P_i add up inversely as

$$\frac{1}{P_{\text{tot}}} = \sum_i \frac{1}{P_i} = \sum_i \frac{e^{\beta \Delta F_i}}{D_i} L_i = \sum_i \frac{L_i}{D_i K_i}, \qquad (2.16)$$

where the sum goes over all layers, represented by their respective diffusion constants D_i, free-energy values ΔF_i or partition coefficients K_i and thicknesses L_i. Here, P_{tot} denotes the total permeability, which is dominated by the smallest permeability in the inverse sum.

Figure 2.7B schematically illustrates permeation through a layered system which represents the mammalian stomach [11]. The outermost layer of mucus is only loosely bound and characterized by the permeability P_1, it is followed by a layer of more tightly bound mucus, characterized by P_2, and adheres onto the first layer of epithelial cells, characterized by P_3. The total thickness of this diffusional barrier is about a millimeter, with the two mucus layers spanning a few hundred micrometers only [75]. Measurements in rat gastrointestinal mucosa suggest typical values of $L_1 = 109$ μm, $L_2 = 80$ μm and $L_3 \approx L_2$ [76], which are close to the range of gel thicknesses studied in this Chapter.

The total permeability is determined by the free-energies and the mobilities inside all layers. Nutrients for instance can easily penetrate through the epithelia of the gastrointestinal tract, displaying large permeabilities in the different layers. Pathogens on the other hand are in healthy environments kept from reaching the epithelium, due to low permeability in the tightly bound mucus layer ($P_2 \ll P_1$) [11]. From eq. (2.16), it is apparent that the lowest permeability in such a layered system dominates the total permeability, leading to an effective barrier function that for different particles can be caused by different parts of the layered barrier structure.

Using the method described in this Chapter, permeabilities of molecules diffusing through different environments could be estimated, representing distinct layers of biological barriers as discussed above. The technical advances described in this Chapter

will thus hopefully help to shed light on the underlying mechanisms of the function of general biological barriers including mucous membranes.

2.4 Appendix to Chapter 2

2.4.1 Measured Fluorescence Intensity Data

The experimental fluorescence intensity data, measured by our collaborators from the Haag group, displays a continuous drift in the signal in all recorded measurements, which is likely due to an automatic re-adjustment of the laser intensity in the used setup. An example of the observed drift in the raw un-scaled signal is shown in fig. 2.8A, recorded for $M_{\text{dex}} = 70$ kDa dextran molecules at the *hPG-G10* interface. Even though almost no penetration of the large dextran molecules into the hydrogel is observed, the fluorescence intensity in the probed part of the bulk solution changes significantly over time. In order to obtain physical values for the dextran concentration, the measured profiles are being re-scaled during the fitting procedure. The obtained re-scaling factors for every measured concentration profile $\vec{f}$ decline over time, thus overcoming the constant increase of signal intensity due to the drift (see fig. 2.9A). Additionally, smaller changes in the fluorescence intensity are apparent. Since robust results are obtained by employing this re-scaling routine, this suggests that the entire information about the diffusion process is present in the relative shape of the concentration profiles.

The obtained re-scaling factors can additionally be used, to estimate the experimental bulk concentration c_{bulk} far away from the hydrogel interface, based on the experimentally measured profiles alone, without using the numerically computed dextran distributions. The total amount of dextran in the system C_{tot} is computed from the first concentration profile as $C_{\text{tot}} = \int_{-\infty}^{\infty} c(z, t = 0) \; dz$, where $c(z, t = 0)$ was approximated by c_i^{init} according to eq. (2.4) in Section 2.1.5. An average experimental concentration in the bulk region $\bar{c}_{\text{bulk}}(t_{\text{j}})$ can then be estimated from the fitted re-scaling factors as

$$\bar{c}_{\text{bulk}}(t_{\text{j}}) = \frac{C_{\text{tot}} - \sum_{i=1}^{M} f_{\text{j}} \cdot c_i^{\text{exp}}(t_j) \cdot \Delta z_i}{z_{\text{top}}}. \tag{2.17}$$

Values for $\bar{c}_{\text{bulk}}(t_{\text{j}})$ are shown in fig. 2.9B and are virtually constant for the exemplary measurement of $M_{\text{dex}} = 70$ kDa dextrans, as is expected due to the absence of penetration into the hydrogel.

The re-scaling procedure is additionally validated by a comparison of the concentration profiles obtained for the $M_{\text{dex}} = 40$ kDa dextran molecules, diffusing into the *hPG-G10* hydrogel, which is presented in fig. 2.8B. The concentration profiles were measured by our collaborators in two different experiments, with a period of one month in between. The observed agreement between the data sets, with significant deviations being only present in the transition region between the hydrogel and the bulk solution, corroborates the re-scaling method used to obtain concentration profiles from the fluorescence intensity data, as well as the experimental setup.
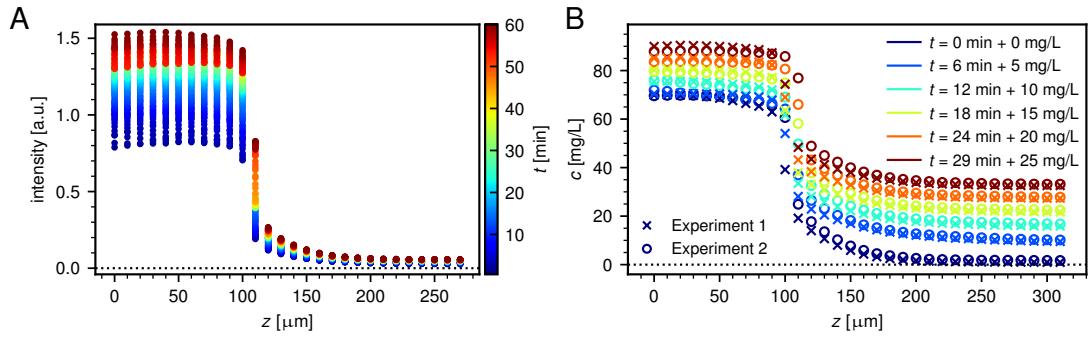
Figure 2.8: A: Raw fluorescence intensity data from experiments of $M_{dex} = 70$ kDa dextrans in combination with the *hPG-G10* hydrogel. A significant change in the signal over time is observed in the probed part of the bulk solution, even though almost no penetration of the dextrans into the hydrogel is apparent. This drift in the experimentally measured signal is overcome by the numerically determined re-scaling factors. B: Re-scaled concentration profiles measured by the Haag group one month apart in two different experiments for the $M_{dex} = 40$ kDa dextran molecules, penetrating into the *hPG-G10* gel. Good reproducibility is observed in the data. Note that profiles at different timepoints are shifted for an easier comparison.
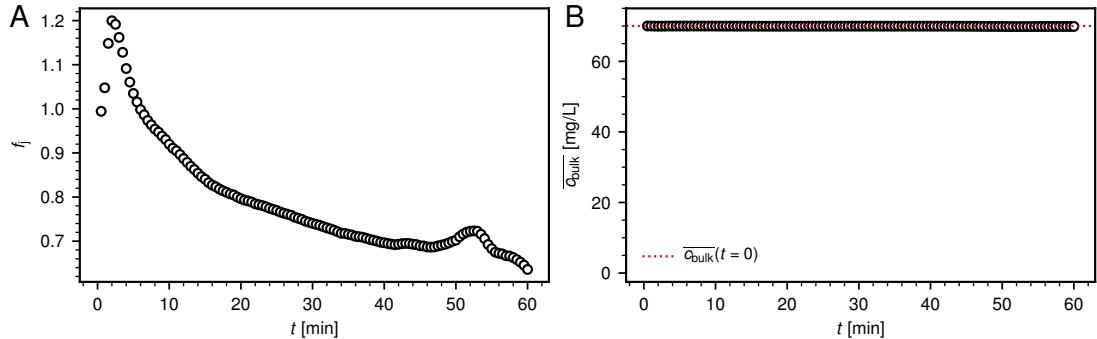
Figure 2.9: A: Set of re-scaling factors $\vec{f}$ for every measured concentration profile obtained from numerical analysis of experimental data from $M_{dex} = 70$ kDa dextrans in contact with the *hPG-G10* hydrogel. Decreasing re-scaling factors counteract the drift observed in the raw experimental data. Additionally, peaks in the re-scaling factor distribution are observed, counteracting shorter fluctuations in the fluorescence intensity. B: Average bulk concentration $\overline{c_{bulk}}$ computed according to eq. (2.17) for the same measurements. The bulk concentration remains constant in this measurement, since almost no dextran penetrates into the hydrogel.

2.4.2 Analytical Solution for Two-Segment System

Simplifying the hydrogel-water setup as a two-box system with piece-wise constant values of the free-energy and diffusion constant in the two regions allows for an analytical solution of the diffusion problem. The modeled system with the corresponding boundary conditions is sketched in fig. 2.10A.
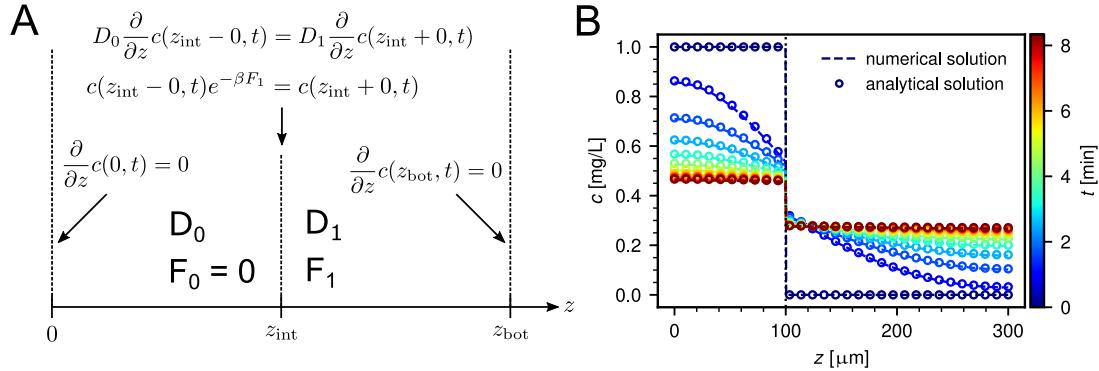
Figure 2.10: Two-segment system for the generalized diffusion equation, which can be solved analytically. A: Two-segment system with different diffusion constants and a jump in the free-energy at the interface z_{int}. The used boundary conditions are also indicated. B: Comparison of the numerical model and the analytical solution of the system explained in A, with values for the parameters of $z_{int} = 100~\mu m$, $z_{bot} = 300~\mu m$, $c_0 = 1$, $D_0 = 50~\mu m^2/s$, $D_1 = 100~\mu m^2/s$ and $F_1 = 0.5~k_B T$.

We solve the following diffusion equation in each of the two segments

$$\frac{\partial}{\partial t}c(z,t) = D(z)\frac{\partial^2}{\partial z^2}c(z,t), \tag{2.18}$$

where the diffusion constant $D(z)$ has a different value in each of the two regions

$$D(z) = \begin{cases} D_0, & \text{if } 0 \leq z \leq z_{int} \\ D_1, & \text{if } z_{int} < z \leq z_{bot} \end{cases} \tag{2.19}$$

as does the free-energy $F(z)$, which we set to zero in the left segment as reference

$$F(z) = \begin{cases} F_0 = 0, & \text{if } 0 \leq z \leq z_{int} \\ F_1, & \text{if } z_{int} < z \leq z_{bot}. \end{cases} \tag{2.20}$$

At the interface z_{int}, the flux needs to be continuous due to mass conservation, while the jump in the free-energy leads to a jump in the concentration profile $c(z = z_{int}, t)$. This defines the boundary conditions at z_{int} as

31

$$\lim_{z \nearrow z_{\text{int}}} D_0 \frac{\partial}{\partial z} c(z,t) = \lim_{z \searrow z_{\text{int}}} D_1 \frac{\partial}{\partial z} c(z,t) \qquad (2.21\text{a})$$

$$\lim_{z \nearrow z_{\text{int}}} c(z,t) e^{-\beta F_1} = \lim_{z \searrow z_{\text{int}}} c(z,t), \qquad (2.21\text{b})$$

Since we model a closed system, the edges at $z = 0$ and $z = z_{\text{bot}}$ are reflecting boundaries with

$$\frac{\partial}{\partial z} c(z = 0, t) = 0 \qquad (2.22\text{a})$$

$$\frac{\partial}{\partial z} c(z = z_{\text{bot}}, t) = 0. \qquad (2.22\text{b})$$

Initially, the diffusors are only present in the left segment, modeling the bulk solution. This defines our initial condition as

$$c(z, t = 0) = \begin{cases} c_0, & \text{if } 0 \leq z \leq z_{\text{int}} \\ 0, & \text{if } z_{\text{int}} < z \leq z_{\text{bot}}. \end{cases} \qquad (2.23)$$

We now solve eq. (2.18) by means of Laplace transformation. To this end, we use the single sided Laplace transform in time, defined as $\hat{f}(s) := \int_0^\infty f(t) e^{-st} dt$, where s is the complex variable in Laplace space $s = \sigma + i\omega$. This converts the partial differential equation (2.18) into an ordinary differential equation of second order

$$\left[s - D(z) \frac{\partial^2}{\partial z^2} \right] \hat{c}(z, s) = c(z, t = 0). \qquad (2.24)$$

The general solution of eq. (2.24) for the two regions reads

$$\hat{c}(z, s) = \begin{cases} a_1 e^{\lambda_0 z} + a_2 e^{-\lambda_0 z} + \hat{c}_{\text{p}}, & \text{if } 0 \leq z \leq z_{\text{int}} \\ a_3 e^{\lambda_1 z} + a_4 e^{-\lambda_1 z}, & \text{if } z_{\text{int}} < z \leq z_{\text{bot}} \end{cases} \qquad (2.25)$$

where we define $\lambda_i := \sqrt{\frac{s}{D_i}}, i = 0, 1$ and $\hat{c}_{\text{p}} := \frac{c_0}{s}$. The coefficients a_i of eq. (2.25) are determined by solving the system of linear equations obtained by Laplace transforming the boundary conditions of eq. (2.21) and eq. (2.22) and substituting the general solution of eq. (2.25). After some algebra, the solution to the posed problem is obtained as

$$\hat{c}(z, s) = \begin{cases} \hat{c}_{\text{p}} \frac{K \cdot \tanh(\lambda_1(z_{\text{bot}} - z_{\text{int}}))[\cosh(\lambda_0 z_{\text{int}}) - \cosh(\lambda_0 z)] + \sinh(\lambda_0 z_{\text{int}})\sqrt{\delta}}{K \cdot \tanh(\lambda_1(z_{\text{bot}} - z_{\text{int}}))\cosh(\lambda_0 z_{\text{int}}) + \sinh(\lambda_0 z_{\text{int}})\sqrt{\delta}}, & \text{if } 0 \leq z \leq z_{\text{int}} \\ \hat{c}_{\text{p}} \frac{K \cdot \cosh(\lambda_1(z_{\text{bot}} - z))\tanh(\lambda_0 z_{\text{int}})\sqrt{\delta}}{K \cdot \sinh(\lambda_1(z_{\text{bot}} - z_{\text{int}})) + \tanh(\lambda_0 z_{\text{int}})\cosh(\lambda_1(z_{\text{bot}} - z_{\text{int}}))\sqrt{\delta}}, & \text{if } z_{\text{int}} < z \leq z_{\text{bot}} \end{cases}$$

$$(2.26)$$

where $\delta := \frac{D_0}{D_1}$ and $K := e^{-\beta F_1}$.

The solution in Laplace space (eq. (2.26)) is then transformed into real space by use of the Mellin integral

$$
\begin{aligned}
c(z,t) &= \frac{1}{2\pi i} \int_{s=\sigma-i\infty}^{s=\sigma+i\infty} \hat{c}(z,s)e^{st} \; ds \\
&= \frac{e^{\sigma t}}{2\pi} \int_{-\infty}^{+\infty} \hat{c}(z,\sigma+i\omega)e^{i\omega t} \; dw,
\end{aligned}
\tag{2.27}
$$

where the last integral was solved numerically through the inverse discrete Fourier transform.

Figure 2.10B shows a comparison of the analytical solution and the numerical model for an exemplary parameter set of $z_{\text{int}} = 100 \; \mu$m, $z_{\text{bot}} = 300 \; \mu$m, $c_0 = 1 \;$ mg/L, $D_0 = 50 \; \mu\text{m}^2/s$, $D_1 = 100 \; \mu\text{m}^2/s$ and $F_1 = 0.5 \; k_\text{B}T$, mimicking a slight repulsion in the right segment. Perfect agreement between the numerical model and the analytical solution is obtained.

2.4.3 Error Estimate for Numerical Analysis

In order to determine confidence intervals for the fitted parameters of D_{sol}, D_{gel} and ΔF_{gel}, the values are varied from the optimum until the agreement with the experimental data is 50% worse than for the optimal parameter values. Figure 2.11 shows an exemplary analysis of the fitted parameters influence on the error. All parameters are varied independently, meaning that the error is always computed while keeping all other parameters fixed at their optimal values. Also, the fitted values for d_{int} and z_{int} are not changed but kept at their optimum. It is apparent that increasing the fitted diffusion constants does not affect the agreement with the experimental data as strongly as a decrease (see fig. 2.11A and B). Changing the free-energy difference influences the numerical error σ more symmetrically, meaning increasing ΔF_{gel} has the same influence on the error as decreasing it.
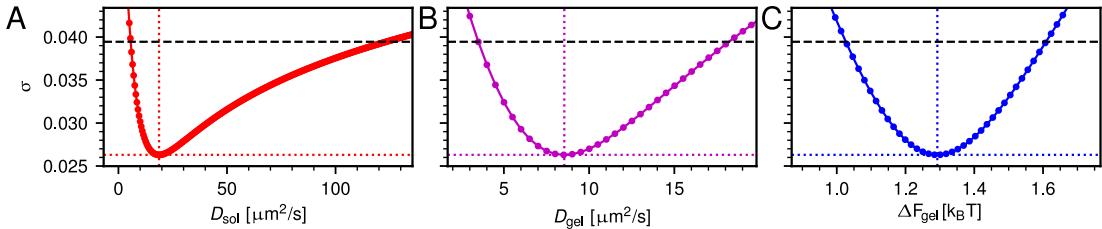
Figure 2.11: Error estimation of the fitted values for D_{sol} (A), D_{gel} (B) and ΔF_{gel} (C) for measurements of $M_{dex} = 40$ kDa dextran molecules diffusing into the *hPG-G10* hydrogel. Fitted optimal values for the parameters are indicated by dotted lines, while a 50% change in σ is shown by the dashed black line. A larger value of the diffusion constants does not affect the agreement with the experimental data as strongly as a smaller value.

2.4.4 Scaling of Diffusion Constant with Dextran Size

According to the Stokes-Einstein relation, the diffusion constant of dextran molecules in the bulk solution D_sol is expected to scale with the dextran radius r_0 as

$$D_\text{sol} \propto r_0^{-1}. \tag{2.28}$$

Assuming the dextran polymer behaves like a freely jointed chain, its radius is related to the number of monomers N_dex as [60, 61]

$$r_0 = b_0^\text{dex} \sqrt{N_\text{dex}}, \tag{2.29}$$

where b_0^dex is the dextran monomer length and N_dex can be estimated from the total molecular mass of a dextran molecule M_dex, when the monomer mass M_dex^mono is known

$$N_\text{dex} = \frac{M_\text{dex}}{M_\text{dex}^\text{mono}}. \tag{2.30}$$

This leads to the following equality

$$D_\text{sol} = \frac{k_\text{B}T}{6\pi\eta_\text{w} \frac{b_0^\text{dex}}{\sqrt{M_\text{dex}^\text{mono}}} \sqrt{M_\text{dex}}}, \tag{2.31}$$

which gives rise to a scaling of $D_\text{sol} \propto M_\text{dex}^{-1/2}$.

2.4.5 Expression for the Elastic Deformation Free Energy

The free-energy cost for stretching a polymer chain from an initial equilibrium mean square end-to-end distance $\langle \vec{R}_0^2 \rangle$ to a larger end-to-end distance $\langle \vec{R}^2 \rangle$ can be written as [60, 61]

$$\Delta F_{\text{stretch}} = \frac{3}{2} k_{\text{B}} T \frac{\langle \vec{R}^2 \rangle - \langle \vec{R}_0^2 \rangle}{\langle \vec{R}_0^2 \rangle}, \tag{2.32}$$

where $k_{\text{B}} T$ denotes the thermal energy. In the case of the PEG linkers we define the z-component of the squared end-to-end distance as $l^2 := \langle R_z^2 \rangle$, so that $l_0^2 := \langle R_{0,z}^2 \rangle$. The PEG polymer chain is only stretched in the z-direction, thus eq. (2.32) reduces to

$$\Delta F_{\text{stretch}} = \frac{3}{2} k_{\text{B}} T \frac{\langle R_x^2 \rangle + \langle R_y^2 \rangle + l^2 - \langle R_{0,x}^2 \rangle - \langle R_{0,y}^2 \rangle - l_0^2}{\langle \vec{R}_0^2 \rangle} = \frac{3}{2} k_{\text{B}} T \frac{l^2 - l_0^2}{\langle \vec{R}_0^2 \rangle}, \tag{2.33}$$

since $\langle R_x^2 \rangle = \langle R_{0,x}^2 \rangle$ and $\langle R_y^2 \rangle = \langle R_{0,y}^2 \rangle$. As the PEG polymer chain performs a random walk in all three spatial dimensions, all components of the mean squared end-to-end distance contribute equally and so

$$\frac{\langle \vec{R}_0^2 \rangle}{3} = \langle R_{0,x}^2 \rangle = \langle R_{0,y}^2 \rangle = \langle R_{0,z}^2 \rangle = l_0^2. \tag{2.34}$$

Together with eq. (2.33), eq. (2.34) leads to the stretching free-energy for a single PEG linker polymer chain

$$\Delta F_{\text{stretch}} = \frac{1}{2} k_{\text{B}} T \left[\frac{l^2}{l_0^2} - 1 \right]. \tag{2.35}$$

For the compression of a polymer chain from an initially larger mean square end-to-end distance $\langle \vec{R}_0^2 \rangle$ to a smaller one $\langle \vec{R}^2 \rangle$ we write [60, 61]

$$\Delta F_{\text{compress}} = \frac{3}{2} k_{\text{B}} T \frac{\langle \vec{R}_0^2 \rangle - \langle \vec{R}^2 \rangle}{\langle \vec{R}^2 \rangle}. \tag{2.36}$$

In the same way as above, we only allow compression along the z-axis, which leads to

$$\Delta F_{\text{compress}} = \frac{3}{2} k_{\text{B}} T \frac{\langle R_{0,x}^2 \rangle + \langle R_{0,y}^2 \rangle + l_0^2 - \langle R_x^2 \rangle - \langle R_y^2 \rangle - l^2}{\langle R_x^2 \rangle + \langle R_y^2 \rangle + l^2} = \frac{3}{2} k_{\text{B}} T \frac{l_0^2 - l^2}{\langle R_{0,x}^2 \rangle + \langle R_{0,y}^2 \rangle + l^2}. \tag{2.37}$$

Using eq. (2.34) to substitute the x- and y-components of the equilibrium end-to-end distance gives the expression for the compression free-energy of a single PEG linker

$$\Delta F_{\text{compress}} = \frac{1}{2} k_{\text{B}} T \frac{3l_0^2 - 3l^2}{2l_0^2 + l^2}. \tag{2.38}$$

The total elastic deformation free-energy per PEG linker is the sum of eq. (2.35) and eq. (2.38)

$$\Delta F_{\text{PEG}} = \frac{1}{2}k_{\text{B}}T \left(\left[\frac{l}{l_0}\right]^2 + \frac{l_0^2 - 4l^2}{2l_0^2 + l^2} \right). \tag{2.39}$$

For the twelve PEG linkers of the hydrogel unit cell this leads to eq. (2.10) of Section 2.2.3.

2.4.6 Estimating PEG-Monomer Hydration Number

Based on eq. (2.7) and eq. (2.12), we obtain the following relation between the partition coefficient K_{gel} and the volume accessible to the dextran diffusors V_{free}

$$K_{\text{gel}} = \frac{V_{\text{free}}}{V_{\text{unit}}} e^{-\beta(\Delta F_{\text{dex}} + \Delta F_{\text{PEG}})}. \tag{2.40}$$

The volume inaccessible to the dextran molecules V_{ex} (see eq. (2.8) of Section 2.2.3) is composed of a part occupied by the gel or dextran directly and a part due to tightly bound hydration water, so that

$$V_{\text{ex}} = V_{\text{unit}} - V_{\text{free}} = V_{\text{gel}} + V_{\text{hyd}} + V_{\text{dex}}, \tag{2.41}$$

where $V_{\text{gel}} = V_{\text{PEG}} + V_{\text{hPG}}$ denotes the excluded volume due to both gel components, $V_{\text{dex}} = 3\pi r^2 l - \frac{32}{3}\pi r^3$ (with r and l as explained in fig. 2.6A) denotes the excluded volume due to dextran, $V_{\text{unit}} = l^3$ is the unit cell volume and V_{hyd} is the volume occupied by hydration water. Since r denotes the hydrodynamic radius of the spherical dextran, we assume V_{hyd} to be the volume of hydration water only binding to the gel components.

The mass fraction Φ_{gel} of the gel components inside the hydrogel is defined as the ratio of the mass of the gel components m_{gel} to the total mass m_{tot}, but since the mass density of the gel components is comparable to that of water, it also represents the fraction of inaccessible volume due to the gel components

$$\Phi_{\text{gel}} := \frac{m_{\text{gel}}}{m_{\text{tot}}} \approx \frac{V_{\text{gel}}}{V_{\text{unit}}}. \tag{2.42}$$

In the same fashion we can also estimate the fraction of inaccessible volume due to only the PEG linkers as

$$\Phi_{\text{PEG}} = \frac{m_{\text{PEG}}}{m_{\text{tot}}} = \frac{n_{\text{PEG}} M_{\text{PEG}}}{m_{\text{tot}}} \approx \frac{V_{\text{PEG}}}{V_{\text{unit}}}, \tag{2.43}$$

where n_{PEG} is the total number and M_{PEG} the molar mass of the PEG linkers. Combining eq. (2.40), eq. (2.41) and eq. (2.42) from above gives the following expression for the volume fraction occupied by hydration water

$$\frac{V_{\text{hyd}}}{V_{\text{unit}}} = 1 - \Phi_{\text{gel}} - K_{\text{gel}} e^{\beta(\Delta F_{\text{dex}} + \Delta F_{\text{PEG}})} - 3\pi \left(\frac{r}{l}\right)^2 + \frac{32}{3}\left(\frac{r}{l}\right)^3. \tag{2.44}$$

The hydration water of eq. (2.44) in principle binds to the entire hydrogel, meaning the hPG hubs and the PEG linkers. For a rough estimate, we neglect the presence of the hPG hubs and assume V_{hyd} is the volume of water molecules hydrating only the PEG linkers. We can compute the fraction of hydration water per unit PEG volume from eq. (2.43) and eq. (2.44) as

$$\frac{V_{\text{hyd}}}{V_{\text{PEG}}} = \frac{n_{\text{hyd}} v_{\text{w}}}{n_{\text{PEG}} v_{\text{PEG}}} = \frac{1 - \Phi_{\text{gel}} - K_{\text{gel}} e^{\beta(\Delta F_{\text{dex}} + \Delta F_{\text{PEG}})} - 3\pi \left(\frac{r}{l}\right)^2 + \frac{32}{3}\left(\frac{r}{l}\right)^3}{\Phi_{\text{PEG}}}, \tag{2.45}$$

where n_{hyd} is the number of hydration water molecules, v_{w} is their partial volume, n_{PEG} is the number of PEG linkers and v_{PEG} is the PEG linker partial volume. The ratio between the partial volumes of water and the PEG linkers is approximated by the ratio of their molar masses as

$$\frac{v_{\text{w}}}{v_{\text{PEG}}} \approx \frac{M_{\text{w}}}{M_{\text{PEG}}}, \tag{2.46}$$

with the water molar mass $M_{\text{w}} = 18$ g/mol and the molar mass of the respective PEG linker M_{PEG} (see Section 2.1.1). From eq. (2.45), we can now compute the number of hydration waters per PEG linker molecule as

$$\frac{n_{\text{hyd}}}{n_{\text{PEG}}} = \frac{1 - \Phi_{\text{gel}} - K_{\text{gel}} e^{\beta(\Delta F_{\text{dex}} + \Delta F_{\text{PEG}})} - 3\pi \left(\frac{r}{l}\right)^2 + \frac{32}{3} \left(\frac{r}{l}\right)^3}{\Phi_{\text{PEG}}} \frac{M_{\text{PEG}}}{M_{\text{w}}}. \tag{2.47}$$

In order to obtain the number of hydration waters per PEG-monomer we simply divide eq. (2.47) by the respective number of PEG-monomers per linker N_{PEG}, which we obtain from the ratio of total linker mass M_{PEG} and PEG-monomer mass $M_{\text{PEG}}^{\text{mono}} = 44$ g/mol, as $N_{\text{PEG}} = M_{\text{PEG}}/M_{\text{PEG}}^{\text{mono}}$. The number of hydration waters per PEG-monomer can thus be obtained as

$$\frac{n_{\text{hyd}}}{n_{\text{PEG}}^{\text{mono}}} = \frac{1 - \Phi_{\text{gel}} - K_{\text{gel}} e^{\beta(\Delta F_{\text{dex}} + \Delta F_{\text{PEG}})} - 3\pi \left(\frac{r}{l}\right)^2 + \frac{32}{3} \left(\frac{r}{l}\right)^3}{\Phi_{\text{PEG}}} \frac{M_{\text{PEG}}^{\text{mono}}}{M_{\text{w}}}. \tag{2.48}$$

With the values of $K_{\text{gel}} e^{\beta(\Delta F_{\text{dex}} + \Delta F_{\text{PEG}})}$, $V_{\text{dex}}/V_{\text{unit}} = 3\pi \left(\frac{r}{l}\right)^2 - \frac{32}{3} \left(\frac{r}{l}\right)^3$, Φ_{gel} and Φ_{PEG} for the two hydrogels, eq. (2.48) allows us to estimate the number of hydration waters per PEG monomer for all measurements. Figure 2.12 shows the results of the calculation for each of the two hydrogels. Estimated values scatter around 8 water molecules per PEG monomer, with a slight dependence on the PEG linker length and dextran mass. Depending on the employed experimental method, values reported in the literature vary, ranging from 2 to 11 water molecules per PEG monomer [77–81]. Additionally, an increase of the hydration waters per monomer has been observed, as a function of the polymerization degree [82]. The values obtained from our estimates, all lie within the range of values reported in the literature, as indicated by the grey shaded area in fig. 2.12. This further corroborates our methodology and specifically the model for the free-energy of eq. (2.12), since the estimate of eq. (2.48) is based on this model.
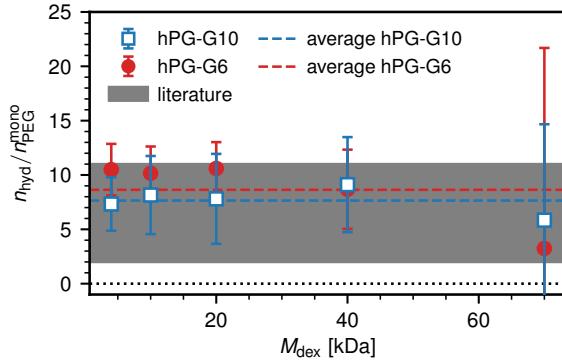
Figure 2.12: Estimated number of water molecules per PEG monomer $n_{\mathrm{hyd}}/n_{\mathrm{PEG}}^{\mathrm{mono}}$ from the obtained values of K_{gel} for the two hydrogels based on eq. (2.48). The estimated values scatter around $n_{\mathrm{hyd}}/n_{\mathrm{PEG}}^{\mathrm{mono}} = 8$ and agree with the range of values reported in the literature indicated as the grey shaded area, ranging from $n_{\mathrm{hyd}}/n_{\mathrm{PEG}}^{\mathrm{mono}} = 2$ to $n_{\mathrm{hyd}}/n_{\mathrm{PEG}}^{\mathrm{mono}} = 11$ [77–81]. Error bars are computed from Gauß error propagation of eq. (2.48).

2.4.7 Permeability Coefficient

The definition of the permeability coefficient P is, as stated in Section 2.2.4 [70]

$$P(z_1, z_2) := \frac{J}{c(z_1) - c(z_2)}, \tag{2.49}$$

with the stationary flux J and the equilibrium concentrations on both sides of the barrier $c(z_1)$ and $c(z_2)$. From the generalized diffusion equation (2.6), one obtains the stationary flux for the case of $\partial c(z,t)/\partial t = 0$ as

$$J = D(z)e^{-\beta F(z)} \frac{\partial}{\partial z} \left(c(z,t)e^{\beta F(z)} \right), \tag{2.50}$$

as a function of the diffusion constant $D(z)$ and the free-energy landscape $F(z)$ across the barrier. After rearranging eq. (2.50) and integrating from one side of the barrier from z_1 to the other z_2, we obtain the following relation

$$J \int_{z_1}^{z_2} \frac{e^{\beta F(z)}}{D(z)} \, dz = c(z_1, t)e^{\beta F(z_1)} - c(z_2, t)e^{\beta F(z_2)}. \tag{2.51}$$

We now assume that the free-energy value is the same on both sides of the barrier and additionally set it to zero as reference so that $F(z_1) = F(z_2) = 0$ and thus

$$J \int_{z_1}^{z_2} \frac{e^{\beta F(z)}}{D(z)} \, dz = c(z_1, t) - c(z_2, t), \tag{2.52}$$

which, in combination with eq. (2.49), results in eq. (2.14) used in Section 2.2.4

$$\frac{1}{P} = \int_{z_1}^{z_2} \frac{e^{\beta F(z)}}{D(z)} \, dz. \tag{2.53}$$

Chapter 3

Hydration Levels of Lipid Membranes in Presence of Polar Co-Solutes and Salt

Bibliographic information:
Parts of this Chapter have been published under Ref. [ii].

Naturally occurring lipid membranes experience a strong repulsion at separations below 2-3 nm [28, 29]. This phenomenon is called *hydration repulsion* and plays an essential role in biology as it creates a barrier against close membrane contacts, thereby suppressing uncontrolled membrane adhesion and fusion [32]. Additionally, it provides lipid membrane systems with the fluid environment required for vital functioning. Under dry conditions, however, dehydration due to osmotic stress can affect lipid self-assembly with far-reaching consequences. One example are dehydration-induced phase transitions, shifting the membrane state from fluid to gel-like, which have been studied before [83, 84] ajd have been associated with altered barrier functions of the human stratum corneum (SC), the outermost layer of the skin [34]. The SC is formed by dead corneocyte cells embedded in a lipid multilamellar matrix, only a few micrometers thick. The lipid bilayers in the SC are arranged parallel to the skin surface [35]. It constitutes a penetration barrier and thus exhibits very low permeability for hydrophilic and hydrophobic molecules [17].

In nature, protection against osmotic stress is commonly achieved by the release of small polar co-solutes with low vapor pressure, commonly referred to as osmolytes [33, 85]. These molecules serve to retain the physiological, fluid state of membrane systems in case of low relative humidity. This strategy is taken by algae and higher plants, which produce small carbohydrates and polyols, like glycerol [86, 87]. Similarly, insects and higher animals rely on glycerol, urea, and trimethylamine-N-oxide (TMAO), among others [88, 89]. The human skin contains a mixture of small polar compounds that is referred to as the *natural moisturizing factor* (NMF), comprising free amino acids, derivatives thereof, lactic acid, urea, and glycerol [90, 91]. The manifestation of NMF components in the SC is well documented, and their presence is considered crucial to maintain softness and pliability [91, 92]. In fact, defective skin conditions and certain skin diseases, for example, winter xerosis and atopic dermatitis, are associated with decreased NMF levels in the SC [93, 94].

Previous studies on urea, glycerol, and small carbohydrates have shown that these

molecules act as non-volatile substitutes of water molecules, thereby protecting self-assembled structures that are otherwise only present in more hydrated conditions [95–97]. More recently, in a study related to this thesis [25] (Ref. [v]), it was shown that TMAO, in contrast to urea, exhibits unfavorable interactions with lipid headgroups and is therefore preferentially expelled from membrane multilayers via precipitation at very dry conditions [25] or by partitioning into the excess aqueous medium when present [98]. In a wide range of dehydrating osmotic pressures, however, both urea and TMAO remain confined between the membrane surfaces [25].

In this Chapter, the influence of co-solutes on the *hydration repulsion* between lipid membranes, the interfacial force that ultimately governs the hydration level of membrane systems subject to osmotic stress, is investigated [28]. Pressure-hydration curves were obtained by our experimental collaborators from the Sparr group (Lund University) via sorption calorimetry and sorption balance experiments of phospholipid multilayers containing defined amounts of urea, TMAO, and of the salt NaCl and reveal that the repulsion can be dramatically enhanced, depending on the chemistry of the co-solute (for chemical structures see fig. 3.1A). The effect of TMAO is 2-3 times stronger than that of urea or NaCl. The experimental pressure-hydration curves are quantitatively reproduced in solvent-explicit atomistic molecular dynamics (MD) simulations, which precisely yield the chemical potential of water [99, 100] (for a simulation snapshot see fig. 3.1B). Detailed analysis of the simulation results provides the physical explanation for the observed repulsion enhancement: Additional repulsion arises from the osmotic pressure generated by the co-solutes, an effect which is amplified for TMAO, due to its unfavorable interactions with the membrane surfaces and its extraordinarily high osmotic coefficient. For high enough TMAO weight fractions, the thermodynamics of membrane dehydration is dominated by the dehydration of the confined TMAO solution.

While the fluidizing effect of small polar co-solutes has so far been mainly attributed to their ability to substitute for water molecules [96, 97], the enhancement of the *hydration repulsion* identified and explained in this Chapter demonstrates that co-solutes can additionally have a moisturizing effect in the literal sense: At dry conditions, i.e, depressed water chemical potential, they retain additional water molecules and therefore provide membranes with a fluid and more physiological environment.

3.1 Methodology

3.1.1 Sample Preparation

For the experiments performed by our collaborators at Lund University, the phospholipids dimyristoylphosphatidylcholine (DMPC) and palmitoyl-oleoyl-phosphatidylcholine (POPC) were purchased from Avanti Polar Lipids, Inc. (Alabaster, AL). Urea and TMAO were obtained from Sigma-Aldrich and NaCl from VWR. The samples were prepared so that the co-solute-lipid mass fraction (of urea, TMAO or NaCl) in the dry samples, $\Psi_{\mathrm{cosol}}^{\mathrm{lip}} = m_{\mathrm{cosol}}/(m_{\mathrm{cosol}} + m_{\mathrm{lip}})$, was fixed while the water content in terms of
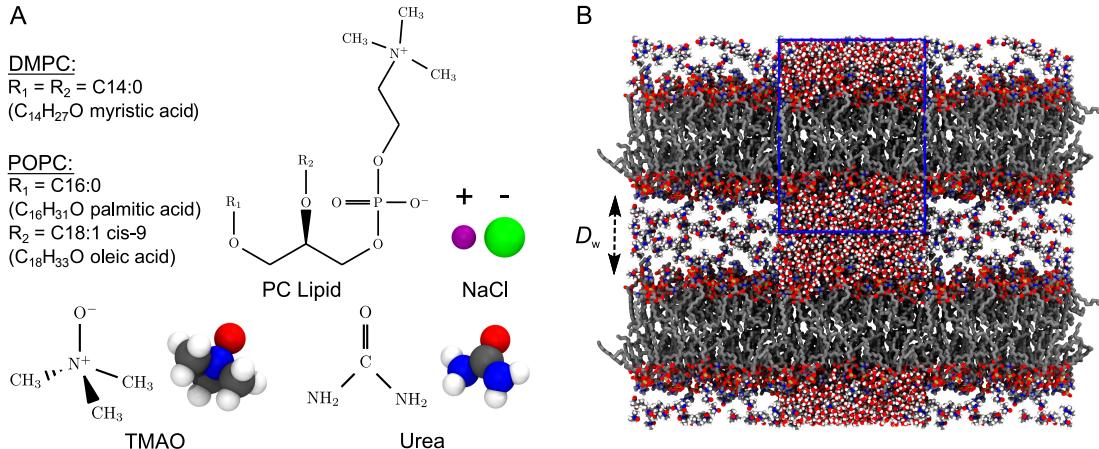
Figure 3.1: A: Chemical structures of the studied lipids and co-solutes. B: Snapshot from simulations of DMPC bilayers loaded with 10 wt% TMAO at a hydration level of $n_w = 25$ water molecules per lipid, corresponding to a water layer thickness of $D_w \approx 2.5$ nm. The simulation box is indicated with a blue rectangle. Water is only shown in the central periodic images.

the number of water molecules per lipid $n_w = N_w/N_{lip}$ is variable.

3.1.2 Sorption Measurements

Our collaborators from the Sparr group (Lund University) performed sorption experiments, in which the relative hydration and thus the water chemical potential is monitored while simultaneously adjusting the water content of the studied sample. Two kinds of sorption experiments were performed, sorption calorimetry and sorption microbalance measurements.

For the sorption calorimetry experiments our collaborators used a double twin isothermal microcalorimeter studying the thermodynamics of water vapor sorption [101]. The instrument involves a two-chamber calorimetric cell, with a sorption chamber that contains the dry sample and a vaporization chamber in which liquid water is injected to start the sorption experiment. The chambers are connected by a tube. Water vaporizes in the vaporization chamber and diffuses through the tube to the sorption chamber where it is absorbed by the sample. The calorimetric cell is inserted into a double twin isothermal microcalorimeter that separately measures thermal powers released or absorbed in the two chambers. The data for each experiment were recorded for ca. 14 days at $T = 27°C$. The experimental setup can be considered a continuous titration of an initially dry sample with water vapor [101]. Using this method, one can simultaneously monitor the water uptake in terms of n_w, the partial enthalpy of water, and the relative humidity h_{rel}, which is then converted into the water chemical potential as $\Delta\mu = -RT \ln(h_{rel}/100)$, where R is the gas constant.

In addition, osmotic coefficients Φ of TMAO, urea and sodium chloride can be determined from the water chemical potential in aqueous solutions without lipids at various co-solute concentrations, using the following equation [102]

$$\Phi(x_{\mathrm{w}}) = \frac{\Delta\mu}{\Delta\mu_{\mathrm{is}}} = \frac{\Delta\mu}{RT\,\ln(x_{\mathrm{w}})}, \tag{3.1}$$

where $\Delta\mu_{\mathrm{is}}$ is the water chemical potential in an ideal solution which solely depends on the water mole fraction x_{w} and $\Delta\mu$ denotes the real water chemical potential. The mole fraction of water can also be expressed in terms of the molal solute concentration b as $x_{\mathrm{w}}(b) = 1/(1 + \nu M_{\mathrm{w}}b)$, where M_{w} is the molar mass of water and ν is the ideal van't Hoff factor ($\nu_{\mathrm{NaCl}} = 2$, $\nu_{\mathrm{TMAO}} = \nu_{\mathrm{urea}} = 1$).

Sorption microbalance measurements were performed by our experimental collaborators from the Sparr group using an Aquadyne DVS microbalance device from Quantachrome Instruments. The dry samples were placed on pans in the device and exposed to a stream of nitrogen at controlled relative humidity h_{rel}. The balance measures the mass gain or loss over time with a weight reading every 5 s. Experiments started with drying steps, where h_{rel} was brought as closely as possible to zero for 240 – 5000 minutes at 40°C and then for 180 – 5000 minutes at 27°C. After drying, the experiments continued subsequently with a ramp of h_{rel} steps at $T = 27°$, where each step was performed for 180 – 5000 mins. The total weight of water and dry sample at each h_{rel} step was obtained from the final plateau values of the weight recorded after each change in h_{rel} and immediately before the next h_{rel} step. Sorption isotherms were constructed based on the water content as a function of h_{rel}.

3.1.3 Molecular Dynamics Simulations

Using the GROMACS 2016.4 package [103], planar lipid bilayers with $N_{\mathrm{lip}} = 72$ lipid molecules (36 in each leaflet) were simulated at various hydration levels and with various co-solute contents. For a simulation snapshot see fig. 3.1B. Periodic boundary conditions were imposed in all directions, effectively representing infinite stacks of hydrated lipid bilayers. Unless stated otherwise, the Berger lipid forcefield [104] was employed in combination with SPC/E water [105] and thermodynamically optimized forcefields for TMAO [106], urea [107] and NaCl [108]. In order to investigate forcefield effects, selected simulations were repeated with the CHARMM36 forcefield for lipids and ions [109, 110] in combination with the TIP3P water model [111, 112] (see Section 3.2.7). Simulations were run in the NpT-ensemble at $T = 300$ K and atmospheric pressure of $p = 1$ bar. Temperature was controlled using the velocity re-scaling thermostat [113] with a time constant of $\tau_T = 0.5$ ps, while for the pressure the Berendsen barostat [114] was used with semi-isotropic pressure coupling with a time constant of $\tau_p = 1$ ps and a compressibility of $\kappa = 4.5 \cdot 10^{-5}$ bar^{-1}. The timestep was $\Delta t = 2$ fs. Charge interactions were modeled using the particle-mesh-Ewald (PME) method [115] and van der Waals interactions were described by Lennard-Jones potentials shifted to zero at the cut-off. For both, electrostatics and van der Waals interactions, a cut-off

radius of $r_c = 0.9$ nm was used. Starting configurations for the different hydration levels were generated by step-wise dehydration of a highly hydrated bilayer ($n_w = 25$) and subsequent equilibration for 10 ns. All data points represent averages over five independently dehydrated systems. For density profiles and observables derived thereof data were gathered from 10 ns production runs of each of the five systems, amounting to a total of 50 ns.

The repulsive pressure Π was obtained from the shift $\Delta\mu$ in the water chemical potential according to eq. (3.2). To determine $\mu = \mu^{ex} + \mu^{id}$, its excess and ideal contributions, μ^{ex} and $\mu^{id} = k_B T \ln(\rho_w \Lambda^3 N_A / M_w)$, were measured independently, where ρ_w is the water density, $\Lambda \approx 0.0237$ nm is the thermal wavelength of water at $T = 300$ K and N_A is Avogadro's number. While μ by definition is constant over the simulation volume in thermal equilibrium, μ^{ex} and μ^{id} are not. Due to the inhomogeneous water distribution perpendicular to the membrane surface, $\mu^{ex}(z)$ and $\mu^{id}(z)$ via $\rho(z)_w$ are functions of the perpendicular coordinate, z. As a consequence, μ^{ex} and μ^{id} have to be evaluated at the same z position in the simulation box to determine μ. While μ^{id} trivially follows from ρ_w, μ^{ex} was determined via a computationally efficient combination of two approaches, the test particle insertion [116] for the Lennard-Jones contribution and the thermodynamic integration with multi-state Bennet acceptance ratio analysis [117] for the Coulomb contribution. The thermodynamic integration involved 18 λ-steps of at least 10 ns duration each, amounting to a total simulation time of at least 5 x 18 x 10 ns = 900 ns per data point, or 7.2 μs per pressure-distance curve. The water chemical potential of the bulk reference μ_0 was approximated by averaging values obtained at the three largest hydration levels ($n_w = 19$, 22, and 25).

Interaction free energies were computed by integrating the change in the water chemical potential as $\Delta G(n_w) = \int_{n_w}^{\infty} \Delta\mu(n'_w) \, dn'_w$. The enthalpic contribution was computed from the system's total enthalpy as $\Delta H(n_w) = H(n_w) - (H(n_w^{max}) - (n_w^{max} - n_w) \cdot dH_w / dN_w)$, where $n_w^{max} = 25$. From independent simulations of bulk water $dH_w / dN_w = -38.67$ kJ/mol is determined (see fig. 3.8 in the Appendix to this Chapter).

Osmotic coefficients were determined by measuring the change in water chemical potential $\Delta\mu$ in simulations of bulk co-solute solutions at various concentrations. The corresponding values for the osmotic coefficients Φ were then calculated using eq. (3.1).

3.2 Results and Discussion

TMAO and urea are commonly-studied co-solutes, due to their ability to stabilize and destabilize, respectively, the native fold of proteins [118]. In phospholipid bilayer systems, a study related to this thesis [25] (Ref. [v]) showed that TMAO is repelled from the lipid headgroup region, while urea has a slight affinity for the bilayer surface. Here, the effect of TMAO and urea as well as NaCl on the hydration of phospholipid multilayers is investigated. Two lipid species, one with saturated chains and one with partially unsaturated chains, dimyristoyl-phosphatidylcholine (DMPC) and palmitoyl-oleoyl-phosphatidylcholine (POPC), respectively, are studied. First, the experimental
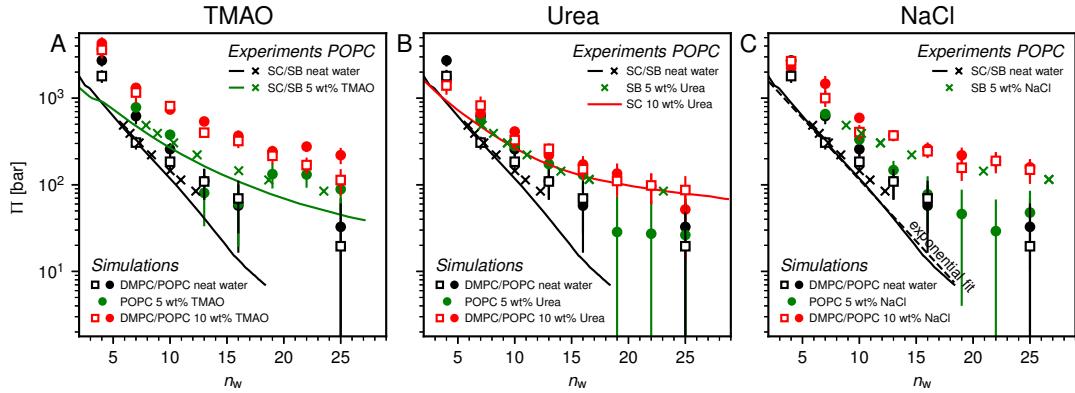
Figure 3.2: Pressure-hydration curves $\Pi(n_\mathrm{w})$ of POPC membranes with and without added TMAO (A), urea (B), and NaCl (C), as obtained in sorption balance (SB - crosses) and sorption calorimetry (SC - solid lines) experiments from the Sparr group and simulations. The figure also contains simulation data for DMPC. The dashed line in panel C indicates an exponential fit to the sorption calorimetry data in the absence of co-solutes, with decay length $\lambda_\mathrm{POPC} = 0.29$ nm (see Section 3.2.1).

data obtained by the Sparr group via sorption calorimetry and sorption balance are presented. This is followed by a description of the simulation results and their comparison with the experimental data. Finally, the underlying mechanisms identified through simulation analysis are discussed.

3.2.1 Influence of Co-Solutes on the Hydration Repulsion

Figure 3.2 shows the relationships between the dehydrating osmotic pressure Π and the hydration level n_w as obtained in sorption experiments performed by our collaborators from the Sparr group (Lund University), for samples composed of POPC lipids with varying amounts of co-solutes (data for DMPC lipids are shown in fig. 3.10 in the Appendix to this Chapter). The dehydrating osmotic pressure follows from the shift in the water chemical potential, $\Delta\mu$ (see Section 3.1), as

$$\Pi = -\frac{\Delta\mu}{v_\mathrm{w}}, \tag{3.2}$$

where v_w is the partial molecular volume of water [101]. In the absence of co-solutes, the curves exhibit an approximately exponential pressure decay with increasing hydration, i.e., with increasing surface separation (see dashed line in fig. 3.2C). The latter is defined in terms of an equivalent water layer thickness,

$$D_\mathrm{w} = 2n_\mathrm{w}v_\mathrm{w}^0/A_\mathrm{lip}, \tag{3.3}$$

where v_w^0 is the volume per water molecule in bulk and A_lip the average area per lipid (see further below). The observed exponential decay in the repulsive pressure reflects the well-known *hydration repulsion* between PC-lipid membranes [28, 30]. The fitted decay lengths in the absence of co-solute are $\lambda_\mathrm{DMPC}^{n_\mathrm{w}} \approx 2.3$ and $\lambda_\mathrm{POPC}^{n_\mathrm{w}} \approx 3.1$ in units of n_w. For areas per lipid of $A_\mathrm{lip} \approx 0.60 - 0.65$ nm^2 (see fig. 3.4), this corresponds to decay lengths of $\lambda_\mathrm{DMPC} \approx 0.21$ nm and $\lambda_\mathrm{POPC} \approx 0.29$ nm, in agreement with the literature [30, 119]. The addition of co-solutes significantly increases both strength and range of the repulsion. The increase in the hydration level n_w for a fixed osmotic pressure upon co-solute addition clearly demonstrates that the presence of co-solutes leads to the retention of additional water molecules for a given humidity level. The strength of this effect is monotonic in the added co-solute mass fraction, as seen for TMAO in panel A, but it is not simply proportional to the co-solute concentration. Instead, the repulsion is amplified more strongly for TMAO, although the added mass fraction corresponds to a lower co-solute concentration compared to the other co-solutes with a smaller molar mass. The results in fig. 3.2 demonstrate that co-solutes have a pronounced influence on the *hydration repulsion* between lipid membranes, which is however strongly dependent on the co-solute chemistry. The underlying physical mechanisms are discussed in the following on the basis of the results obtained with MD simulations.

3.2.2 Comparing Experiments and Simulations

Over the last few years, computational studies have demonstrated that dehydrating osmotic pressures in atomistic MD simulations can be determined via precise measurements of the water chemical potential μ as a function of the hydration level [99, 100]. In analogy to the experimental procedure, the osmotic pressure follows from $\Delta\mu = \mu - \mu_0$ according to eq. (3.2). In the simulations the reference chemical potential in neat bulk water is $\mu_0 = -48.3$ kJ/mol and the partial molecular volume of water, v_w, is found to be approximately equal to $v_\mathrm{w}^0 \approx 0.0304$ nm^3 for all hydration levels (see Section 3.4.1 in the Appendix). The main simulation results are reported for the Berger lipid forcefield, which is known to quantitatively reproduce pressure-distance curves between lipid bilayers [100], and which uses the SPC/E water model, for which also the co-solute forcefields have been optimized [106–108].

As seen in fig. 3.2, the pressure vs. hydration data obtained in the simulations are in near-quantitative agreement with the corresponding experimental data on POPC. While the agreement between simulations and experiments for lipid membranes in pure water has been demonstrated earlier [30, 100], this Chapter shows that the simulations also accurately reproduce the effect of added TMAO and urea. This agreement lends credibility to the employed forcefields and simulation methodology and motivates further analysis of the simulation trajectories as discussed below. In the case of NaCl the simulations significantly underestimate the added repulsion, which must likely be attributed to shortcomings in the forcefield regarding the interaction of Na$^+$ with the membrane surfaces (see Section 3.2.7). The simulation data for DMPC are also shown in

fig. 3.2. They are very similar to the ones obtained with POPC and, as shown in fig. 3.10 in the Appendix, agree with the experiments, but only within the limits of their comparability. Namely, DMPC at low hydration levels undergoes a phase transition from fluid to gel-like, which is not captured on the time scale of the MD simulations [84]. Moreover, phase separation of co-solutes from the lipid phase, which was reported experimentally earlier for low hydration levels [25], by construction cannot occur in the MD simulations which involve only a single bilayer. Generally, it should be noted that simulations of POPC or DMPC multilayers loaded with as much as 10 wt% co-solutes for the same reasons do not always have an experimental counterpart, especially at very low hydration. They are nonetheless helpful to elucidate the physical mechanisms underlying the experimentally observed effects.

3.2.3 Membrane-Co-Solute Interactions

It was previously shown that the partitioning of co-solutes within multilamellar membrane systems is sensitive to the co-solutes' preferential interactions with the membrane surfaces [25, 98]. It is therefore likely that co-solute/membrane preferential interactions are of relevance also for the membranes' short-range repulsion [120]. Figure 3.3A shows normalized density distributions perpendicular to the membrane surface, ρ/ρ_{cen}, of TMAO, urea, Na^+, and Cl^- in simulations of highly hydrated POPC membranes ($n_{\mathrm{w}} = 25$) containing 10 wt% TMAO, urea, or NaCl, respectively. Here, ρ_{cen} denotes the co-solute density at the center of the water layer. The membrane surface at $z = 0$ is defined as the surface of a water layer of thickness D_{w} according to eq. (3.3).

Preferential accumulation or depletion of the respective solutes at the membrane surface is quantified in terms of the surface excess Γ, which is computed from the co-solute density profiles as

$$\Gamma = \int_{-\infty}^{0} \rho(z) \; dz + \int_{0}^{\infty} [\rho(z) - \rho_{\mathrm{cen}}] \; dz. \tag{3.4}$$

TMAO exhibits a very strong depletion at the interface, $\Gamma_{\mathrm{TMAO}}(n_{\mathrm{w}} = 25) < 0$, so that it accumulates in the center of the aqueous region. As shown below, the magnitude of this depletion is robust with respect to forcefield variations. Regarding the urea distribution, the density deficit ($\rho - \rho_{\mathrm{cen}} < 1$) on the aqueous side ($z > 0$) is somewhat more pronounced than its excess on the membrane side ($z < 0$), reflecting a weak yet significant depletion of urea at the membrane surface at this hydration level, $\Gamma_{\mathrm{urea}}(n_{\mathrm{w}} = 25) < 0$. The exact value of this depletion is however forcefield-dependent (see below). In the case of NaCl, the combined distribution of Na^+ and Cl^- exhibits an excess on the the membrane side overcompensating the slight depletion on the aqueous side, such that the overall surface excess of NaCl becomes positive. The pronounced adsorption of Na^+ (see its individual distribution in fig.3.3A) into the headgroup region, as reported earlier [121], has however been critically discussed and attributed to shortcomings of the Berger forcefield [122]. As shown below, a strong forcefield dependence is indeed observed regarding this aspect.

The hydration-dependent values of Γ, normalized by ρ_{cen}, are shown in fig. 3.3B. TMAO is strongly repelled from the membrane surface for almost all hydration levels. Urea is weakly repelled from the membrane surface at high hydration levels but attracted at low hydration. The surface excess of NaCl is significantly positive, especially at low hydration levels, where it is stressed again that this result is specific to the Berger forcefield.
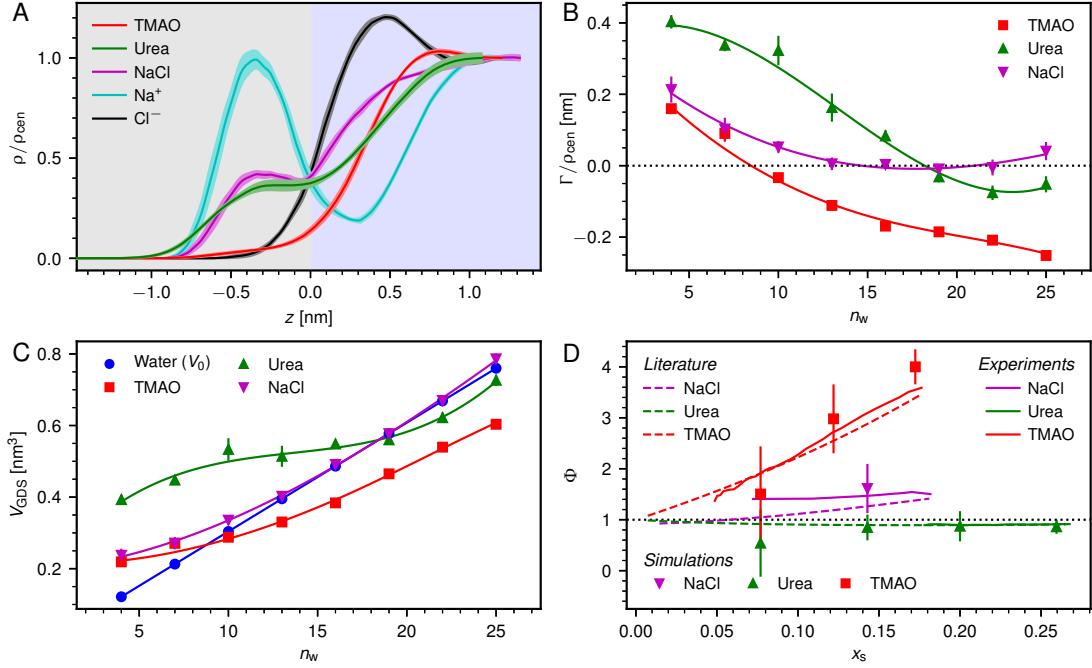
Figure 3.3: A: Normalized density profiles of the co-solutes perpendicular to the membrane surface at high hydration (POPC, $n_w = 25$). The profiles are averaged over five independent simulations with 10 wt% of co-solutes. Shaded areas indicate standart errors of the mean. The background color indicates the location of the lipid bilayer (grey) and the waterslab (blue) in the Gibbs dividing surface definition. B: Hydration-dependent surface excess for the different co-solutes as computed from eq. (3.4). C: Volume per lipid effectively accessible to the co-solutes, $V_{GDS} = A_{lip}D_{GDS}/2$, as a function of the hydration level. Lines show cubic smoothing splines. D: Concentration-dependent osmotic coefficients from the experimental literature [123–125] and the corresponding values from sorption experiments performed by our collaborators and simulations obtained in the present work. Data are plotted over the solute mole fraction $x_s = 1 - x_w$ for clarity. The dotted horizontal line indicates ideal behavior ($\Phi = 1$).

The volume per lipid effectively accessible to the co-solutes is $V_{GDS} = A_{lip}D_{GDS}/2$, where $D_{GDS} = D_w - 2z_{GDS}$. The Gibbs dividing surface for the co-solutes, z_{GDS}, is defined as the z-position for which Γ would vanish and is computed as

$$z_{\text{GDS}} = z_{\text{lip}} + \int_{z_{\text{lip}}}^{z_{\text{w}}} \left[1 - \frac{\rho(z)}{\rho_{\text{cen}}} \right] \, dz, \tag{3.5}$$

where z_{lip} and z_{w} denote the centers of the bilayer and of the water slab, respectively. Figure 3.3C shows V_{GDS} as a function of n_{w} for all three co-solutes. It is seen that $V_{\text{GDS}}^{\text{TMAO}}$ is considerably smaller than the water volume $V_0 = A_{\text{lip}} D_{\text{w}}/2 = n_{\text{w}} v_{\text{w}}^0$ in almost the entire hydration range. Urea exhibits more complex behavior, with $V_{\text{GDS}}^{\text{urea}} > V_0$ at most hydration levels and $V_{\text{GDS}}^{\text{urea}} \lesssim V_0$ at very high hydration. Except for very low hydration levels, $V_{\text{GDS}}^{\text{NaCl}}$ remains almost equal to V_0 due to a compensation of the increasing surface excess and the decreasing area per lipid upon dehydration (see fig. 3.4B), noting once more that this result is specific to the Berger forcefield.

3.2.4 Area per Lipid

The area per lipid in multilamellar membrane systems is known to be affected by the hydration level [28, 119]. Figure 3.4A shows experimental data from the literature on A_{lip} for DMPC as a function of n_{w} [119]. Our simulations show agreement with the experimental data within about 10 % and also reproduce the observed decrease of the lipid area upon dehydration. Remaining deviations must be attributed to forcefield limitations and possible systematic errors introduced in the experimental procedures. For POPC, the agreement between experiments [126] and simulations is similar (see fig. 3.4B).

Figure 3.4B shows the hydration dependence of A_{lip} in presence of co-solutes as obtained in the simulations with POPC bilayers. It is seen that TMAO significantly decreases A_{lip}, by about 2-3 Å^2, while urea increases A_{lip} by a comparable increment, depending on the hydration level. NaCl has the strongest effect. It decreases A_{lip} by about 7-8 Å^2 for all hydration levels. A simple Gibbs adsorption model, associating a positive surface excess with an increase in A_{lip} and a negative surface excess with its decrease, qualitatively predicts the effect of TMAO and urea at most hydration levels. This model however neglects co-solute-induced variations in the lipid chemical potential and is thus of limited predictive power. In fact, it fails to predict the NaCl-induced decrease of A_{lip}, which is in line with earlier indirect experimental evidence [122, 127] and can be attributed to a condensation due to local charge compensation [121, 128].

3.2.5 Modeling Co-Solute Effects on the Hydration Repulsion

As shown in a paper related to this thesis [25] (Ref. [v]), urea and TMAO are confined in the aqueous layer between the membrane surfaces in a wide range of osmotic pressures. This scenario is imposed by construction in the MD simulations in the present Chapter and found to reproduce the experimental data (see above). Dehydration of the co-solute-loaded membranes is thus associated with an increase in the local co-solute concentration in the water-slab model, which in turn exerts a repulsive pressure $\Delta\Pi$
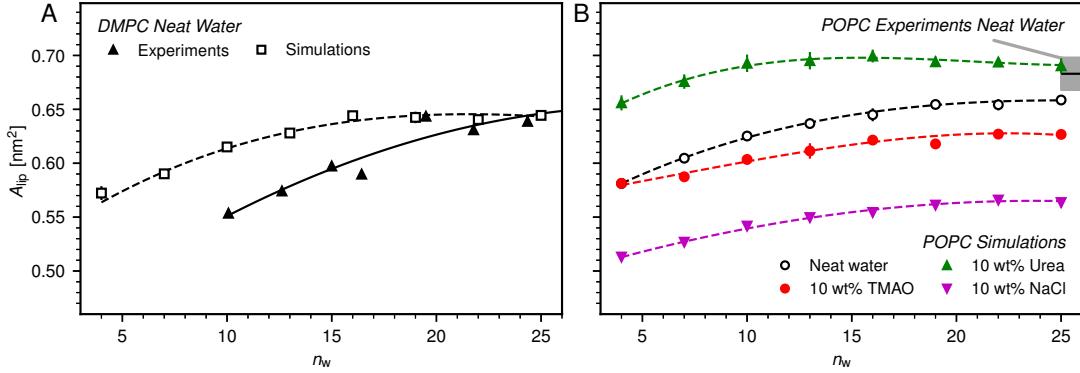
Figure 3.4: A: Average area per lipid, A_{lip}, in DMPC membranes without added co-solutes as a function of the hydration level, as reported in the experimental literature [119] (triangles) and as obtained from the simulations in the present Chapter (squares). B: Influence of 10 wt% TMAO, urea, or NaCl on A_{lip} as observed in simulations of POPC bilayers. Experimental data from the literature for fully hydrated POPC bilayers in neat water is shown for comparison [126]. Lines are guides to the eye.

contributing to the surface interaction. Within an ideal mixing approximation this repulsive pressure is given by van't Hoff's law

$$\Delta\Pi_{\mathrm{ideal}}(n_{\mathrm{w}}) = k_{\mathrm{B}}T\frac{n_{\mathrm{cosol}}}{V_0(n_{\mathrm{w}})}, \qquad (3.6)$$

where n_{cosol} is the number of co-solute molecules per lipid and $V_0 = n_{\mathrm{w}}v_{\mathrm{w}}^0$ the associated solvent volume. The overall repulsive pressure $\Pi_{\mathrm{ideal}}^{\mathrm{theo}} = \Pi_{\mathrm{water}} + \Delta\Pi_{\mathrm{ideal}}$, is indicated with dotted lines in fig. 3.5, where Π_{water} is an exponential fit to the *hydration repulsion* simulation data in pure water for $n_{\mathrm{w}} < 19$. The obtained decay lengths are $\lambda_{\mathrm{DMPC}} = 0.29$ nm and $\lambda_{\mathrm{POPC}} = 0.25$ nm, respectively, in reasonable agreement with the experimental results presented above. It is also seen that $\Pi_{\mathrm{ideal}}^{\mathrm{theo}}$ is in satisfactory agreement with the simulation data for membranes loaded with 10 wt% urea and NaCl but fails in the case of TMAO, where it underestimates the repulsive pressure by more than a factor of 2.

One necessary refinement directly follows from one of our earlier conclusions: The effective volume accessible to the co-solutes, V_{GDS}, deviates significantly from that of the solvent, V_0, meaning that eq. (3.6) needs to be augmented by a correction factor V_0/V_{GDS}. Another refinement concerns the co-solute osmotic coefficients, Φ, which substantially deviate from the ideal behavior ($\Phi = 1$) assumed in eq. (3.6). Figure 3.3D shows osmotic coefficients of urea, TMAO, and NaCl in a wide concentration range, determined in independent simulations and experiments performed by our collaborators from the Sparr group as described in Section 3.1.2. The data are in good agreement with experimental data from the literature for urea [124], TMAO [123], and NaCl [125],
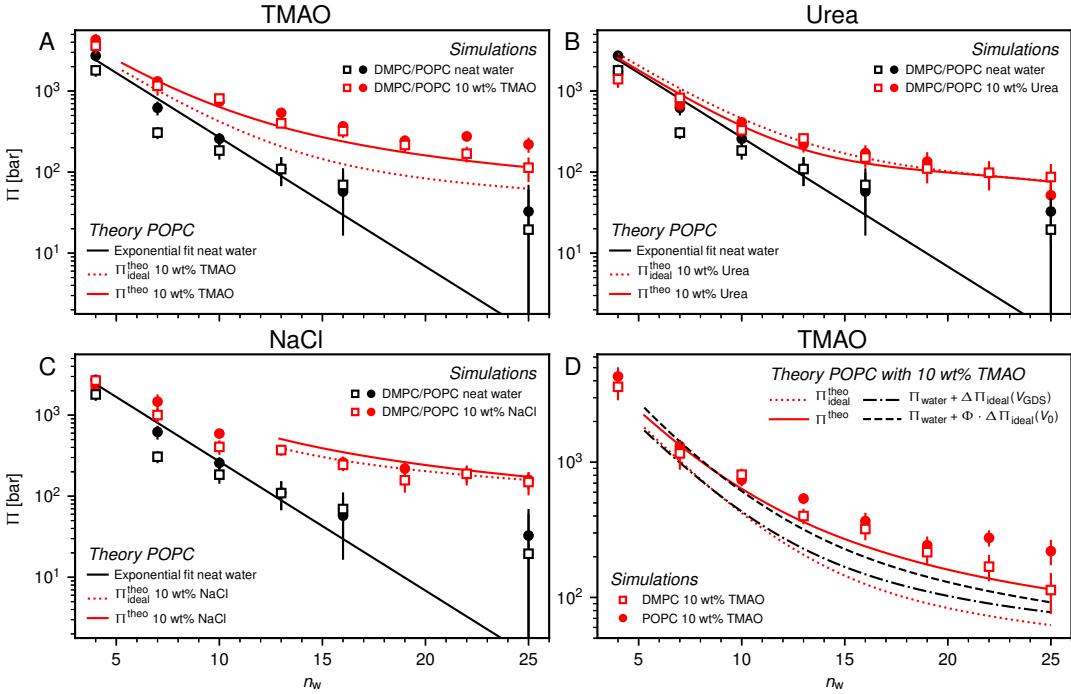
Figure 3.5: Pressure-hydration curves $\Pi(n_{\mathrm{w}})$ of PC membranes with and without added 10 wt% TMAO (panel A), urea (panel B), and NaCl (panel C) as obtained in the simulations. Black solid lines represent exponential fits to the simulation data for POPC without added co-solutes. Dotted and solid red lines indicate the predictions of theoretical models for POPC simulations, neglecting, eq. (3.6), and accounting, eq. (3.7), for effective volume and osmotic coefficient effects, respectively. Theoretical predictions are only shown for hydration levels for which the co-solute concentration is below the solubility limit. Panel D shows the influence of the effective volume and of the osmotic coefficient individually.

indicated in the figure with lines. Literature values were either computed from the reported water activity using eq. (3.1) or the given relation between the osmotic coefficients and the solute molality $b(x_{\mathrm{w}})$ was used directly (for details see Section 3.4.3 and Section 3.4.4 in the Appendix). The solution's osmotic coefficient and the more commonly used co-solute's activity coefficient γ, are related through the Gibbs-Duhem equation as $\ln(\gamma) = \Phi - 1 + \int_0^b (\Phi - 1)/b' db'$ (see also Secion 3.4.2 in the Appendix). The agreement between simulations and experimental data for TMAO and urea in fig. 3.3D is expected because the simulation forcefields have been developed with the aim to reproduce osmotic coefficients [106, 107]. The investigated co-solutes display different deviations from ideality: Φ_{TMAO} deviates the strongest, enhancing its osmolyte-capabilities, and Φ_{NaCl} is slightly larger than unity which is typical for salts. Finally,

urea forms near-ideal solutions in water.

Augmentation of eq. (3.6) by the co-solute osmotic coefficients and their accessible volume yields

$$\Delta\Pi(n_{\mathrm{w}}) = \Phi(n_{\mathrm{w}})k_{\mathrm{B}}T\frac{n_{\mathrm{cosol}}}{V_{\mathrm{GDS}}(n_{\mathrm{w}})}. \qquad (3.7)$$

Cubic splines were used to interpolate between data points for V_{GDS} in order to make eq. (3.7) continuous over the entire hydration range. For the osmotic coefficients $\Phi(n_{\mathrm{w}})$, the expressions reported in the literature [123–125] were used.

With these refinements, the theoretically predicted osmotic pressures $\Pi_{\mathrm{theo}} = \Pi_{\mathrm{water}} + \Delta\Pi$ fit well to the simulation data (see fig. 3.5). Remaining deviations likely originate from the neglect of other effects such as additional electrostatic repulsion in the case of NaCl [129] or other altered contributions to the perpendicular equation of state [130]. Overall, the agreement between eq. (3.7) and the simulation data demonstrates that the co-solutes' osmotic pressure is at the heart of the increase in the repulsion. Closer inspection (cf. fig. 3.5D) reveals that the osmotic coefficient is the dominant correction at low hydration, while excluded-volume and osmotic coefficient effects are equally important at higher hydration. It becomes clear that TMAO leads to the strongest repulsion because it exhibits unfavorable interactions with the membrane surfaces and at the same time a remarkably high osmotic coefficient. TMAO and the lipids' PC headgroups both have a dipolar/hydrophobic architecture. The high osmotic coefficient and the pronounced depletion at the membrane surfaces therefore likely have the same physical origin previously termed *dipolar/hydrophobic frustration* [106].

3.2.6 Thermodynamics of the Repulsion

The free energy of membrane dehydration, $G(n_{\mathrm{w}})$ (see Section 3.1.3), can be decomposed into its enthalpic and entropic contributions, $H(n_{\mathrm{w}})$ and $-TS(n_{\mathrm{w}})$, respectively, as was done earlier in experiments [101] and simulations [106] with satisfactory agreement. In the following, the influence of co-solutes on these individual contributions is discussed.

Figure 3.6A shows the enthalpy/entropy decomposition for DMPC membranes interacting across neat water, where the methodology of Schneck et al. [99] was used. It is seen that the repulsion is of entropic origin at larger hydration but crosses over to an enthalpy-driven regime at low hydration. The addition of co-solutes significantly increases the magnitude of both contributions as well as their antagonistic interplay. Figure 3.6B exemplarily shows the enthalpy/entropy decomposition of the free energy associated with the dehydration of membranes loaded with 10 wt% TMAO, for which the effect is most pronounced and for which complementary thermodynamic information is available [106]. The repulsion is seen to be enthalpic throughout the entire separation range. The entropic contribution is of opposite sign but sub-dominant.

Figure 3.6C compares experimental data obtained by our collaborators from the Sparr group (Lund University) and simulation data for the change $\Delta H' = H'_{\mathrm{5wt\%\ TMAO}} -$

H'_{water} in the differential enthalpy of hydration $H' = dH/dn_{\text{w}}$ when loading POPC membranes with 5 wt% TMAO. The comparison is valid only for relative humidities above $h_{\text{rel}} \approx 55\%$, because in the humidity range below that threshold (indicated with a dashed line style), TMAO forms a separate phase and POPC undergoes a phase transition in the experiments. In the meaningful humidity range (indicated with a solid line style), the simulation data semi-quantitatively agree with the experiments. In fact, the agreement looks even better when $\Delta H'$ is plotted as a function of the hydration level n_{w} (see fig. 3.12 in the Appendix).One should keep in mind, however, that in this representation, the water chemical potential deviates between experiments and simulations.

The pairwise mutual repulsion between TMAO molecules in water was reported to be of enthalpic origin [106] (see fig. 3.6D) and the dehydration of TMAO-loaded membranes is associated with a reduction in the average TMAO/TMAO distance. The enthalpic character of the repulsion between TMAO-loaded membranes can therefore be attributed to the enthalpic character of the TMAO/TMAO mutual repulsion. In fact, the interaction thermodynamics appear dominated by the dehydration of the confined TMAO solution. To take this concept to a quantitative level, the dehydration thermodynamics of TMAO-loaded lipid membranes is approximated in the following as a linear combination of the dehydration thermodynamics of pure membrane dehydration ($G_{\text{lip}}^{\text{theo}}$, $H_{\text{lip}}^{\text{theo}}$, and $S_{\text{lip}}^{\text{theo}}$) and of the thermodynamics of the TMAO/TMAO pairwise interaction ($G_{\text{TMAO}}^{\text{theo}}$, $H_{\text{TMAO}}^{\text{theo}}$, and $S_{\text{TMAO}}^{\text{theo}}$),

$$G^{\text{theo}}(n_{\text{w}}) = G_{\text{lip}}^{\text{theo}}(n_{\text{w}}) + k \cdot G_{\text{TMAO}}^{\text{theo}}(n_{\text{w}}) \tag{3.8a}$$

$$H^{\text{theo}}(n_{\text{w}}) = H_{\text{lip}}^{\text{theo}}(n_{\text{w}}) + k \cdot H_{\text{TMAO}}^{\text{theo}}(n_{\text{w}}) \tag{3.8b}$$

$$S^{\text{theo}}(n_{\text{w}}) = S_{\text{lip}}^{\text{theo}}(n_{\text{w}}) + k \cdot S_{\text{TMAO}}^{\text{theo}}(n_{\text{w}}), \tag{3.8c}$$

where k is a weighting coefficient discussed further below. The contributions of the TMAO/TMAO pairwise interaction were computed by averaging $H_{\text{PMF}}(r)$, $G_{\text{PMF}}(r)$, and $S_{\text{PMF}}(r)$ in fig. 3.6D over the hydration-dependent distribution $p(r, n_w)$ of TMAO-TMAO pair distances r (for details see fig. 3.13 in the Appendix),

$$G_{\text{TMAO}}^{\text{theo}}(n_{\text{w}}) = \int_0^\infty G_{\text{PMF}}(r) \cdot p(r, n_{\text{w}}) dr \tag{3.9a}$$

$$H_{\text{TMAO}}^{\text{theo}}(n_{\text{w}}) = \int_0^\infty H_{\text{PMF}}(r) \cdot p(r, n_{\text{w}}) dr \tag{3.9b}$$

$$S_{\text{TMAO}}^{\text{theo}}(n_{\text{w}}) = \int_0^\infty S_{\text{PMF}}(r) \cdot p(r, n_{\text{w}}) dr. \tag{3.9c}$$
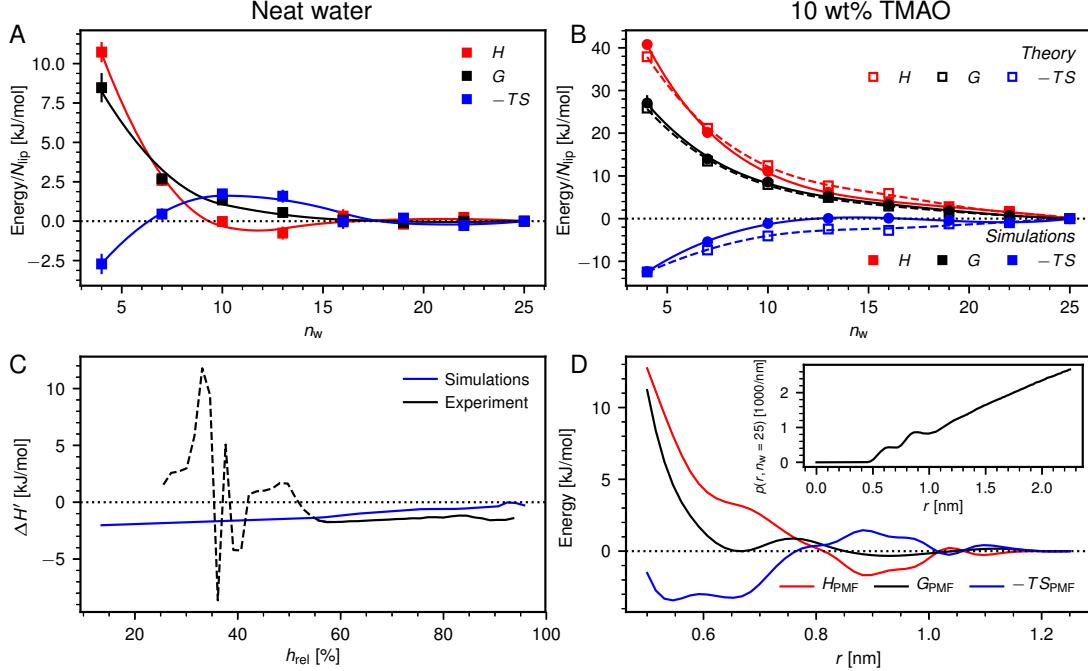
Figure 3.6: A: Decomposition of the dehydration free energy, $G(n_\mathrm{w})$, in DMPC membrane simulations without added co-solutes into enthalpic and entropic contributions, $H(n_\mathrm{w})$ and $-TS(n_\mathrm{w})$, respectively. Lines are guides to the eye. B: Same decomposition for DMPC membranes loaded with 10 wt% TMAO. Open squares are theoretical predictions according to eq. (3.8). C: Comparison between experiments from the Sparr group and simulations of POPC lipids, regarding the change $\Delta H'$ in the differential hydration enthalpy $H' = dH/dn_\mathrm{w}$ due to addition of 5 wt% TMAO. The comparison is only valid for humidities above $h_\mathrm{rel} \approx 55\%$ (indicated with a solid line style). D: Potential of mean force, $G_\mathrm{PMF}(r)$, for the TMAO-TMAO interaction in bulk solutions and its enthalpic and entropic contributions, $H_\mathrm{PMF}(r)$ and $-TS_\mathrm{PMF}(r)$, respectively. The TMAO-TMAO center-to-center radial distance is denoted with r. Data are reproduced from the literature [106]. Inset: Normalized TMAO-TMAO distance distribution $p(r, n_\mathrm{w})$ in DMPC membranes loaded with 10 wt% TMAO at $n_\mathrm{w} = 25$.

The inset of fig. 3.6D exemplary shows $p(r)$ for $n_\mathrm{w} = 25$. The distribution is normalized such that it amounts to the number of TMAO-TMAO pairwise interactions in the simulated system, N_TMAO^{pair},

$$\int_{0}^{\infty} p(r, n_\mathrm{w}) dr = N_\mathrm{TMAO}^{pair} = \frac{N_\mathrm{TMAO}(N_\mathrm{TMAO} - 1)}{2}. \tag{3.10}$$

Open symbols in fig. 3.6B indicate the predictions of eq. (3.8) after adjusting the weighting coefficient k to match the simulation data. The simultaneous satisfactory agreement of free energy, enthalpy, and entropy for a single coefficient suggests that the thermodynamics of the dehydration of membranes loaded with co-solutes can indeed be approximated as a linear combination of membrane dehydration in the absence of co-solutes and the co-solute pair-wise interaction. The best-matching weighting coefficients ($k_{\text{POPC}} = 2.23$ and $k_{\text{DMPC}} = 2.29$), however, significantly deviate from unity. This deviation can be attributed to the following shortcomings of eq. (3.8). Firstly, the interaction between TMAO molecules in concentrated solutions is a multi-body problem and deviates from the sum of pair-wise interactions. And second, eqs. (3.8) neglect interactions between TMAO and the PC headgroups of the lipids. These interactions are likely of similar nature as the TMAO/TMAO interactions, due to the dipolar/hydrophobic architecture of both TMAO and PC, and also comparable in number. Indeed, analysis of the temperature-dependence of the TMAO-membrane potential of mean force (PMF, see fig. 3.14 in the Appendix) indicates that the repulsion between TMAO and the membrane surface is driven by enthalpy. Such enthalpy-driven exclusion of uncharged solutes from macromolecular surfaces was earlier found to be important also for the stabilization of proteins by osmolytes [131].

3.2.7 Simulation Forcefield Influence

It has previously been suggested that the Berger lipid forcefield exhibits unrealistically high affinity for Na^+ ions. [122]. Indirect comparison to experimental data by means of the salt dependent head group order parameter suggests that the CHARMM36 lipid forcefield reproduces the salt adsorption more realistically [122]. In order to evaluate the robustness of the present simulation results with respect to the choice of the forcefields, additional simulations employing the CHARMM36 forcefield for the lipids and NaCl in combination with the TIP3P water model were performed. Figure 3.7A shows a comparison of the NaCl density profiles at the POPC interface for the Berger-based versus the CHARMM36-based forcefield combinations. Indeed, the Na^+ adsorption and thus the surface excess of NaCl (fig. 3.7B) and the accessible volume (fig. 3.7C) are significantly higher for the Berger-based forcefield combination. Additional simulations involving variation of the ion forcefield for each lipid forcefield confirm that the lipid forcefield is determining the strength of the Na^+-adsorption (see fig. 3.15 in the Appendix).

Figure 3.7D shows a comparison between experimental pressure-distance curves (POPC loaded with 5 wt% NaCl) and those predicted by the Berger-based and CHARM36-based forcefield combinations. It is apparent that, especially at larger membrane separations, the added repulsion due to the presence of NaCl is better captured by the CHARMM36-based forcefield combination and that this difference can be partially attributed to the difference in $V_{\text{GDS}}^{\text{NaCl}}$ (see fig. 3.7C and eq. 3.7).

Selected simulations with a CHARMM36-based forcefield combination (i.e., with the CHARMM36 lipid forcefield and TIP3P water) were also performed for the co-solutes
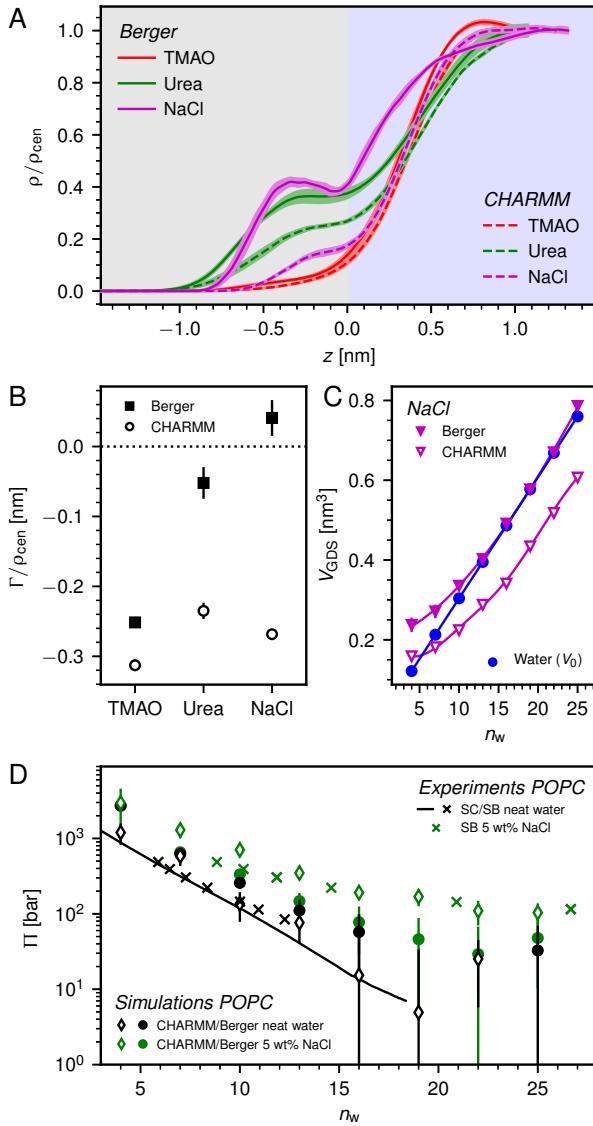
Figure 3.7: Analysis of the influence of the lipid forcefield. A: Density profiles of the respective co-solutes at the POPC lipid interface at high hydration ($n_\mathrm{w} = 25$). B: Co-solute surface excess at $n_\mathrm{w} = 25$ as obtained with both forcefield combinations. C: Hydration dependent accessible volume from NaCl simulations at the POPC interface for both forcefield combinations. The neat water volume V_0 is shown for comparison. Lines are guides to the eye. D: Pressure-distance curves obtained for both forcefield combinations in comparison to experimental data from the Sparr group.

TMAO and urea and compared to the results obtained with the Berger-based forcefield combination. As shown in fig. 3.7A and B, the influence of the forcefield is practically negligible for TMAO, the osmolyte most extensively discussed in this Chapter. For urea the agreement between the two forcefield combinations is only qualitative and consistent only with regard to the negative sign of the surface excess (see fig. 3.7B). It is, however, important to note that irrespective of any forcefield effects on the quantitative level, all simulations reproduce the repulsion-enhancement due to the presence of co-solutes at least semi-quantitatively (see fig. 3.2). More importantly, the physical insights into the repulsion mechanisms are gained from a self-consistent comparison between the simulation results and a theoretical model involving parameters determined with the same forcefields.

3.3 Conclusions

By combining sorption calorimetry and sorption balance experiments performed by our experimental collaborators with molecular dynamics simulations, the influence of TMAO, urea, and NaCl on the *hydration repulsion* between stacked phospholipid membranes was investigated. All studied co-solutes have been shown to enhance the repulsion. For a given level of dehydrating osmotic pressure, the presence of co-solutes leads to a higher hydration level, quantified by the number of water molecules per lipid. The co-solutes therefore do not only substitute for water molecules but additionally have a moisturizing effect in the literal sense. The simulations, which accurately reproduce the chemical potential of water, quantitatively match the experimental data from the Sparr group and provide detailed insight into the mechanism of the increased *hydration repulsion*.

The osmotic pressure afforded by the co-solutes confined in the aqueous layer between the membrane surfaces is found to be the source of the added repulsion. The strength of this effect depends crucially on the interaction of the co-solutes with the membrane surfaces and on the osmotic coefficient of the confined co-solute solution. For high enough co-solute concentrations, the thermodynamics of membrane dehydration is dominated by the thermodynamics of the dehydration of the co-solute solution. With that, the simulations provide the explanation for the remarkably strong moisturizing effect of the osmolyte TMAO, which exhibits highly unfavorable interactions with the membrane surfaces and at the same time a high osmotic coefficient.

3.4 Appendix to Chapter 3
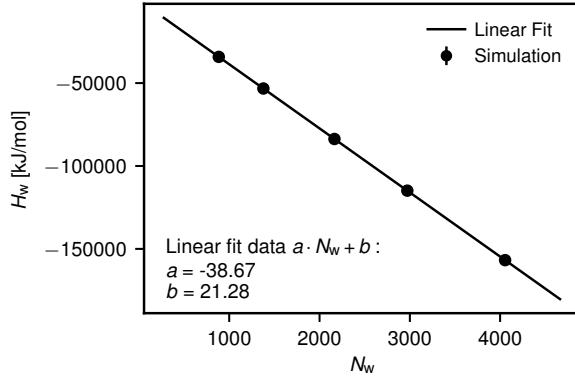
Figure 3.8: Measured enthalpy from simulations of water boxes of different sizes. From a linear fit to the measured data, the partial enthalpy of water is determined to be $dH_w/dN_w = -38.67$ kJ/mol.
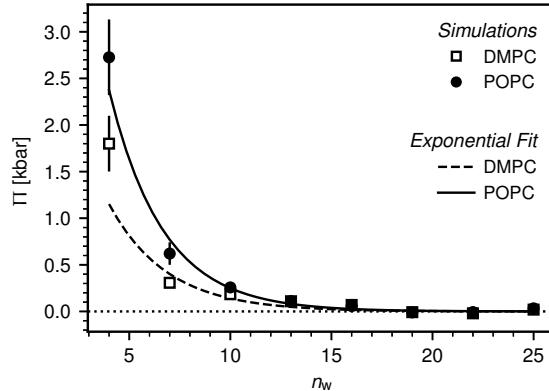
Figure 3.9: Pressure distance curves obtained in simulations for the two lipids shown in a linear scale. The reference potential μ_0 was obtained by averaging results for the water chemical potential for which $n_w > 19$ for simulations of DMPC and POPC. This is why only the average pressure for data points with $n_w > 19$ goes to zero.
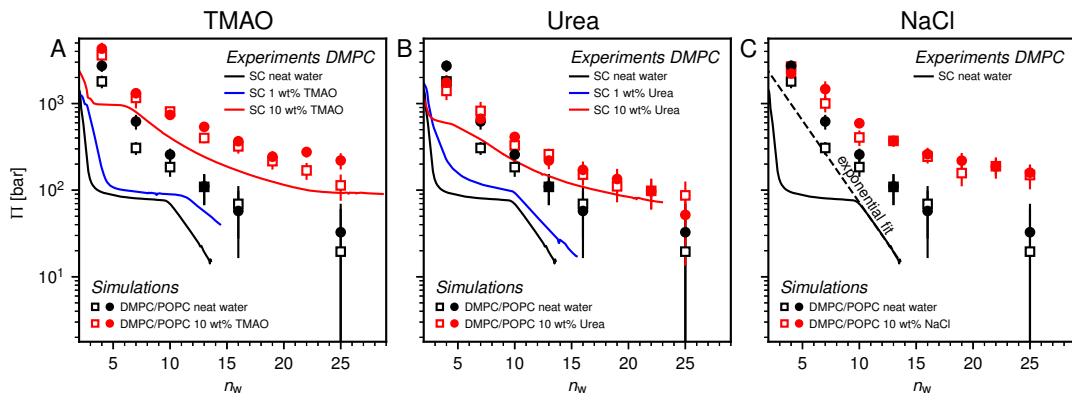
Figure 3.10: Interaction pressure between membrane stacks in solution with TMAO (A), urea (B) and sodium chloride (C) from sorption calorimetry (SC) experiments of DMPC lipids performed by the Sparr group and simulations of DMPC and POPC. Panel C additionally includes an exponential fit to the experimental data for $n_{\mathrm{w}} > 10$. Comparison between experimental data and simulation results for DMPC bilayers shows larger deviations at low hydration levels. This is due to a phase transition from the fluid like to the gel like phase in the experiments when reaching a hydration level below $n_{\mathrm{w}} \approx 10$.

3.4.1 Partial Volumes of Water and Lipids

The slope of the total system volume V_{tot} as a function of the number of water molecules per lipid molecule $n_w = N_w/N_{lip}$ remains constant for all observed systems (see fig. 3.11A). This implies that the partial volume of water $v_w = \partial V_{tot}/\partial N_w$ is unchanged in all simulations. Additionally, the volume per lipid molecule v_{lip} was computed from simulations as

$$v_{lip} = (V_{tot} - N_w \cdot v_w - N_i \cdot v_i)/N_{lip}, \qquad (3.11)$$

where v_i denotes the partial volume of the respective co-solutes and N_i is the number of co-solute molecules in the simulation. The partial volume of the specific co-solute was estimated by the volume increase between simulations with 1wt% and 10wt% of the co-solute at the same hydration level as $v_i \approx \Delta V_{tot}/\Delta N_i$.

Like the water partial volume, the lipid partial volume appears to remain constant throughout all simulation setups (see fig. 3.11B). Since the lipid area A_{lip} was found to be affected by hydration and addition of co-solutes (see Section 3.2.4), this suggests an elongation or contraction of the lipids along their axis, depending on the change in A_{lip}. A difference of about 3-4% is observed between values for the lipid volumes measured in our simulations and values from the experimental literature obtained using the neutral flotation method [132]. This discrepancy might be due to forcefield limitations.
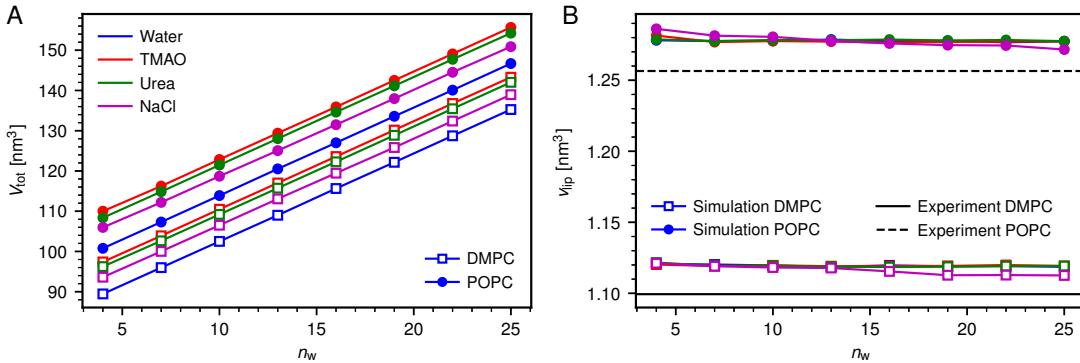
Figure 3.11: Volumes from simulations of binary membrane-water-systems and ternary co-solute-membrane-water systems with 10 wt% of co-solutes. A: Total system volume as a function of the hydration level. The decrease in system volume upon dehydration is constant for all simulated systems, suggesting a constant water partial volume v_w. B: Average volume per lipid molecule for different hydration levels of membrane systems with and without 10 wt% of co-solutes. The lipid volume seems to remain constant during dehydration, while the area per lipid was observed to decrease (cf. fig. 3.4). Experimental data is reported by Greenwood et al. [132].

3.4.2 Relation Between Osmotic Coefficients and Activity Coefficients

When using the definition of the osmotic coefficient Φ of eq. (3.1) from Section 3.1.2, one can express the water chemical potential μ_w in solution with a solute as

$$\mu_w = \Phi RT \ln(x_w) = -\Phi RT \ln(1 + M_w b) \approx -\Phi RT M_w b, \tag{3.12}$$

where M_w is the water molar mass and b is the molal concentration of the solute. The solute chemical potential μ_s is given by

$$\mu_s = RT\ln(\gamma b), \tag{3.13}$$

with the solute specific activity coefficient γ. The Gibbs-Duhem equation at constant pressure and temperature as a function of the solute molality results in the relation

$$bM_w\mathrm{d}\mu_s = -\mathrm{d}\mu_w. \tag{3.14}$$

Using eq. (3.12) and eq. (3.13) we can write the total differentials of μ_s and μ_w as

$$\mathrm{d}\mu_w = -RTM_wb \,\mathrm{d}\Phi - \Phi RTM_w \,\mathrm{d}b \tag{3.15a}$$

$$\mathrm{d}\mu_s = \frac{RT}{\gamma} \,\mathrm{d}\gamma + \frac{RT}{b} \,\mathrm{d}b. \tag{3.15b}$$

Now substituting eqs. (3.15) into eq. (3.14) we obtain

$$b\mathrm{d}\ln(\gamma) + \mathrm{d}b = \mathrm{d}(\Phi b). \tag{3.16}$$

Solving eq. (3.16) for $\mathrm{d}\ln(\gamma)$ and integrating then leads to the relation between activity coefficient and osmotic coefficient referred to in Section 3.2.5

$$\ln(\gamma) = \Phi - 1 + \int_0^b \frac{\Phi - 1}{b'} \,\mathrm{d}b'. \tag{3.17}$$

3.4.3 Osmotic Coefficients for TMAO

In order to obtain the osmotic coefficient of TMAO solutions at different concentrations $\Phi_{\text{TMAO}}(x_{\text{w}})$, the dependence of the water activity on the TMAO molality reported by Courtenay et al. [123] was used. For this, the relation between solute molality and water mole fraction $b(x_{\text{w}}) = (x_{\text{w}}^{-1} - 1)/M_{\text{w}}\nu$, where additionally $\nu_{\text{TMAO}} = 1$ was then substituted.

Together with eq. (3.1) from Section 3.1.2 this then yields the following expression

$$\Phi_{\text{TMAO}}(x_{\text{w}}) = \frac{M_{\text{w}}(b(x_{\text{w}}) + Ab(x_{\text{w}})^2)}{\ln(x_{\text{w}})}, \tag{3.18}$$

where $A = 0.18$ was obtained by Courtenay et al. [123] based on a quadratic fit to the water activity data. Equation (3.18) was then used to compute the TMAO osmotic coefficients for the augmented model of eq. (3.7) from Section 3.2.5.

3.4.4 Osmotic Coefficients for Urea and Sodium Chloride

For urea and sodium chloride, previously determined dependencies of the respective osmotic coefficients on the co-solute molality were obtained from the literature. These expressions were then transformed from the molality scale to the mole fraction scale using the relation $b(x_w) = (x_w^{-1} - 1)/M_w \nu$. Note that $\nu_{NaCl} = 2$. Additionally, the pre-factor $K = (x_w^{-1} - 1)/\ln(x_w^{-1})$ is introduced to account for the different reference potential used in the definition of the molality based osmotic coefficient $\Phi_b(b) = \Delta\mu/RT\nu M_w b$. This definition was used in the study by Stokes [124], whereas in this work we use the fractional osmotic coefficient $\Phi(x_w)$ as defined in eq. (3.1) of Section 3.1.2.

At $T = 25°C$ the relation reported by Stokes [124] leads to the following expression for the osmotic coefficient of an urea-water-solution

$$\Phi_{urea}(x_w) = K \left(1 - \frac{c_1 b(x_w)}{1 + c_2 b(x_w)} - \frac{c_3 b(x_w)^2}{(1 + c_2 b(x_w))^2} \right), \tag{3.19}$$

where values of $c_1 = 0.042783$, $c_2 = 0.15$ and $c_3 = 0.0004198$ were found to reproduce the osmotic coefficient correctly up to $b = 20$ mol/kg corresponding to $x_w \approx 0.74$.

For sodium chloride, osmotic coefficients were computed using the following relation based on the findings of Lang [125]

$$\Phi_{NaCl}(x_w) = K \left(1 - \frac{S_f \sqrt{d_0}}{A^3 b(x_w)} \left[1 + A\sqrt{b(x_w)} - 2\ln(1 + A\sqrt{b(x_w)}) - \frac{1}{1 + A\sqrt{b(x_w)}} \right] \right.$$
$$\left. + B b(x_w) + C b(x_w)^2 + D b(x_w)^3 \right), \tag{3.20}$$

where at $T = 25°C$ the following values of $S_f \sqrt{d_0} = 1.1705$, $A = 1.3924$, $B = 2.655 \cdot 10^{-2}$, $C = 9.60 \cdot 10^{-3}$ and $D = -0.96 \cdot 10^{-3}$ are reported. The derivation of eq. (3.20) is based on the Debye-Hückel limiting law for the activity coefficient, which is then transformed to the osmotic coefficient using eq. (3.17) [125].
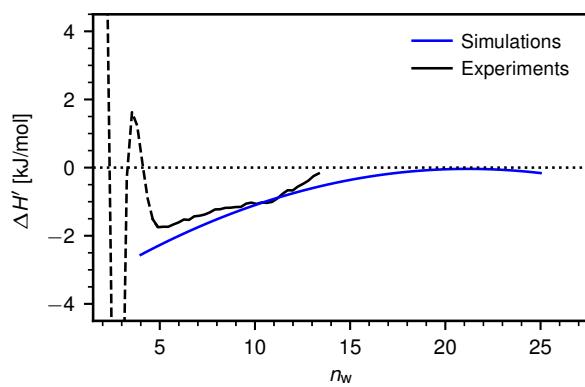
Figure 3.12: Comparison between differential enthalpies $\Delta H' = H'_{5\text{wt\% TMAO}} - H'_{\text{water}}$ (see Section 3.2.6) from sorption calorimetry experiments performed by the Sparr group and MD simulations of POPC lipids. The difference between the differential enthalpies obtained in setups with 5 wt% TMAO and pure water was computed at the same hydration level n_{w}. Dashed lines indicate regimes where TMAO forms a separate phase and POPC undergoes a phase transition in experiments.
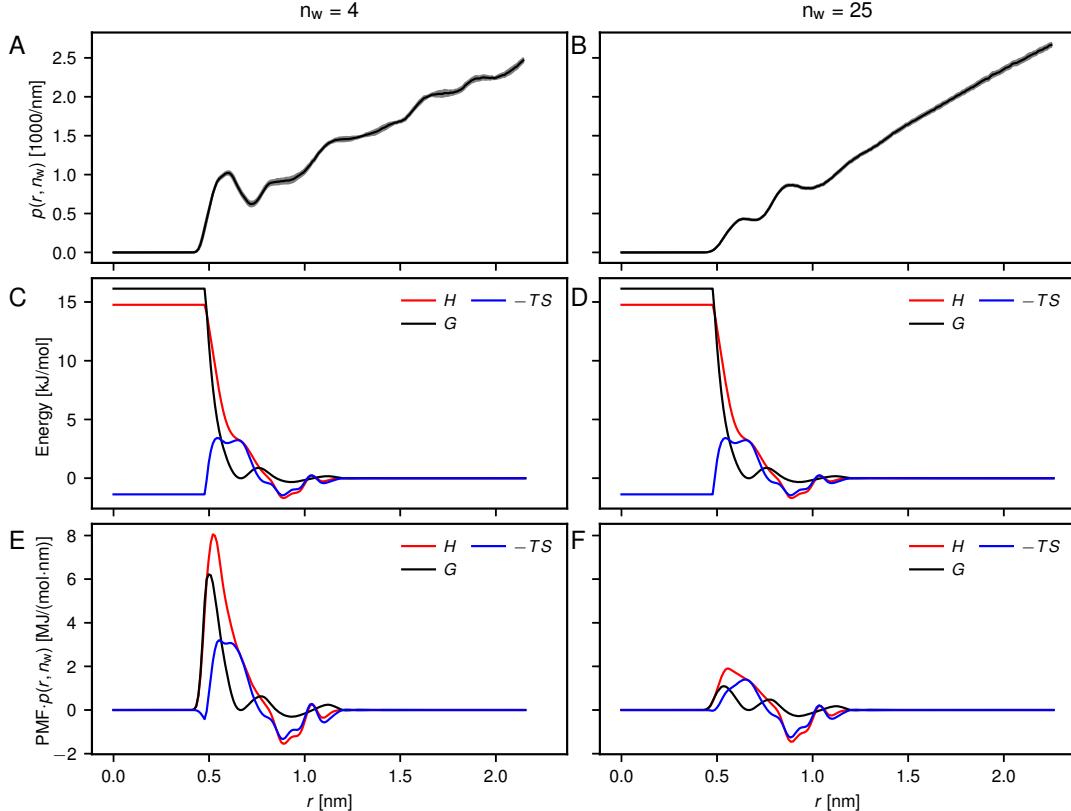
Figure 3.13: Details for the computation of the linear combination of the water-membrane and water-TMAO systems for DMPC, shown exemplary for two hydration levels $n_{\mathrm{w}} = 4$ and $n_{\mathrm{w}} = 25$. A&B: Normalized distribution of TMAO-TMAO separations as observed in DMPC simulations with 10 wt% of TMAO. Data are averaged over five independent simulations and the standard error is indicated as the area shaded in grey. C&D: Potential of mean force for TMAO in water as reported by Schneck et al. [106]. For separations below the smallest measured value, the PMF was taken to be constant. E&F: Product of respective PMF components and TMAO-TMAO separation distribution, which was then used to compute the theoretical contributions of pairwise TMAO-TMAO interactions to the free energy of the TMAO loaded membranes (see eqs. (3.9) of Section 3.2.6).
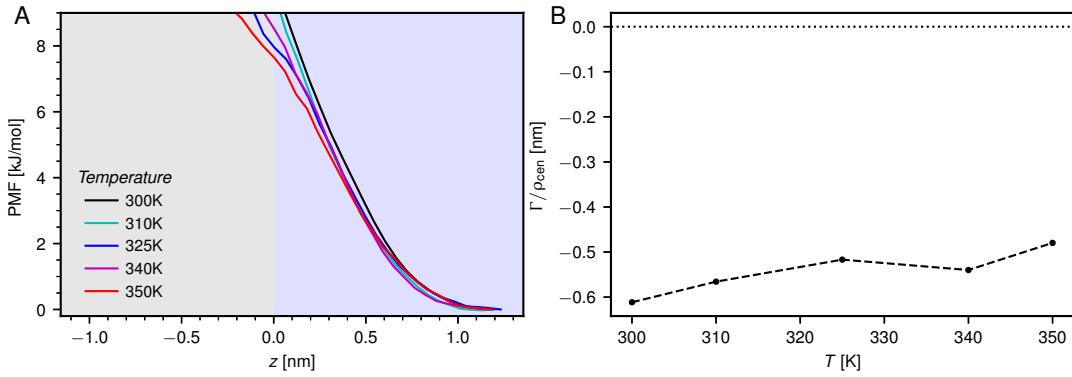
Figure 3.14: A: Potential of mean force (PMF) between the DMPC lipid interface and TMAO molecules at different temperatures. The DMPC-TMAO PMF was estimated from density profiles $\rho_{\mathrm{TMAO}}(z)$ obtained from simulations with 1wt% of TMAO, by using the identity $\mathrm{PMF}(z) = -k_{\mathrm{B}}T\ln(\rho(z)/\rho_{\mathrm{cen}})$. B: Temperature dependent surface excess of TMAO at the DMPC interface from simulations with 1wt% of TMAO. The computation of Γ was performed as defined in eq. (3.4) in Section 3.2.3. Assuming temperature-independent enthalpic and entropic contributions, the decreasing repulsion with increasing temperature indicates entropic attraction over-compensated by enthalpic repulsion. Similarly, a decreasing range of the repulsion between co-solutes and surfaces has previously been associated with enthalpy-driven depletion forces. [131].
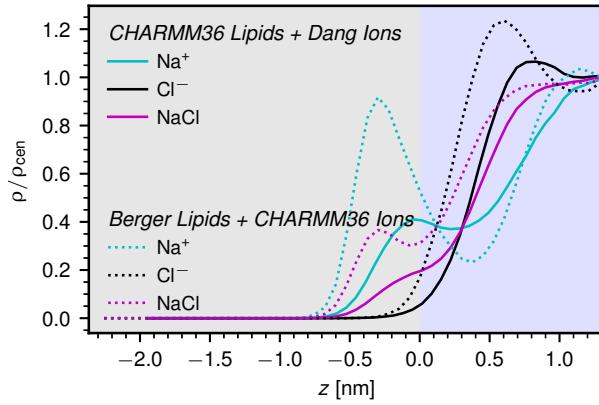
Figure 3.15: In order to evaluate the relative importance of the ion and the lipid force-fields regarding the observed Na^+ adsorption to the membrane surfaces, two different forcefield setups were analyzed. The CHARMM36 forcefield for the lipids [109] in combination with the Dang NaCl forcefield [108] together with the TIP3P water model [111, 112] on the one side are compared to a Berger lipid [104] and CHARMM36 NaCl system [110] in SPC/E water [105] on the other side. We find that regardless of the NaCl forcefield used (Dang or CHARMM36) the Na^+ adsorption is much stronger for the Berger lipids, compared to the CHARMM36 lipids.

Chapter 4

Interplay of Specific Ion and Impurity Adsorption Determines Zeta Potential of Phospholipid Membranes

Bibliographic information:
Parts of this Chapter have previously been published under Ref. [iii].

Cellular membranes are mainly comprised of phosphatidylcholine (PC) lipids [6] and are in living matter in contact with salt solutions on the intra- and extracellular side. It is thus not surprising that ion-membrane interactions, often mediated through membrane proteins and involving calcium, play a crucial role in a plethora of biological processes, ranging from cellular signaling cascades to the production of ATP in mitochondria [133]. Direct ion-lipid interactions have been shown to be of importance, for instance in the initiation of immune responses [134]. The prime experimental method for the study of ion-lipid interactions is the measurement of the so-called ζ-potential of lipid vesicles in electrophoresis experiments. Since the ζ-potential approximates the electrostatic potential at the shear plane, its sign and magnitude is an indication for the effective surface charge and thus reflects ionic adsorption. The observed increase of the ζ-potential of lipid vesicles with increasing concentration of different salt types has been interpreted as a sign for generic cationic attraction to the lipid interface [135, 136], which has been partly confirmed by FCS and NMR experiments [121, 137]. Interestingly, however, studies of zwitterionic net-neutral PC-lipid vesicles commonly report negative ζ-potential values at vanishing salt concentrations, which seems to contradict the assumption of the ζ-potential being generated solely through ionic adsorption [135, 138]. Possible explanations that have been put forth to resolve this paradox include the orientation of the lipid headgroups at the interface [139], polarization effects [140] and, most importantly, the presence of negatively charged impurities [141, 142]. In fact, the relevance of impurities has been demonstrated for a wide range of different interfacial phenomena [143–148] and has recently been used to explain the negative ζ-potential of hydrophobic surfaces [37].

In this Chapter we analyze the influence of combined specific ion and impurity adsorption on the ζ-potential of the lipid-water interface. We first perform atomistic molecular dynamics simulations of PC-lipid bilayers in salt solutions under tangen-

tially applied electric fields. Here we find that the induced electroosmotic flow and thus the obtained value of the ζ-potential strongly depends on the specific type of ions in solution, and, for the cases where data is available, matches previous reports from simulations [149]. However, for all salt solutions the ζ-potential is found to be significantly larger (i.e. more positive) than reported in experimental studies [138]. In a second step, we employ a continuum model based on the modified Poisson-Boltzmann and Helmholtz-Smoluchowski equations, which includes effective specific ion-membrane interaction potentials, the effective dielectric profile at the lipid-water interface as well as the interfacial viscosity profile, which are all extracted from our simulations. We show that the assumption of the presence of anionic impurities, in amounts much lower than the reported purity levels of lipids and salts used in experiments, can explain the experimental data. This indicates that the presence of impurities in experiments, introduced through the addition of salts but presumably also already present in the lipids and the lab water, might crucially influence the measurement of ζ-potentials at the PC-lipid interface. The presence of impurities is thus suggested to be a major factor when interpreting or modeling experimentally measured ζ-potentials.

4.1 Methodology

4.1.1 Molecular Dynamics Simulations

Atomistic molecular dynamics (MD) simulations of palmitoyl-oleoyl-phosphatidylcholine (POPC) lipid bilayers in contact with NaCl, KCl and CaCl$_2$ salt solutions are performed as described in Chapter 3. Using the *GROMACS 2020.2* software package [103], the *CHARMM36* forcefield is employed for both, the lipids and the ions [109, 110], in combination with the TIP3P water model [111, 112]. Lipid bilayers are composed of $N_{\text{lip}} = 72$ lipid molecules, 36 per leaflet. Simulations are run in the NpT-ensemble at $T = 300$ K and atmospheric pressure of $p = 1$ bar. Temperature is controlled using the velocity-re-scaling-thermostat [113] with a time constant of $\tau_T = 0.5$ ps, while for the pressure the Berendsen barostat [114] is employed with semi-isotropic pressure coupling, using a time constant of $\tau_p = 1$ ps and a compressibility of $\kappa = 4.5 \cdot 10^{-5}$ bar^{-1}. The simulation time-step is $\Delta t = 2$ fs. Long-range charge interactions are modeled using the particle-mesh-Ewald (PME) method [115] and van der Waals interactions are described by shifted Lennard-Jones potentials decaying to zero at the cut-off. For both, electrostatics and van der Waals interactions, a real space cut-off radius of $r_c = 0.9$ nm is used. Periodic boundary conditions are employed in all directions, and systems are simulated at membrane separations of $D_w \approx 7$ nm, large enough for the two electric double layers to not overlap. For analysis of the ζ-potential, an electric field $E_{\parallel}$ is applied parallel to the surface of the lipid interface. A comparably low nominal field strength of $E_{\parallel} = 0.05$ V/nm is used at all salt concentrations, to make sure that the system is within the linear response regime (see Section 4.4.1 in the Appendix to this Chapter). Systems are equilibrated for 500 ns before applying the electric field and starting the production runs, which last at least another 1 μs.

4.1.2 Electrostatic Potentials from Simulations

The laterally averaged perpendicular displacement field $D_\perp$ due to the ions is defined as

$$D_\perp(z) = \Delta m_\perp(z) + \varepsilon_0 \Delta E_\perp(z), \tag{4.1}$$

where ε_0 is the vacuum permittivity, $\Delta m_\perp = m_\perp - m_{\perp,0}$ is the difference in the perpendicular polarization density between the system in the absence, $m_{\perp,0}$, and in the presence, $m_\perp$, of the ions and $\Delta E_\perp$ denotes the difference in the perpendicular electric field. It can also be computed from the ionic charge density ρ_{ion} as

$$D_\perp(z) = \int_{D_w/2}^{z} \rho_{\mathrm{ion}}(z') \, dz', \tag{4.2}$$

where $D_w/2 \approx 3.5$ nm is the center of the water slab. Similarly, the polarization density is obtained via [150]

$$m_\perp(z) = - \int_{D_w/2}^{z} \rho_b(z') \, dz', \tag{4.3}$$

where ρ_b is the bound charge density due to lipids and water.

For most media, the polarization density $m_\perp$ is linear in the electric field, and the constant of linearity is termed the electric susceptibility $\chi_\perp$. At interfaces the susceptibility is anisotropic and position dependent [150] so that

$$m_\perp(z) \cong \varepsilon_0 \chi_\perp(z) E_\perp(z). \tag{4.4}$$

Instead of the susceptibility, one commonly refers to the dielectric response $\varepsilon_\perp = 1 + \chi_\perp$. From eq. (4.1) and eq. (4.4), it follows that the D-field and E-field are related as

$$\Delta E_\perp(z) \cong \varepsilon_0^{-1} \varepsilon_\perp^{-1}(z) D_\perp(z), \tag{4.5}$$

where $\varepsilon_\perp^{-1}(z)$ is the inverse local dielectric response and ε_0 is the vacuum permittivity. The locality assumption in eq. (4.5) only holds if the displacement field is constant, but is a good approximation also when the displacement field varies slowly in space (i.e. at low salt concentrations) [151].

The definition of the electrostatic potential $\varphi(z) := - \int_{D_w/2}^{z} \Delta E_\perp(z') dz'$, together with eq. (4.1) and eqs. (4.2)&(4.3) leads to the following equation

$$\varphi_\rho(z) := - \int_{D_w/2}^{z} \int_{D_w/2}^{z'} \Delta\rho_b(z'') + \rho_{\mathrm{ion}}(z'') \, dz'' \, dz', \tag{4.6}$$

where the label φ_ρ indicates the computation based on the charge densities ρ_{ion} and ρ_b. We note here that $\Delta\rho_b = \rho_b - \rho_{b,0}$ is the difference in the density of bound charges between simulations with ions and in neat water, in contrast to previous definitions [149].

When assuming linear response according to eq. (4.5) one obtains the following alternative expression for the electrostatic potential

$$\varphi_\varepsilon(z) := -\varepsilon_0^{-1} \int_{D_w/2}^{z} \varepsilon_\perp^{-1}(z') \int_{D_w/2}^{z'} \rho_{\text{ion}}(z'') \, dz'' \, dz', \tag{4.7}$$

the label φ_ε again being chosen since the potential is computed from the inverse dielectric constant $\varepsilon_\perp^{-1}$. In Section 4.2.1 we will apply the two expressions for the electrostatic potential of eq. (4.6) and eq. (4.7) on data from atomistic molecular dynamics simulations and compare the obtained results.

4.2 Results and Discussion

The ζ-potential is a measure for the electrostatic potential at the shear surface, which for a neutral surface such as the PC-lipid interface is due to the adsorption of charges, and is determined experimentally by measuring the mobility of lipid vesicles when applying an electric field. In this Chapter we determine ζ-potentials from atomistic molecular dynamics simulations of PC-lipid bilayers. For this, we apply a tangential electric field, which induces a relative motion between the lipid interface and the salt solution, allowing for determination of the electrophoretic mobility in analogy to the experimental scenario (see fig. 4.1A).

The hydrodynamic flow at the lipid interface in the absence of a pressure gradient is governed by the Stokes equation

$$\frac{d}{dz}\left[\eta_\perp(z)\frac{du(z)}{dz}\right] = -E_\parallel \rho_{\text{ion}}(z). \tag{4.8}$$

Here $\eta_\perp(z)$ is the viscosity at position z, $u(z) = u_{\text{sol}}(z) - u_{\text{lip}}$ is the velocity of the solution $u_{\text{sol}}(z)$ relative to that of the lipid bilayer u_{lip}, and $E_\parallel$ is the electric field parallel to the lipid interface (for details see Section 4.4.1 in the Appendix to this Chapter). The charge density ρ_{ion} is due to the free charges only, i.e. the ions in solution, since bound charges only change their orientation in an electric field but do not cause a net electroosmotic flow [152]. Integrating both sides of eq. (4.8) leads to

$$\eta_\perp(z)\frac{du(z)}{dz} = -E_\parallel \int_{D_w/2}^{z} \rho_{\text{ion}}(z') \, dz'$$
$$= -E_\parallel D_\perp(z), \tag{4.9}$$

where $z = D_w/2$ is the center of the water slab between the lipid bilayers and where we used eq. (4.2). We also employed the boundary condition of vanishing stress in the bulk solution $du(D_w/2)/dz = 0$. After multiplication with the inverse dielectric response profile and another integration we obtain the following relation

$$\varphi_\eta(z) := \int_{D_w/2}^{z} \varepsilon_\perp^{-1}(z') \frac{\eta_\perp(z')}{E_\parallel \varepsilon_0} \frac{du(z')}{dz} \, dz' \tag{4.10}$$

$$= -\varepsilon_0^{-1} \int_{D_w/2}^{z} \varepsilon_\perp^{-1}(z') D_\perp(z') \, dz' \overset{!}{=} \varphi_\varepsilon(z),$$

which is an alternative expression for the electrostatic potential of eq. (4.7). According to eq. (4.10), φ_η is determined by the solution viscosity profile $\eta_\perp(z)$, which can be estimated from simulations by inverting eq. (4.9) (see Section 4.4.2 in the Appendix for details).

In experimental electrophoresis studies, the dielectric response and solution viscosity are usually approximated by the constant experimental bulk values $\varepsilon_\perp(z) = \varepsilon_{exp} = 80$ [153] and $\eta_\perp(z) = \eta_{exp} = 1$ mPas [154], in which case eq. (4.10) reduces to

$$\varphi_u(z) := \frac{\eta_{exp}}{\varepsilon_{exp}\varepsilon_0 E_\parallel} \left[u(z) - u_0 \right], \tag{4.11}$$

where $u_0 := u(D_w/2)$ is the velocity of the bulk solution.

The potential at the shear surface $z = 0$, where the solution velocity vanishes, is called the ζ-potential. The well known Helmholtz-Smoluchowski expression for the ζ-potential [155, 156] is thus obtained from eq. (4.11) by evaluating it at the interface

$$\zeta := \varphi_u(z = 0) = -\frac{\eta_{exp}}{\varepsilon_{exp}\varepsilon_0 E_\parallel} u_0, \tag{4.12}$$

where the no-slip boundary condition $u(z = 0) = 0$ was used. The bulk solution velocity $u_0 = u(D_w/2) = u_{sol}(D_w/2) - u_{lip}$ describes the relative movement between lipid bilayer and salt solution.

4.2.1 Electrophoresis in Molecular Dynamics Simulations

Figure 4.1B and C show mass and number densities across the lipid-solution interface as obtained from simulations with a bulk NaCl concentration of $c_{salt} = 0.44$ M, computed from the value of the sodium chlorine density distribution at the center of the water slab, and an electric field of $E_\parallel = 0.05$ V/nm applied parallel to the interface. The data is shown with the Gibbs dividing surface positioned at $z = 0$, which, as in Chapter 3, is the position where the water surface excess vanishes and is determined as

$$z_{GDS} = z_{lip} + \int_{z_{lip}}^{D_w/2} \left[1 - \frac{\rho_w(z)}{\rho_w(D_w/2)} \right] \, dz. \tag{4.13}$$

Here z_{lip} denotes the center of the lipid bilayer, $z = D_w/2$ is the center of the water slab and $\rho_w(z)$ is the water density profile.

A small peak in the distribution of the sodium ions in the lipid headgroup region, below the Gibbs dividing surface, is apparent, in agreement with the observations of
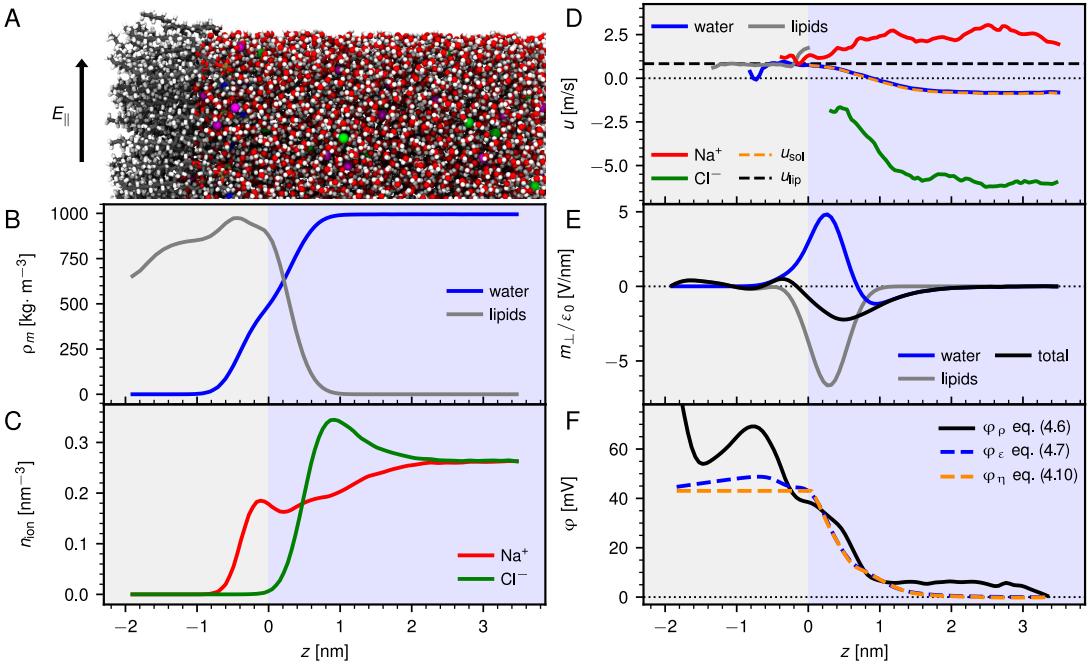
Figure 4.1: A: Screenshot from simulations of a POPC lipid bilayer in a $c_{salt} = 0.44$ M sodium chlorine solution, only one half of the simulation system is shown. An electric field parallel to the interface of $E_\parallel = 0.05$ V/nm is applied. Chlorine ions are shown in green and sodium ions are magenta colored. B: Mass density profiles of the lipid and water molecules across the interface. C: Ionic number density profiles across the interface. A peak in the distribution of sodium ions is observed below the Gibbs dividing surface, in agreement with the results of Chapter 3. D: Average center of mass velocity per molecule across the interface. The ions are set in motion due to the applied electric field and cause a hydrodynamic flow of the water molecules. The mass averaged solution velocity u_{sol} (dashed orange line) and the average lipid velocity u_{lip} (dashed black line) are shown as well. The velocity profiles have been smoothed by a sliding window average. E: Polarization field $m_\perp/\varepsilon_0$ due to the dipolar lipid (grey) and water (blue) charge densities according to eq. (4.3). The significant negative contribution due to the lipids is only partly compensated by the oriented water molecules, leading to a net negative polarization field (black) at the interface, as has been described previously [26]. F: Electrostatic potential computed using different approaches. The potential φ_ρ (continuous black line) is calculated from the ionic and bound charge densities according to eq. (4.6), while the potential φ_ε (dashed blue line) assumes linear response, taking the dielectric response profile into account according to eq. (4.7). The potential φ_η (dashed orange line) is computed from the solution velocity, assumes linear dielectric response and uses the viscosity profile according to eq. (4.10). Background coloring indicates the position of the Gibbs dividing surface.

Chapter 3. The fact that the peak in the chlorine distribution on the other hand is located above the Gibbs dividing plane, leads to a charge separation across the interface and thus is at the heart of the mechanism responsible for a finite ζ-potential at charge-neutral lipid bilayers in the presence of salt. This distinct shape of the ionic profiles represents a net positive charge at the interface due to Na^+ accumulation, followed by a diffuse cloud of neutralizing Cl^- counter-ions, which means that the lipid interface acts as an elecrophoretic positively charged surface.

Figure 4.1D shows the results obtained for the molecular center-of-mass velocity profiles. Movement of the ions due the applied field is observed, with a larger net velocity for the chlorine ions caused by their higher mobility in water [157]. The mass averaged solution velocity $u_{\mathrm{sol}}(z) = \sum_i u_i(z) \cdot \rho_i(z) / \sum_i \rho_i(z)$, where the sum extends over both ions and the water molecules, is shown as the orange dashed line and is almost identical to the pure water velocity profile (blue line). In the water slab u_{sol} is negative in sign, i.e. in opposite direction as the applied field, which means that the chlorine ions drag the water molecules along, leading to a substantial bulk flow velocity of $u_{\mathrm{sol}}(D_w/2) = -0.87 \pm 0.26$ m/s. A net movement of the lipid interface due to the bounded sodium ions in the headgroup region is observed with an equal but opposite average velocity of $u_{\mathrm{lip}} = +0.87 \pm 0.45$ m/s, indicated as the black dashed line. We note that the similarity of the magnitudes of the two velocities is coincidental and only obtained for the specific simulation shown in fig. 4.1.

The polarization density generated by the charge distribution of the lipid and water molecules $m_\perp$ is obtained according to eq. (4.3). As shown in fig. 4.1E, a significantly negative polarization field is generated by the lipid charges at the interface which is partially compensated by oriented water molecules. This apparent negative charge of the lipid interface has recently been investigated in a study related to this thesis [26] (Ref. [vi]) and is important in influencing the ion-lipid interaction potentials (see below), for which the water contribution has been shown to be less relevant [158]. The polarization at the interface is thus one of the underlying reasons for the distinct shape of the electric double layer shown in fig. 4.1C.

The electrostatic potential at the lipid interface obtained by different methods is shown in fig. 4.1F. The profile of the potential φ_ρ, computed from the charge densities according to eq. (4.6), is shown as the black continuous line and follows in its shape the solution velocity profile of fig. 4.1D, increasing from the bulk solution towards the lipid interface. The potential φ_ε is computed from eq. (4.7), using the smoothed dielectric response profile (see fig. 4.2A below) and is shown as the blue dashed line. Good agreement between the profiles of φ_ε and φ_ρ is observed for the largest part outside of the bilayer, indicating that the assumption of linear local dielectric response according to eq. (4.5) holds surprisingly well. The electrostatic potential φ_η according to eq. (4.10) is computed from the solution velocity profile $u_{\mathrm{sol}}(z)$ and a fit to the solution viscosity profile $\eta(z)$ (see fig. 4.2B below) and is shown as the dashed orange line in fig. 4.1F. Below the Gibbs dividing surface, $z < 0$, the solution velocity u_{sol} is constant in accord with the no-slip boundary condition, resulting in an infinite solution viscosity for $z < 0$ in our viscosity model (see below). As is apparent from fig. 4.1F,

the overall shape of the electrostatic potential is conserved, regardless of the specific method of computation. This means that not only linear dielectric response is valid and described by the dielectric profile $\varepsilon_\perp(z)$, but also that the hydrodynamic shear-stress relation described by the viscosity profile $\eta_\perp(z)$ holds.

The inverse perpendicular dielectric response profile $\varepsilon_\perp^{-1}(z)$ obtained from equilibrium fluctuations in neat water simulations as explained in a study related to this thesis [159] (Ref. [viii]) and used for the computation of φ_ε and φ_η is shown in fig. 4.2A. The lipid molecules only contribute significantly to the dielectric response about 1 nm around the interface (grey circles), where the charged headgroups are located. The dielectric response due to the water molecules (blue circles) increases away from the lipid bilayer and reaches the bulk value for the employed TIP3P water model of $\varepsilon_{\mathrm{sim}} = 94$ [160] about 1 nm away from the interface (as demonstrated in the inset in fig. 4.2A). Together, this leads to a non-monotonic increase of the total dielectric response (black circles) from the vacuum value of $\varepsilon_\perp = 1$ to the bulk water value $\varepsilon_\perp = 94$. This observation is in agreement with previous studies, which have shown that the dielectric response decreases at interfaces [150, 161]. The continuous black line shows the smoothed total inverse dielectric response profile $\varepsilon_\perp^{-1}(z)$ obtained by a sliding window average, which is used for the computation of the electrostatic potentials φ_ε and φ_η and the continuum model (see below).

Figure 4.2B shows the solution viscosity profile $\eta_\perp(z)$ obtained from the same simulations shown in fig. 4.1 by inversion eq. (4.9) (cf. eq. (4.19) in the Appendix). In the center of the water slab, the viscosity is difficult to estimate, since the solution velocity gradient and the total ionic charge density approach zero. Nevertheless, a drastic increase in the viscosity from the water slab towards the interface is apparent. A value at the interface of $\eta_\perp(z = 0) \approx 2$ mPas is observed, which is more than six times higher than the TIP3P bulk value of $\eta_{\mathrm{sim}} = 0.32$ mPas [162] (dashed blue line). Indeed, it has been shown previously that the solution viscosity increases at polar surfaces [163, 164], even as much as fivefold in the stagnant layer of charged interfaces [165]. The continuous black line in fig. 4.2B shows an exponential fit to the viscosity profile according to

$$\eta_\perp^{\mathrm{fit}}(z) = \overline{A}_\eta \cdot e^{-z/\overline{\lambda}_\eta} + \eta_{\mathrm{sim}}, \tag{4.14}$$

with values of $\overline{A}_\eta = 7\eta_{\mathrm{sim}}$ and $\overline{\lambda}_\eta = 0.39$ nm obtained from an average over all performed simulations with NaCl (see Appendix, Section 4.4.2 for details). The exponential fit of eq. (4.14) is used for the computation of the electrostatic potential φ_η according to eq. (4.10), as shown in fig. 4.1F and for the computation of the ζ-potential from the continuum model below.

For the direct comparison with experimental data, the ζ-potential is obtained from simulations based on the measured relative bulk solution velocity u_0 according to eq. (4.12), using the experimental values of the bulk dielectric constant $\varepsilon_{\mathrm{exp}}$ and viscosity η_{exp}, in analogy to the conversion of experimentally measured electroosmotic velocities into ζ-potentials. For the simulation data shown in fig. 4.1 we obtain $\zeta_{\mathrm{sim}} =$
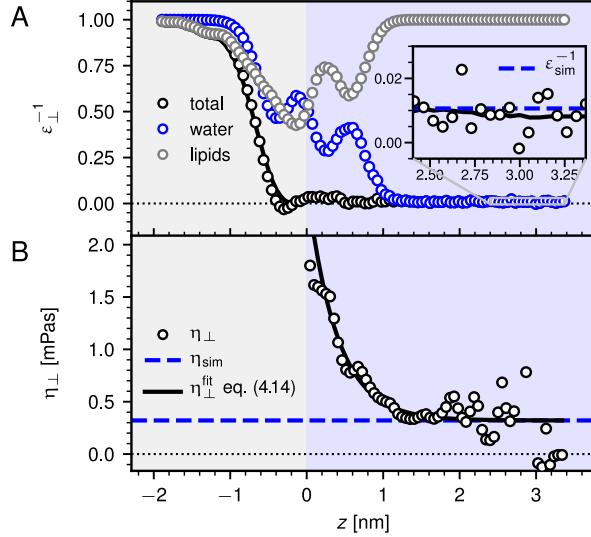
Figure 4.2: A: Profile of the inverse dielectric response $\varepsilon_\perp^{-1}(z)$. The lipids (grey circles) only contribute significantly in the interfacial region. Further away from the interface, the water contribution dominates (blue circles), reproducing the TIP3 bulk water value of $\varepsilon_{\text{sim}} = 94$ [160] (indicated as the blue broken line in the inset). The black continuous line represents the the smoothed version of the profile, which is obtained by a sliding window average and which is used for the computation of φ_ε, φ_η and the continuum model of eqs. (4.15). B: Profile of the solution viscosity $\eta_\perp(z)$ obtained from the same simulations as shown in fig. 4.1. A more than sixfold increase at the interface is observed compared to the TIP3P bulk value of $\eta_{\text{sim}} = 0.32$ mPas [162] (dashed blue line). The continuous black line is an exponential fit according to eq. (4.14), averaged over all simulations containing NaCl. The exponential fit is used in the computation of φ_η and the ζ-potential of the continuum model.

53.3 ± 10.7 mV, which indicates a positive net charge at the interface. Since the ζ-potential is defined by eq. (4.12) without taking interfacial dielectric and viscosity effects into account, it is not surprising that it does not match the computed electrostatic potential, $\zeta_{\text{sim}} \gg \varphi_\varepsilon(z = 0) = 24.7 \pm 1.2$ mV of fig. 4.1F, based on eq. (4.7). The assumptions of constant viscosity and dielectric response made in the derivation of the Helmholtz-Smoluchowski equation (4.12) are well known to underestimate the actual electrostatic potential [166, 167]. The fact that ζ_{sim} overestimates the electrostatic potential, however, is mainly due to the experimental value for the solution viscosity being much larger than the value in the simulations, $\eta_{\text{exp}} \gg \eta_{\text{sim}}$.

4.2.2 Continuum Model of the Lipid Interface

The obtained ζ- and electrostatic potentials are in agreement with previous simulation studies on the electrophoretic mobility of POPC bilayers in sodium chlorine solutions [149]. Experimental ζ-potential studies, however, report much lower values ranging from $\zeta_{\text{exp}} = -7$ mV to $\zeta_{\text{exp}} = +1$ mV, depending on the salt concentration [138]. In the following we rationalize this significant difference in magnitude and even sign of the ζ-potential obtained in simulations and experiments by the possible presence of minute amounts of anionic impurities. The same assumption has already resolved similar disagreements for ζ-potentials and surface tensions of hydrophobic interfaces [37, 146].

To this end, we model the lipid system in the presence of impurities using the modified Poisson-Boltzmann equation (PBE), which has been shown to accurately describe rigid [37, 146, 156] and soft interfaces [168]. The PBE is an equilibrium model, while the simulations discussed above have been performed out of equilibrium in the presence of an applied electric field, the strength of which, however, was chosen carefully in order to remain within the linear response regime (see Appendix, Section 4.4.1). In fact, no significant change compared to the equilibrium system is observed in the ion distributions and in the electrostatic potential (cf. also fig. 4.1F), legitimizing an equilibrium continuum model based on the PBE. Based on eq. (4.5) the electrostatic potential φ_ε is related to the charge density of free charges $\rho_f = \rho_{\text{ion}} + \rho_{\text{imp}}$, composed of the ionic density ρ_{ion} and a charge density due to the impurities ρ_{imp}, which are both assumed to be Boltzmann distributed (see Appendix, Section 4.4.3 for a detailed derivation)

$$
\begin{aligned}
\frac{d\varphi_\varepsilon}{dz}\frac{d\varepsilon_\perp^{-1}}{dz} - \varepsilon_\perp^{-1}(z)\frac{d^2\varphi_\varepsilon}{dz^2} &= \\
&= \varepsilon_0^{-1}\varepsilon_\perp^{-2}(z)\left[\rho_{\text{ion}}(z) + \rho_{\text{imp}}(z)\right], \\
\rho_{\text{ion}}(z) &= ec_{\text{salt}}\sum_{i=\pm}z_i\exp\left[-z_i\beta\varphi_\varepsilon(z) - \beta V_i(z)\right], \\
\rho_{\text{imp}}(z) &= ec_{\text{imp}}\sum_{j=\pm}z_j\exp\left[-z_j\beta\varphi_\varepsilon(z) - \beta W_j(z)\right].
\end{aligned}
\tag{4.15}
$$

Here e is the elementary charge, z_i and z_j are the respective valencies, $\beta = 1/k_{\text{B}}T$ is the inverse thermal energy and $\varepsilon_\perp^{-1}(z)$ is the inverse dielectric response. The bulk salt concentration is denoted as c_{salt} and the bulk impurity concentration as c_{imp}. The index in the sum of the ionic charge density extends over the cat- and anions, and for the impurities over the anionic surface-active species, as well as the positive counterion. The potentials of mean force (PMFs) V_i and W_j include all electrostatic and non-electrostatic interactions between the lipid-water interface and the ions or impurities at vanishing salt and impurity concentration [168]. Equation (4.15) is solved numerically for the electrostatic potential and the ion and impurity distributions.

The ionic PMFs have been determined from simulations by thermodynamic integration of the respective ions at infinite dilution at the lipid-water interface (for details see

Appendix, Section 4.4.4) and are shown for sodium and chlorine in fig. 4.3A. The PMFs reflect the observed shape of the electric double layer at the interface (cf. fig. 4.1C), demonstrating that the sodium ions penetrate further into the lipid phase compared to the chlorine ions. The anionic impurity PMF is modeled as a box profile

$$W_-(z) = \alpha\Theta(z_2 - z) + (\gamma - \alpha)\,\Theta(z_1 - z), \tag{4.16}$$

with values of $z_1 = 0.25$ nm, $z_2 = 0.75$ nm, $\gamma = 50\ k_\mathrm{B}T$ and $\alpha = -15.6\ k_\mathrm{B}T$. The adsorption strength of $\alpha = -15.6\ k_\mathrm{B}T$ and the width of the box $z_2 - z_1 = 0.5$ nm are chosen to match values extracted from the surface tension of sodium dodecyl-sulfate (SDS) [145], which is also why the PMF recorded for sodium is used for the neutralizing cation W_+. The potential barrier γ and the position of the box center at $z = 0.5$ nm are chosen so that the negative charge of the impurities is located slightly above the interface (cf. also fig. 4.3B), close to the choline groups of the zwitterionic lipid headgroup (cf. fig. 4.8A), which is reasonable when assuming incorporation of the impurities into the lipid bilayer.

Figure 4.3B shows a comparison between the ion distributions measured in simulations (continuous lines) and obtained from the continuum model of eqs. (4.15) (dashed lines), both at the same NaCl concentration of $c_\mathrm{salt} = 0.44$ M. The simulation data is from the same system as shown in fig. 4.1. Both, cationic and anionic distributions, match nicely in the absence of impurities, validating our modeling approach. Accounting for a finite but minute bulk concentration of impurities of $c_\mathrm{imp} = 156$ nM significantly changes the anion and especially the cation distribution at the interface (dotted lines). The exact value of c_imp has been chosen to match experimental ζ-potentials, as will be explained below. The electrostatic potential obtained from the continuum model in the absence of impurities is shown in fig. 4.3C as the dashed line. In the water slab it agrees for the most part with the potential obtained from simulations (continuous line). Deviations close to the interface and inside the lipid region presumably result from uncertainties in the ionic PMFs, as they are difficult to sample close to the lipid interface. The potential is significantly reduced in the presence of impurities (dotted line), and even becomes negative in the region where the surface-active impurities accumulate.

The ζ-potential is obtained from the continuum model by first computing an effective bulk flow velocity u_0^PBE by essentially inverting eq. (4.10) (for a detailed derivation see Appendix, Section 4.4.5). This bulk flow velocity is determined based on the electrostatic potential φ_ε obtained as the solution to the modified PB eqs. (4.15). In analogy to eq. (4.12) the ζ-potential is then computed according to [156]

$$\begin{aligned} \zeta_\mathrm{PBE} &= -\frac{\eta_\mathrm{exp}}{\varepsilon_\mathrm{exp}}\frac{u_0^\mathrm{PBE}}{\varepsilon_0 E_\|} \\ &= -\frac{\eta_\mathrm{exp}}{\varepsilon_\mathrm{exp}}\int_0^\infty \frac{1}{\varepsilon_\perp^{-1}(z)\eta_\perp^\mathrm{fit}(z)}\frac{d\varphi_\varepsilon}{dz}\ dz, \end{aligned} \tag{4.17}$$
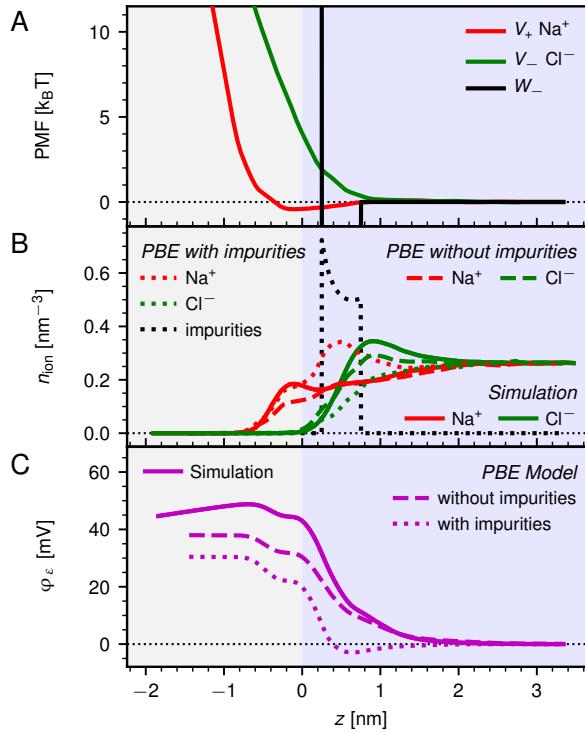
Figure 4.3: Continuum Model based on the modified Poisson-Boltzmann equation (PBE). A: Potentials of mean force (PMFs) for the sodium (red) and chlorine (green) ions at the lipid water interface. The PMF of the anionic impurities (black) is modeled as a box profile according to eq. (4.16). B: Comparison of number densities obtained from the continuum model of eqs. (4.15) and from simulations, in both cases for a NaCl concentration of $c_{salt} = 0.44$ M. The model results for the case without impurities (dashed lines) match the simulation results well (continuous lines). Especially the cation distribution changes significantly in the presence of impurities, shown as the dotted lines for a bulk impurity concentration of $c_{imp} = 156$ nM. C: Electrostatic potential from simulations and from the continuum model for both cases, with and without impurities. Model and simulation results agree for the most part of the water slab in the case of $c_{imp} = 0$ nM, while the potential is drastically reduced in the presence of impurities.

where $\eta_{\perp}^{fit}(z)$ denotes the averaged exponential fit to the viscosity profiles from simulations (as shown in fig. 4.2B) and $\varepsilon_{\perp}^{-1}(z)$ is the smoothed version of the inverse dielectric response profile (black continuous line in fig. 4.2A).

The ζ-potential obtained from the continuum model for the same salt concentration of $c_{salt} = 0.44$ M as shown in fig. 4.3 reduces drastically in the presence of impurities compared to the case without impurities, from $\zeta_{PBE} = 36.3$mV to $\zeta_{PBE} = 1.1$ mV,

which is now well within the range of experimentally measured values [138, 169]. This is in agreement with the fact, that the interfacial electrostatic potential decreases in the presence of impurities (cf. fig. 4.3C). The impurity surface excess $\Gamma_{\text{imp}} = \int_{-\infty}^{0} n_{\text{imp}}(z) \ dz + \int_{0}^{\infty} n_{\text{imp}}(z) - n_{\text{imp}}(D_w/2) \ dz = 0.27$ nm^{-2}, computed from the impurity number density n_{imp}, in the same way as in Chapter 3, translates to an average area per molecule of $A_{\text{imp}} = 3.70$ nm^2. The average area per POPC lipid molecule in the simulations shown in fig. 4.3 is obtained as $A_{\text{POPC}} = 0.64$ nm^2, in agreement with previous experimental studies [126] and with the findings of Chapter 3. This suggests that the surface concentration of the impurity molecules is roughly six times smaller than that of the PC-lipids in the bilayer. This is only a rough estimate, however, the actual impurity bulk concentration depends on the exact value of the adsorption strength and the specific shape of the impurity PMF. Additionally, the bulk concentration of impurities in experiments might be reduced by the partitioning of the surface-active species into the lipid vesicles, depending on the employed lipid concentration.

Using the PBE continuum model of eqs. (4.15), ζ-potentials can be computed for different salts at varying salt and impurity concentrations, according to eq. (4.17). The results of this analysis are presented in fig. 4.4A, in comparison to simulation results obtained in this work (full symbols) and experimental data from the literature (open symbols and crosses). Open symbols are experimental results on the ζ-potential of POPC vesicles from Klasczyk et al. [138] and crosses are measurements on DOPC vesicles from Maity et al. [169]. PBE model results in the absence of impurities (continuous lines) agree for the most part with results from simulations for KCl and NaCl salts. In MD simulations (full black circle) and in the continuum model the ζ-potential vanishes in neat water in agreement with the observation of a vanishing ionic charge density according to eq. (4.7) and vanishing bulk flow velocity according to eq. (4.11). We indeed observe no significant relative movement between lipid bilayer and water slab when applying an electric field in simulations without ions (see fig. 4.9 in the Appendix), which also rules out previous explanations for non-vanishing ζ-potentials in neat water due to polarization effects [140]. Only when incorporating nano-molar impurity concentrations in the PBE model (dashed lines), do the results agree with the experimental data. Especially the non-vanishing ζ-potential at $c_{\text{salt}} = 0$ M observed in experiments (open black circle) is only obtained in the continuum model when accounting for a minute but finite amount of negatively charged impurities. The exact value of the impurity concentration in the model is adjusted to match the corresponding experimental ζ-potential data best. A slightly reduced ζ-potential in the case of KCl compared to NaCl is observed in both, simulations and experiments, and reflects the reduced surface affinity for K$^+$ (cf. also fig. 4.8).

Figure 4.4B shows the impurity concentration c_{imp} necessary to explain the experimental data for different salt concentrations. An almost perfectly linear relationship between impurity and salt concentration is observed, which suggests that the impurities might be introduced through the addition of salt. The dashed lines show linear fits to the data, where each point is weighted by the corresponding uncertainty of the experimen-
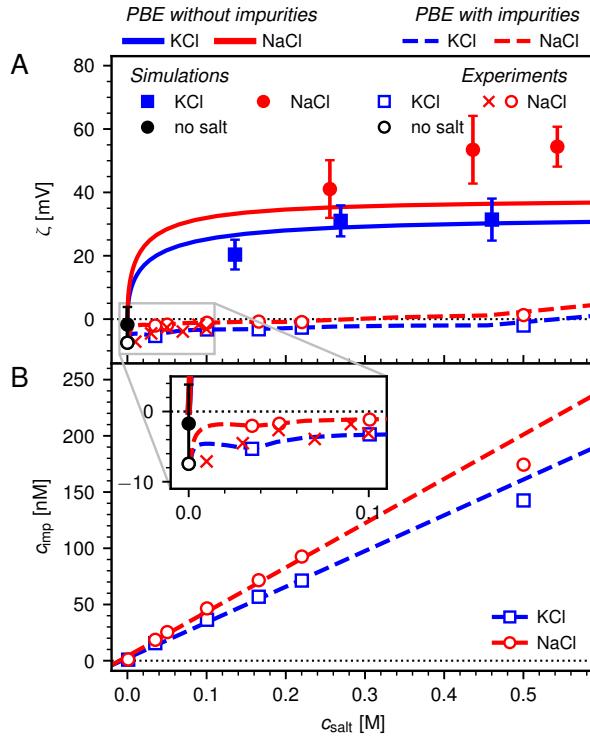
Figure 4.4: A: Comparison of experimental data for the ζ-potential of PC-lipid vesicles with simulations and modified PBE continuum model results. The continuum model in the absence of impurities (continuous lines) matches the simulation data (full symbols) for both chlorine salts. Only when accounting for a finite amount of negatively charged impurities does the continuum model (dashed lines) describe the experimental data (open symbols and crosses). The open symbols are data from Klasczyk et al. [138], while the crosses are measurements from Maity et al. [169]. B: The bulk impurity concentration c_{imp} necessary to describe the experimental data with the continuum model increases in a linear fashion with the bulk salt concentration c_{salt}. The dashed lines show a linear fit, where each point is weighted by the error of the respective experimental data point. For zero salt concentration we obtain an impurity concentration of $c_{imp} = 1$ nM.

tal ζ-potential measurement. The obtained values for the slope are $a_{NaCl} = 394$ nM/M and $a_{KCl} = 318$ nM/M, corresponding to impurity fractions in the salts in the order of 1 ppm, suggesting much higher purity values than the 99.9% usually reported for the salt samples by the suppliers. The non-vanishing impurity concentration at zero salt concentration of $c_{imp} = 1$ nM suggests that trace amounts of impurities may also be present in the purified lab water, which has been discussed previously in the literature [143, 144]. The fact that the obtained values for the impurity concentrations are

so similar for both salts, reflects the similar preparation of the samples, as the data is taken from the same study [138].

An analogous analysis for the salt $CaCl_2$ does not show a clear linear relation between impurity and salt concentration but nevertheless suggests the presence of impurities (see fig. 4.10 in the Appendix).

4.3 Conclusions

Using atomistic MD simulations in combination with electrostatic and hydrodynamic continuum modeling, we rationalize previously counterintuitive experimental data on the ζ-potential of PC-lipid vesicles by suggesting the presence of trace amounts of negatively charged impurities in lipids, lab water and added salt. In the first step of our multi-scale modeling, we obtain the ζ-potential of the PC-lipid interface from non-equilibrium MD simulations performed in the presence of an explicitly applied tangential electric field. In the second step we employ a continuum model based on the modified Poisson-Boltzmann and Helmholtz-Smoluchowski equations, for which the necessary input functions, namely the dielectric profile at the lipid-water interface, the ion-specific interactions between ions and the lipid-water interface and the interfacial viscosity profile, are all extracted from atomistic simulations. The validity and accuracy of the modified Poisson-Boltzmann and Helmholtz-Smoluchowski equations is checked by comparison with simulation results. Using the surface affinity of typical anionic surface-active species reported in the literature, we incorporate the presence of minute concentrations of impurities in our continuum model and are thus able to quantitatively explain experimental ζ-potential measurements. We find no evidence for previous alternative explanations for the value of ζ-potentials of PC-lipid vesicles in neat water, which were based on polarization effects of water or lipids [139, 140]. The possible presence of impurities presumably is thus the reason why, so far, simulation studies have not been able to reproduce experimental ζ-potentials [149, 170–172]. In agreement with our findings, previous studies suggested that impurities are present in the lab water used during preparations [143, 144]. The linear increase of the bulk impurity concentration with the salt concentration observed in our continuum model, indicates that impurities might be additionally introduced through the added salts. The presence of nano-molar concentrated impurities has recently helped to develop scenarios that explain a plethora of other surface phenomena such as the Jones-Ray effect [145], the stability of water films on silica surfaces [146] and the negative ζ-potential of hydrophobic surfaces [37]. We suggest that the investigation and understanding of ion-lipid interactions is aided by shedding light on the possibly crucial influence of impurities on the experimental measurement of ζ-potentials of the lipid-water interface.

4.4 Appendix to Chapter 4

4.4.1 Applying Electric Fields in Simulations

In order to determine ζ-potentials from simulations, an electric field $E_\parallel$ parallel to the lipid interface is applied. To independently determine the actual field strength in the water slab, we use the following relation between water polarization and electric field

$$E_\parallel^{\text{pol}} = \frac{m_\parallel}{(\varepsilon_{\text{bulk}} - 1)\varepsilon_0} = \frac{p_0 \cdot \cos\theta \cdot n_w}{(\varepsilon_{\text{bulk}} - 1)\varepsilon_0}. \tag{4.18}$$

Here ε_0 is the vacuum permittivity. The polarization density $m_\parallel$ is obtained from the TIP3P dipole moment $p_0 = 2.3$ D [173], the average of the cosine of the orientational angle of the water molecules in field direction in the center of the water slab $\cos\theta$ and the water number density in the center of the water slab n_w. For the dielectric constant, a value of $\varepsilon_{\text{bulk}} = 94$ is used, representing the TIP3P bulk value [160].

Figure 4.5A shows that the measured field strength $E_\parallel^{\text{pol}}$ in simulations containing $c_{\text{salt}} = 0.4$ M sodium chlorine, is for all performed simulations almost identical to the applied field strength $E_\parallel$. Deviations increase, however, for field strengths where $E_\parallel > 0.5$ V/nm. Additionally, the relation between field strength and bulk flow velocity is tested to make sure that the simulations are performed in the linear response regime (see fig. 4.5B). The relative bulk flow velocity $u_0 := u_{\text{sol}}(D_w/2) - u_{\text{lip}}$ is obtained from the solution velocity in the center of the water slab $u_{\text{sol}}(D_w/2)$ and the average velocity of the lipid bilayer u_{lip}. Figure 4.5B shows that u_0 increases in magnitude linearly with the field strength until $E_\parallel = 0.05$ V/nm, while it deviates from this linear relation (black continuous line) for larger field strengths. The number densities shown in fig. 4.5C also show that for fields larger than $E_\parallel = 0.05$ V/nm, the ionic distributions change significantly compared to the equilibrium distributions at vanishing electric field. This is why in all simulations used for analysis of the ζ-potential, a field strength of $E_\parallel = 0.05$ V/nm is employed.
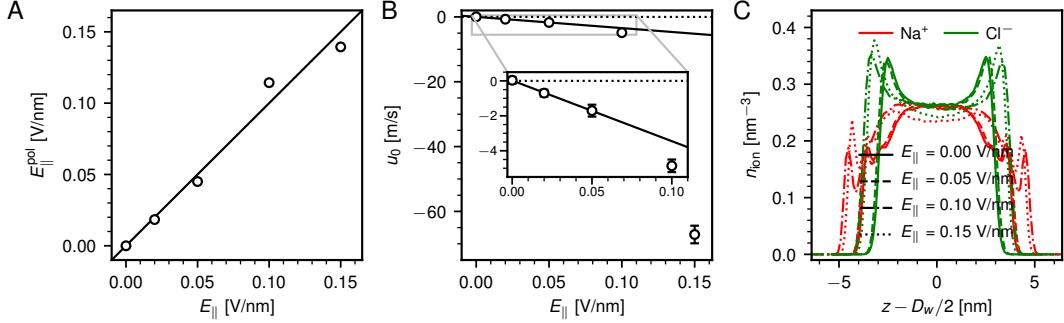
Figure 4.5: A: Relation between the nominally applied electric field $E_\parallel$ and the measured field strength in the water slab $E_\parallel^{\mathrm{pol}}$ according to eq. (4.18). The measured value is very close to the nominally applied value for the entire range of fields strengths. The continuous line represents the expected relation $E_\parallel^{\mathrm{pol}} = E_\parallel$. B: Average bulk flow velocity u_0 as a function of the strength of the applied field in the simulation $E_\parallel$. The continuous line shows a linear fit to the data for $E_\parallel \leq 0.5$ V/nm, where the system is in the linear response regime. C: Number density of sodium (red) and chlorine (green) ions in simulations with different applied field strengths indicated as different line styles.

4.4.2 Viscosity Profiles from Simulations

Atomistic molecular dynamics simulations of a POPC lipid bilayer in contact with different salt solutions at different salt concentrations with tangentially applied electric fields are performed, as described in Section 4.1. Viscosity profiles are estimated from these simulations by inverting eq. (4.9) from Section 4.2, leading to the following relation

$$\eta_\perp(z) = \frac{-E_\parallel \int_{D_w/2}^z \rho_{\text{ion}}(z')\ dz'}{du(z)/dz}, \tag{4.19}$$

where $E_\parallel$ is the tangential electric field, ρ_{ion} is the total ionic charge density, $D_w/2 \approx$ 3.5 nm is the center of the water slab and du/dz is the gradient of the solution velocity profile. According to eq. (4.19), an estimate for the viscosity is difficult to obtain in regions where $\int \rho_{\text{ion}}\ dz$ and du/dz vanish, i.e. in the center of the water slab. Below the Gibbs dividing plane at $z < 0$ the solution viscosity diverges, since the fluid velocity is constant in accord with the no-slip boundary condition. Figure 4.6 shows viscosity profiles obtained from simulations with $c_{\text{salt}} = 0.5$ M of NaCl (A), KCl (B) and CaCl$_2$ (B), respectively. The error bars for the viscosity profiles are estimated using Gauß error propagation based on the uncertainty of the integral over the ionic charge density and the derivative of the velocity profile, the errors of which are obtained by averaging over the two sides of the bilayer. In the center of the water slab the estimated viscosity is slightly lower than the TIP3P bulk viscosity of $\eta_{\text{sim}} = 0.32$ mPas [162] due to the aforementioned effect of vanishing total ionic charge density (cf. eq. (4.19)). For all simulations, a drastic increase is observed for the interfacial viscosity, which is in agreement with previous reports [163–165]. The continuous lines show error weighted exponential fits to the data points based on eq. (4.14) from Section 4.2.1. The z-range for these fits is chosen to be 0 nm $< z <$ 1.5 nm.
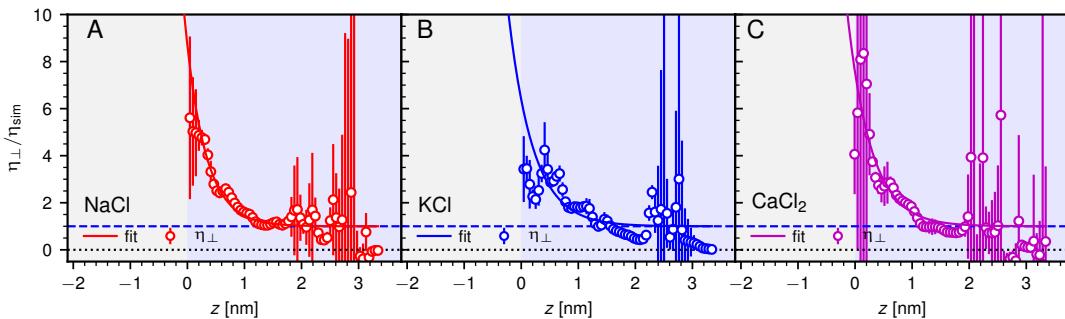
Figure 4.6: Results for the estimated solution viscosity profiles $\eta_\perp(z)$ according to eq. (4.19) obtained from simulations with the salts sodium chlorine (A), potassium chlorine (B) and calcium chlorine (C), all for a bulk salt concentration of $c_{\text{salt}} = 0.5$ M. Continuous lines represent exponential fits to the data based on eq. (4.14).

The obtained values for the fit parameters for each performed simulation are presented in fig. 4.7. The dashed lines show averaged values for a specific salt over all concentrations, which are the parameter values used for the continuum model of Section 4.2.2.
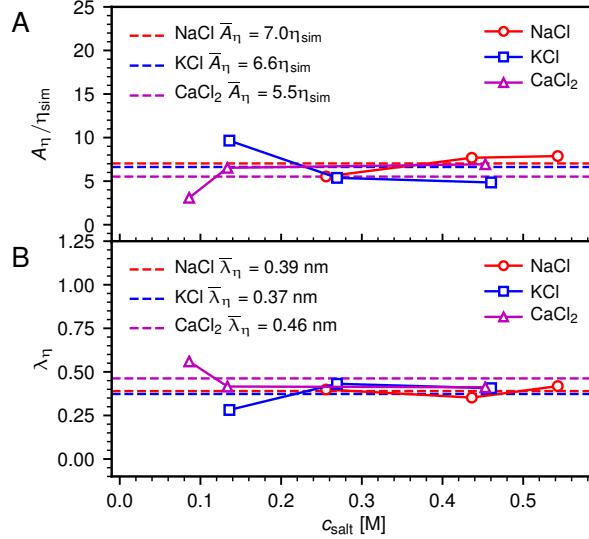
Figure 4.7: Obtained values for the parameters A_η (A) and λ_η (B) of the exponential fits to the viscosity data according to eq. (4.14) from Section 4.2.1. For each salt, the averaged values over all concentrations (dashed lines) are used for the continuum model of eqs. (4.15) from Section 4.2.2.

4.4.3 Derivation of the Modified Poisson Boltzmann Equation

Equation (4.5) from Section 4.1.2 approximately relates the profiles of the electric field $E_\perp(z)$ and the displacement field $D_\perp(z)$ as

$$\Delta E_\perp(z) = \varepsilon_0^{-1}\varepsilon_\perp^{-1}(z)D_\perp(z), \tag{4.20}$$

where $\varepsilon_\perp^{-1}(z)$ is the inverse local dielectric constant and ε_0 is the vacuum permittivity. Using the definition of the electrostatic potential, $\varphi_\varepsilon(z) := -\int_{D_w/2}^z \Delta E_\perp(z')dz'$, and taking the spatial derivate on both sides we obtain

$$
\begin{aligned}
-\frac{d^2\varphi_\varepsilon}{dz^2} &= \varepsilon_0^{-1}\frac{d}{dz}\left(\varepsilon_\perp^{-1}(z)D_\perp(z)\right) \\
&= \varepsilon_0^{-1}D_\perp(z)\frac{d\varepsilon_\perp^{-1}}{dz} + \varepsilon_0^{-1}\varepsilon_\perp^{-1}(z)\frac{dD_\perp}{dz}.
\end{aligned} \tag{4.21}
$$

We now employ eq. (4.2) from Section 4.1.2 for the divergence of the displacement field and multiply both sides with the inverse dielectric response, leading to

$$
\begin{aligned}
-\varepsilon_\perp^{-1}(z)\frac{d^2\varphi_\varepsilon}{dz^2} &= \varepsilon_0^{-1}\varepsilon_\perp^{-1}(z)D_\perp(z)\frac{d\varepsilon_\perp^{-1}}{dz} + \varepsilon_0^{-1}\varepsilon_\perp^{-2}(z)\rho_\mathrm{f}(z) \\
&= -\frac{d\varphi_\varepsilon}{dz}\frac{d\varepsilon_\perp^{-1}}{dz} + \varepsilon_0^{-1}\varepsilon_\perp^{-2}(z)\rho_\mathrm{f}(z),
\end{aligned} \tag{4.22}
$$

where we additionally re-substituted eq. (4.20) and where $\rho_f = \rho_\mathrm{ion} + \rho_\mathrm{imp}$ denotes all free charges in the model, including the ionic charge density ρ_ion and a charge density due to the impurities ρ_imp. Equation (4.22) then leads to the modified Poisson Boltzmann equation in the form of eq. (4.15) from Section 4.2.2, which is solved numerically using the method of successive over relaxation.

4.4.4 Recording Ion-Lipid Potentials of Mean Force

In order to determine the ion-membrane potential of mean force (PMF), the ion is introduced into the system by means of thermodynamic integration at different separations from the lipid bilayer. Using the multi-state Bennet acceptance ratio analysis [117], the van der Waals and Coulomb contributions to the PMFs are determined independently. For each component 11 λ-steps are employed with a simulation run time of 1 ns per λ-step. Results for a specific bilayer-ion separation are averaged over five lateral positions across the interface and over the two sides of the bilayer. This amounts to a total simulation run time of at least 220 ns per PMF data point. The ion-membrane distance is controlled by restraining the ions with a harmonic potential. The anion and cation are always simulated and introduced into the system together in order to guarantee charge neutrality. The counter ion position is, however, not varied in order to only observe the effect of the ion of interest. The contribution of the ion-ion interaction is estimated by computing the electrostatic potential of two point charges at a dielectric interface. For this, the full dielectric response profile is approximated by a two-region box profile. This interaction energy is then subtracted from the Coulomb part of the recorded PMFs, to determine only the ion-membrane interactions. The obtained PMFs with their individual contributions are shown in fig. 4.8.
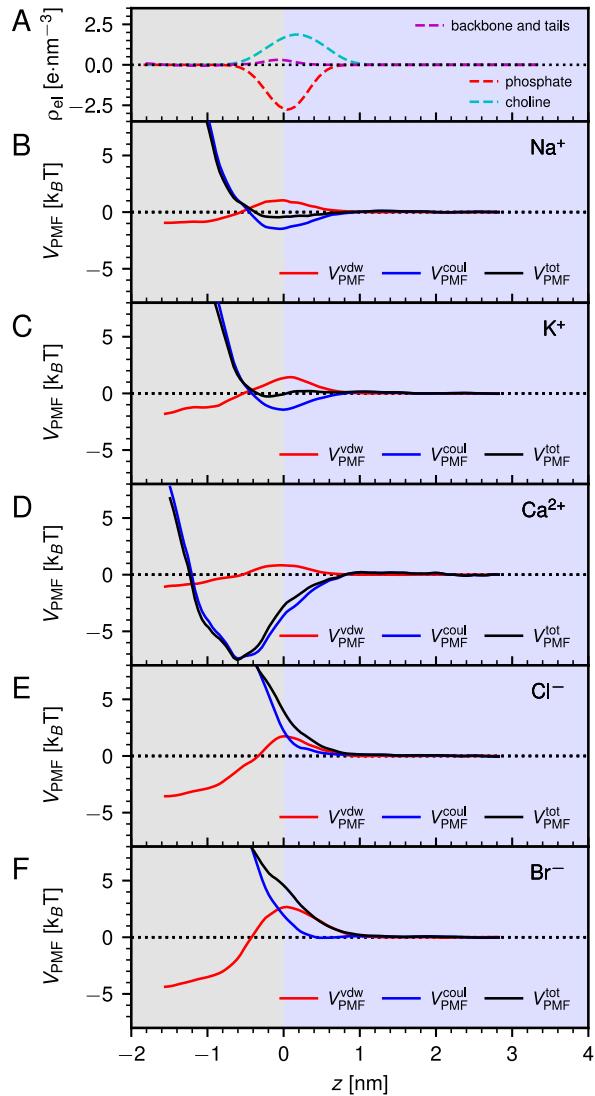
Figure 4.8: The charge density due to the different chemical groups of the lipid molecules (A) interacts with the ions and thereby determines the ionic potentials of mean force (PMF). The coulombic contribution $V_{\mathrm{PMF}}^{\mathrm{coul}}$ and the van der Waals part $V_{\mathrm{PMF}}^{\mathrm{vdw}}$ of the total PMF $V_{\mathrm{PMF}}^{\mathrm{tot}}$ are shown individually. The PMFs at the lipid-water interface for sodium (B) and potassium (C) display a slight attraction into the lipid domain, with a significantly stronger attraction for calcium (D), while the anionic PMFs for chlorine (E) and bromide (F) ions are purely repulsive. The cationic attraction to the interface is mediated by the coulombic contribution to the PMF $V_{\mathrm{PMF}}^{\mathrm{coul}}$ and, except for calcium, coincides with the position of the lipid headgroup's phosphate.

4.4.5 Computing Zeta Potentials from the Continuum Model

As explained in Section 4.2, the Stokes equation describes the flow at the lipid interface and reads

$$\frac{d}{dz}\left[\eta_\perp(z)\frac{du(z)}{dz}\right] = -E_\parallel \rho_{\text{ion}}(z), \tag{4.23}$$

where $\eta_\perp(z)$ is the fluid viscosity profile, $u(z)$ is the relative fluid velocity profile, $E_\parallel$ denotes the tangentially applied electric field and $\rho_{\text{ion}}(z)$ is the ionic charge density. Following the derivation in Section 4.2, integration of both sides of eq. (4.23) leads to

$$\eta_\perp(z)\frac{du(z)}{dz} = -E_\parallel \int_{D_w/2}^{z} \rho_{\text{ion}}(z')\ dz' = -E_\parallel D_\perp(z), \tag{4.24}$$

where $z = D_w/2$ denotes the center of the water slab and where eq. (4.2) from Section 4.1.2 is used. Additionally, the boundary condition of vanishing stress in the bulk solution $du(D_w/2)/dz = 0$ is used. Multiplication of both sides with the inverse dielectric response and substitution of eq. (4.5) from Section 4.1.2 leads to

$$\varepsilon_0^{-1}\varepsilon_\perp^{-1}(z)\eta_\perp(z)\frac{du(z)}{dz} = -E_\parallel \varepsilon_0^{-1}\varepsilon_\perp^{-1}(z)D_\perp(z)$$

$$\frac{1}{\varepsilon_0 E_\parallel}\frac{du(z)}{dz} = \frac{1}{\varepsilon_\perp^{-1}(z)\eta_\perp(z)}\frac{d\varphi_\varepsilon}{dz}. \tag{4.25}$$

Another integration on both sides, starting from the position of the shear plane $z = 0$ where the fluid velocity vanishes $u(z = 0) = 0$, leads to the following expression

$$\frac{u_0}{\varepsilon_0 E_\parallel} = \int_0^\infty \frac{1}{\varepsilon_\perp^{-1}(z)\eta_\perp(z)}\frac{d\varphi_\varepsilon}{dz}\ dz, \tag{4.26}$$

where $u_0 := u_{\text{sol}}(D_w/2) - u_{\text{lip}}$ denotes the solution velocity in the center of the water slab $u_{\text{sol}}(D_w/2)$ relative to the average velocity of the lipid bilayer u_{lip}. According to eq. (4.12) for the experimental ζ-potential from Section 4.2, the ζ-potential from the continuum model is obtained by multiplication of eq. (4.26) with the experimental viscosity η_{exp} and the inverse dielectric constant $\varepsilon_{\text{exp}}^{-1}$

$$\zeta_{\text{PBE}} = -\frac{\eta_{\text{exp}}u_0}{\varepsilon_{\text{exp}}\varepsilon_0 E_\parallel} = -\frac{\eta_{\text{exp}}}{\varepsilon_{\text{exp}}}\int_0^\infty \frac{1}{\varepsilon_\perp^{-1}(z)\eta_\perp(z)}\frac{d\varphi_\varepsilon}{dz}\ dz. \tag{4.27}$$
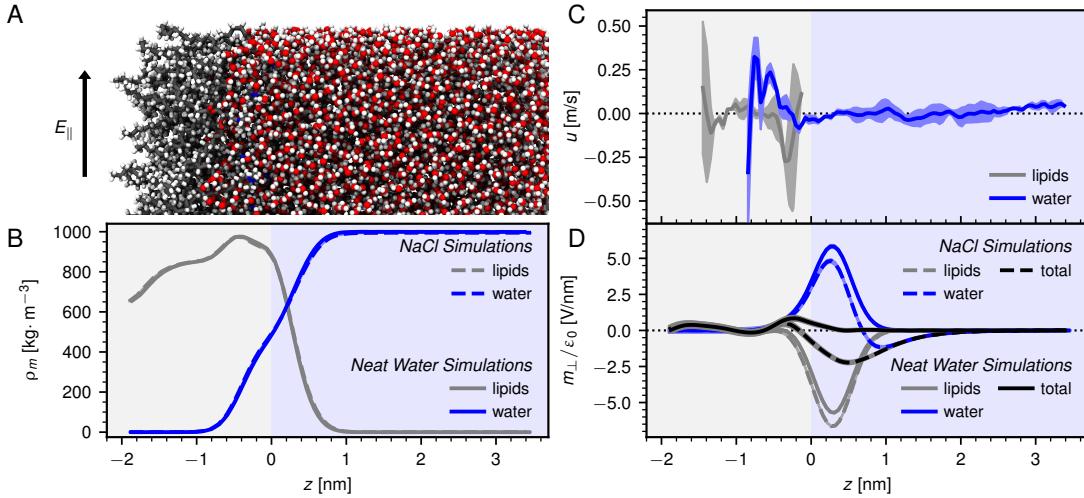
Figure 4.9: A: Screenshot from simulations of a POPC bilayer in neat water with an applied field of $E_\parallel = 0.05$ V/nm. B: Mass density ρ_m of the lipid (grey) and water molecules (blue). The density profiles from simulations in neat water (continuous lines) follow in their shape those obtained in simulations with $c_\mathrm{salt} = 0.44$ M NaCl (dashed lines) (cf. also fig. 4.1B). C: Average velocity across the interface. Both, the lipid (grey) and the water (blue) velocity profiles fluctuate around zero and no significant movement between the lipid bilayer and the water slab is observed. D: Polarization field due to the lipid charge density (grey) and the oriented water molecules (blue). The interfacial field due to the water is slightly larger in simulations with neat water (continuous lines) compared to simulations with NaCl (dashed lines) (cf. also fig. 4.1E), which suggests that the presence of ions perturbs the orientation of the water molecules at the interface. Also the lipid contribution is increased in simulations containing sodium chlorine, which leads to a significant net negative interfacial polarization field in NaCl simulations (dashed black line), which is not present in the neat water system (continuous black line). Shaded areas indicate errors estimated by averaging over both sides of the lipid bilayer.
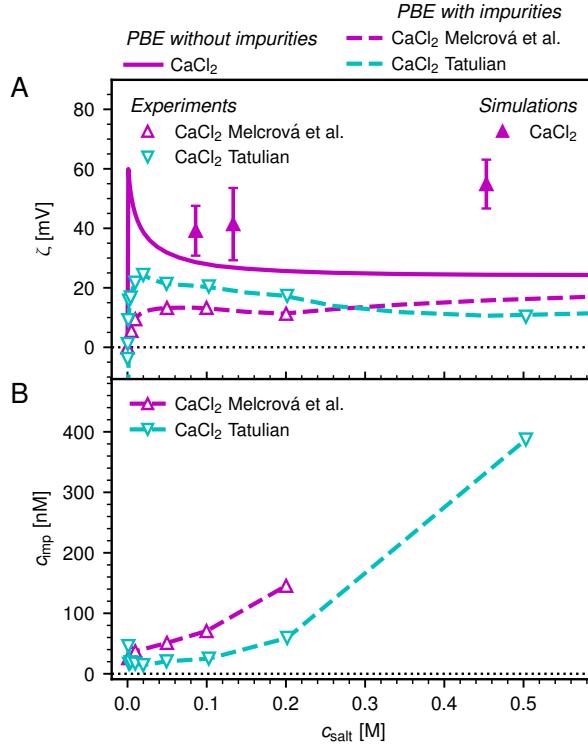
Figure 4.10: Calcium chlorine ζ-potential data. A: Comparison between results from simulations (full symbols) and continuum model results in the absence of impurities (continuous line). Deviations between simulations and the continuum model are likely due to the high adsorption strength of Ca^{2+} (see also fig. 4.11). The continuum model results accounting for impurities (dashed lines) match the experimental data (open symbols). The cyan open symbols are experimental results for DMPC vesicles from Tatulian [135] and the magenta open symbols are measurements for POPC vesicles performed by Melcrová et al. [174]. B: The impurity concentration in the continuum model needed in order to match the experimental data increases non-linearly with the added salt concentration. The apparent decrease in the impurity concentration at low salt concentration for the data of Tatulian is unclear and might be caused by different experimental procedures employed for the data points at low salt concentrations. Additionally, the lipids used for the experiments in this study were not obtained from a supplier, as is usually the case, but rather synthesized in house [135]. The purity of the lipid samples was reported as 99.3% [135].
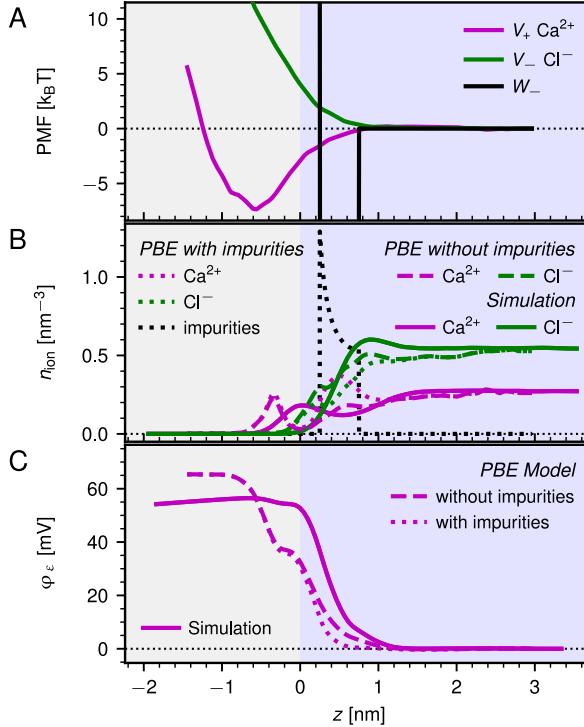
Figure 4.11: Calcium chlorine results from the continuum model. A: Potentials of mean force (PMFs) for the calcium (magenta) and chlorine (green) ions at the lipid water interface. The PMF of the anionic impurities (black) is modeled as a box profile according to eq. (4.16) from Section 4.2.2. The adsorption strength of calcium is significantly larger than that of the other cations (cf. fig. 4.8). B: Comparison of the number density profiles obtained from the continuum model and from simulations for a $CaCl_2$ bulk concentration of $c_{salt} = 0.5$ M. The deviations between the density profiles from simulations (continuous lines) and the continuum model in the absence of impurities (dashed lines) are larger for calcium compared to the case of sodium (cf. fig. 4.3B). Especially the position of the peak in the calcium distribution is shifted between the simulation and continuum model results. The reason for this disagreement might be due to modifications of the lipid-ion interactions in simulations at finite concentration of $CaCl_2$ compared to the PMFs obtained at infinite dilution, which presumably are caused by the strong attraction between lipid headgroup and calcium ions. As seen for the NaCl results in fig. 4.3, the cation distribution significantly changes in the presence of impurities (dotted lines). C: Electrostatic potentials from simulations (continuous line) and from the continuum model without impurities (dashed line) show the same trend as seen for the NaCl results in fig. 4.3. Only a small change in the potential is observed in the presence of impurities (dotted line).

Chapter 5

Summary and Conclusion

This thesis is concerned with biological interfaces and their interactions with various solutes. Penetration processes are a prime example of biological interfaces acting as permeation barriers which have to be overcome by diffusors and are of importance in medical scenarios such as drug delivery or host-infection by pathogens. The topics covered in this thesis broaden the understanding of barrier functions and other properties of biological interfaces, which are studied by means of theoretical and computational analyses. The first part considers hydrogels, being one of the most common biological interfaces, and their selective permeability for solutes, which is analyzed by employing the generalized diffusion equation. In the second part, the phosphatidylcholine (PC) lipid bilayer interface is investigated by means of atomistic molecular dynamics simulations in combination with electrostatic continuum modeling.

The analysis on the permeability of mucus-analogous hydrogels in Chapter 2 is based on a numerical inversion of the generalized diffusion equation. Using concentration profiles of fluorescently labeled tracer particles penetrating into hydrogels, free energy differences and diffusivity values are extracted. The introduced method constitutes an improvement over previous works [17, 18], as it does not require the conversion of the raw fluorescence intensity into physical concentration values but rather works on arbitrarily normalized data. This allows for the analysis of data that is subject to intensity fluctuations or drifts due to disturbances during experiments. The application of this method on measurements of fluorescently labeled dextran diffusors penetrating into PEG-based hydrogels reveals a *size-filtering* mechanism and displays scaling laws for the diffusion constants as a function of the dextran mass, which are in agreement with results from polymer theory. Based on the obtained values for the partition coefficients, a free-volume model, which also incorporates PEG and dextran flexibility, is developed. The model suggests that the pore distribution of the hydrogels is broad and that larger pores dominate the partitioning process, a feature that might be generally encountered for unordered biological hydrogels like mucus. This exemplary application of the method introduced in Chapter 2 shows the range of possible insights that can be gained by its use. This is why the application to actual layered biological systems, e.g. a layer of mucus on top of living mucus secreting cells, is especially intriguing for the future.

In Chapter 3 the PC-lipid interface in contact with solutions containing different small co-solutes, namely either TMAO, urea or sodium chlorine, is investigated. Based on atomistic molecular dynamics (MD) simulations, interaction pressures between lipid

bilayers at different hydration levels (i.e. different surface separations) are determined. For these simulations the water chemical potential in the water slab between the bilayers has to be carefully controlled. The characteristic exponential decay of the interaction pressure with surface separation, termed *hydration repulsion*, is recovered and an added repulsion compared to the neat-water system due to the addition of co-solutes is observed for all studied solutes. This effect can also be understood as leading to an increased level of hydration at the same interaction pressure. By retaining water at high osmotic pressures in this manner, compatible solutes hydrate the lipid bilayers in a way that is different from the usually reported substitution for water molecules at low hydration [96, 97]. The results of the simulations, which are corroborated by corresponding experimental measurements performed by our collaborators from the Sparr group (Lund University), provide data for in-detail analysis of the added repulsion. A simple thermodynamic model developed based on the simulation results, reveals that the added repulsion can be understood as an increased osmotic pressure afforded by the co-solutes. Furthermore, the solute-solute and solute-lipid interactions, which can also be determined from the simulation data, define the specific extent of this addition to the interaction pressure. The results of Chapter 3 thus show that, at least for large enough co-solute contents, the thermodynamics of the lipid system containing co-solutes can be modeled as a linear combination of the lipid neat-water system and the pure co-solute solution, when also accounting for the the lipid co-solute interactions. This way of modeling the interaction pressures explains the co-solute specific influences by relating them to their fundamental thermodynamic properties due to their chemical composition.

Chapter 4 considers the electrostatic properties of the PC-lipid interface and the way in which they govern the interactions with ions. Lipid bilayers are analyzed using a combination of large-scale atomistic MD simulations in equilibrium and out of equilibrium due to the application of an electric field parallel to the interface. From these simulations properties of the lipid interface like the dielectric response and the viscosity profiles are obtained. In agreement with studies on similar interfaces [150, 161, 163, 164], both, the dielectric response and the viscosity are significantly altered in the vicinity of the lipid bilayer. The simulations also allow for the determination of the potentials of mean force (PMFs) for various ions, which govern the ion-lipid interactions. The observed shape of the PMFs suggests that the PC-lipid interface displays an affinity for cations over anions, which, while still being a topic of debate in the physical chemistry community, has partly been confirmed by previous studies [121, 137]. Using the results from our simulations, an electrostatic continuum model based on the modified Poisson-Boltzmann and Smoluchowski equations is derived, allowing for the computation of ζ-potentials at varying salt concentration and subsequent comparison with experimental data. The negative ζ-potential of PC-lipid vesicles at vanishing salt concentration consistently observed in experimental studies is explained in this model by the incorporation of nanomolar amounts of negatively charged surface active impurities. In the neat-water experiments the impurities likely stem from contaminations of the lipid samples or are present in the lab water as suggested earlier [143, 144]. In agreement with

experimental observations, the ζ-potential steadily increases with the addition of salt, which can be understood by the aforementioned cationic adsorption to the interface. However, the presence of impurities is found to drastically reduce this increase and only when accounting for the presence of impurities does the continuum model match experimental results quantitatively. Additionally, the amount of impurities necessary to explain the experimental data increases with the salt concentration, which suggests that the contaminants are not only present in the lab water but are also introduced through the addition of salt. Chapter 4 thus shows that when assessing the ionic affinity to the PC-lipid interface by means of ζ-potential measurements, the possible presence of impurities has to be taken into account in order to obtain a realistic estimate of the underlying ion-lipid interactions.

In summary, the studies combined in this thesis introduce new computational frameworks for the analysis of biological interfaces and their interactions with solutes, being based on or validated by comparison with existing experimental approaches. The presented exemplary applications of these methods provide insights into the penetration barrier mechanism of hydrogels, as well as solute and ion adsorption to lipid interfaces, both of which are fundamental processes crucial for the functioning of these biological interfaces.

List of Publications

The present thesis is based on the following manuscripts, which have been published in peer-reviewed journals or books:

[i] A. Wolde-Kidan, A. Herrmann, A. Prause, M. Gradzielski, R. Haag, S. Block, and R. R. Netz, "Particle Diffusivity and Free-Energy Profiles in Hydrogels from Time-Resolved Penetration Data," *Biophysical Journal*, vol. 120, pp. 463-475, **2021**. [Online]. Available: https://doi.org/10.1016/j.bpj.2020.12.020

[ii] A. Wolde-Kidan, Q. D. Pham, A. Schlaich, P. Loche, E. Sparr, R. R. Netz, and E. Schneck, "Influence of polar co-solutes and salt on the hydration of lipid membranes," *Physical Chemistry Chemical Physics*, vol. 21, pp. 16989-17000, **2019**. [Online]. Available: https://doi.org/10.1039/C9CP01953G

[iii] A. Wolde-Kidan and R. R. Netz, "Interplay of Interfacial Viscosity, Specific-Ion, and Impurity Adsorption Determines Zeta Potentials of Phospholipid Membranes," *Langmuir*, vol. 37, pp. 8463–8473, **2021**. [Online]. Available: https://doi.org/10.1021/acs.langmuir.1c00868

The following publications are related to this thesis:

[iv] S. B. Lohan, S. Saeidpour, M. Colombo, S. Staufenbiel, M. Unbehauen, A. Wolde-Kidan, R. R. Netz, R. Bodmeier, R. Haag, C. Teutloff, R. Bittl, and M. C. Meinke, "Nanocrystals for Improved Drug Delivery of Dexamethasone in Skin Investigated by EPR Spectroscopy," *Pharmaceutics*, vol. 12, pp. 400, **2020**. [Online]. Available: https://doi.org/10.3390/pharmaceutics12050400

[v] Q. D. Pham, A. Wolde-Kidan, A. Gupta, A. Schlaich, E. Schneck, R. R. Netz, and E. Sparr, "Effects of Urea and TMAO on Lipid Self-Assembly under Osmotic Stress Conditions," *The Journal of Physical Chemistry B*, vol. 122, pp. 6471-6482, **2018**. [Online]. Available: https://doi.org/10.1021/acs.jpcb.8b02159

[vi] L. B. Dreier, A. Wolde-Kidan, D. J. Bonthuis, R. R. Netz, E. H. Backus, and M. Bonn, "Unraveling the Origin of the Apparent Charge of Zwitterionic Lipid Layers," *The Journal of Physical Chemistry Letters*, vol. 10, pp. 6355-6359, **2019**. [Online]. Available: https://doi.org/10.1021/acs.jpclett.9b02587

[vii] P. Loche, A. Wolde-Kidan, A. Schlaich, D. J. Bonthuis and R. R. Netz, "Comment on 'Hydrophobic Surface Enhances Electrostatic Interaction in Water'," *Physical Review Letters*, vol. 123, pp. 049601, **2019**. [Online]. Available: https://doi.org/10.1103/PhysRevLett.123.049601

[viii] P. Loche, C. Ayaz, A. Wolde-Kidan, A. Schlaich, and R. R. Netz, "Universal and Nonuniversal Aspects of Electrostatics in Aqueous Nanoconfinement," *The Journal of Physical Chemistry B*, vol. 124, pp. 4365–4371, **2020**. [Online]. Available: https://doi.org/10.1021/acs.jpcb.0c01967

[ix] M. Kanduč, A. Schlaich, B. Kowalik, A. Wolde-Kidan, R. R. Netz and E. Schneck, "Simulation Approaches to Short-Range Interactions between Lipid Membranes," *Biomembrane Simulations: Computational Studies of Biological Membranes*, Max L. Berkowitz, CRC Press, **2019**. ISBN: 1351060295

Bibliography

[1] C. Wagner, K. Wheeler, and K. Ribbeck, "Mucins and Their Role in Shaping the Functions of Mucus Barriers," *Annual Review of Cell and Developmental Biology*, vol. 34, pp. 189–215, **2018**. [Online]. Available: https://doi.org/10.1146/annurev-cellbio-100617-062818

[2] D. Wirthl, R. Pichler, M. Drack, G. Kettlguber, R. Moser, R. Gerstmayr, F. Hartmann, E. Bradt, R. Kaltseis, C. M. Siket, S. E. Schausberger, S. Hild, S. Bauer, and M. Kaltenbrunner, "Instant tough bonding of hydrogels for soft machines and electronics," *Science Advances*, vol. 3, p. e1700053, **2017**. [Online]. Available: https://doi.org/10.1126/sciadv.1700053

[3] A. Herrmann, L. Kaufmann, P. Dey, R. Haag, and U. Schedler, "Bioorthogonal in Situ Hydrogels Based on Polyether Polyols for New Biosensor Materials with High Sensitivity," *ACS Applied Materials & Interfaces*, vol. 10, pp. 11 382–11 390, **2018**. [Online]. Available: https://doi.org/10.1021/acsami.8b01860

[4] A. S. Hoffman, "Hydrogels for biomedical applications," *Advanced Drug Delivery Reviews*, vol. 64, pp. 18–23, **2012**. [Online]. Available: https://doi.org/10.1016/j.addr.2012.09.010

[5] J. Li and D. J. Mooney, "Designing hydrogels for controlled drug delivery," *Nature Reviews Materials*, vol. 1, p. 16071, **2016**. [Online]. Available: https://doi.org/10.1038/natrevmats.2016.71

[6] G. van Meer, D. R. Voelker, and G. W. Feigenson, "Membrane lipids: where they are and how they behave," *Nature Reviews Molecular Cell Biology*, vol. 9, pp. 112–124, **2008**. [Online]. Available: https://doi.org/10.1038/nrm2330

[7] R. Rand and V. Parsegian, "Hydration forces between phospholipid bilayers," *Biochimica et Biophysica Acta (BBA) - Reviews on Biomembranes*, vol. 988, pp. 351–376, **1989**. [Online]. Available: https://doi.org/10.1016/0304-4157(89) 90010-5

[8] V. A. Parsegian and T. Zemb, "Hydration forces: Observations, explanations, expectations, questions," *Current Opinion in Colloid and Interface Science*, vol. 16, pp. 618–624, **2011**. [Online]. Available: https://doi.org/10.1016/j.cocis. 2011.06.010

[9] N. Billings, A. Birjiniuk, T. S. Samad, P. S. Doyle, and K. Ribbeck, "Material properties of biofilms—a review of methods for understanding permeability and mechanics," *Reports on Progress in Physics*, vol. 78, p. 036601, **2015**. [Online]. Available: https://doi.org/10.1088/0034-4885/78/3/036601

[10] M. A. McGuckin, S. K. Lindén, P. Sutton, and T. H. Florin, "Mucin dynamics and enteric pathogens," *Nature Reviews Microbiology*, vol. 9, pp. 265–278, **2011**. [Online]. Available: https://doi.org/10.1038/nrmicro2538

[11] M. E. V. Johansson, H. Sjövall, and G. C. Hansson, "The gastrointestinal mucus system in health and disease," *Nature Reviews Gastroenterology & Hepatology*, vol. 10, pp. 352–361, **2013**. [Online]. Available: https://doi.org/10.1038/nrgastro.2013.35

[12] D. P. Wolf, L. Blasco, M. A. Khan, and M. Litt, "Human cervical mucus. IV. Viscoelasticity and sperm penetrability during the ovulatory menstrual cycle," *Fertility and Sterility*, vol. 30, pp. 163–169, **1978**. [Online]. Available: https://doi.org/10.1016/S0015-0282(16)43454-0

[13] O. Lieleg and K. Ribbeck, "Biological hydrogels as selective diffusion barriers," *Trends in Cell Biology*, vol. 21, pp. 543–551, **2011**. [Online]. Available: https://doi.org/10.1016/j.tcb.2011.06.002

[14] J. Witten and K. Ribbeck, "The particle in the spider's web: transport through biological hydrogels," *Nanoscale*, vol. 9, pp. 8080–8095, **2017**. [Online]. Available: https://doi.org/10.1039/C6NR09736G

[15] L. D. Li, T. Crouzier, A. Sarkar, L. Dunphy, J. Han, and K. Ribbeck, "Spatial Configuration and Composition of Charge Modulates Transport into a Mucin Hydrogel Barrier," *Biophysical Journal*, vol. 105, pp. 1357–1365, **2013**. [Online]. Available: https://doi.org/10.1016/j.bpj.2013.07.050

[16] M. Marczynski, B. T. Käsdorf, B. Altaner, A. Wenzler, U. Gerland, and O. Lieleg, "Transient binding promotes molecule penetration into mucin hydrogels by enhancing molecular partitioning," *Biomaterials Science*, vol. 6, pp. 3373–3387, **2018**. [Online]. Available: https://doi.org/10.1039/C8BM00664D

[17] R. Schulz, K. Yamamoto, A. Klossek, R. Flesch, S. Hönzke, F. Rancan, A. Vogt, U. Blume-Peytavi, S. Hedtrich, M. Schäfer-Korting, E. Rühl, and R. R. Netz, "Data-based modeling of drug penetration relates human skin barrier function to the interplay of diffusivity and free-energy profiles," *Proceedings of the National Academy of Sciences*, vol. 114, pp. 3631–3636, **2017**. [Online]. Available: https://doi.org/10.1073/pnas.1620636114

[18] R. Schulz, K. Yamamoto, A. Klossek, F. Rancan, A. Vogt, C. Schütte, E. Rühl, and R. R. Netz, "Modeling of Drug Diffusion Based on Concentration Profiles

in Healthy and Damaged Human Skin," *Biophysical Journal*, vol. 117, pp. 998–1008, **2019**. [Online]. Available: https://doi.org/10.1016/j.bpj.2019.07.027

[19] A. Wolde-Kidan, A. Herrmann, A. Prause, M. Gradzielski, R. Haag, S. Block, and R. R. Netz, "Particle Diffusivity and Free-Energy Profiles in Hydrogels from Time-Resolved Penetration Data," *Biophysical Journal*, vol. 120, pp. 463–475, **2021**. [Online]. Available: https://doi.org/10.1016/j.bpj.2020.12.020

[20] J.-B.-J. Fourier, *Théorie analytique de la chaleur*. F. Didot, 1822.

[21] A. Fick, "Ueber Diffusion," *Annalen der Physik und Chemie*, vol. 170, pp. 59–86, **1855**. [Online]. Available: https://doi.org/10.1002/andp.18551700105

[22] M. V. Smoluchowski, "Über Brownsche Molekularbewegung unter Einwirkung äußerer Kräfte und deren Zusammenhang mit der verallgemeinerten Diffusionsgleichung," *Annalen der Physik*, vol. 353, pp. 1103–1112, **1916**. [Online]. Available: https://www.physik.uni-augsburg.de/theo1/hanggi/MvS_Annalen_1916.pdf

[23] C. J. H. Porter, N. L. Trevaskis, and W. N. Charman, "Lipids and lipid-based formulations: optimizing the oral delivery of lipophilic drugs," *Nature Reviews Drug Discovery*, vol. 6, pp. 231–248, **2007**. [Online]. Available: https://doi.org/10.1038/nrd2197

[24] M. J. Janiak, D. M. Small, and G. G. Shipley, "Temperature and compositional dependence of the structure of hydrated dimyristoyl lecithin." *Journal of Biological Chemistry*, vol. 254, pp. 6068–6078, **1979**. [Online]. Available: https://doi.org/10.1016/S0021-9258(18)50520-2

[25] Q. D. Pham, A. Wolde-Kidan, A. Gupta, A. Schlaich, E. Schneck, R. R. Netz, and E. Sparr, "Effects of Urea and TMAO on Lipid Self-Assembly under Osmotic Stress Conditions," *The Journal of Physical Chemistry B*, vol. 122, pp. 6471–6482, **2018**. [Online]. Available: https://doi.org/10.1021/acs.jpcb.8b02159

[26] L. B. Dreier, A. Wolde-Kidan, D. J. Bonthuis, R. R. Netz, E. H. Backus, and M. Bonn, "Unraveling the Origin of the Apparent Charge of Zwitterionic Lipid Layers," *The Journal of Physical Chemistry Letters*, vol. 10, pp. 6355–6359, **2019**. [Online]. Available: https://doi.org/10.1021/acs.jpclett.9b02587

[27] E. K. Perttu, A. G. Kohli, and F. C. Szoka, "Inverse-Phosphocholine Lipids: A Remix of a Common Phospholipid," *Journal of the American Chemical Society*, vol. 134, pp. 4485–4488, **2012**. [Online]. Available: https://doi.org/10.1021/ja210989h

[28] V. A. Parsegian, N. Fuller, and R. P. Rand, "Measured work of deformation and repulsion of lecithin bilayers," *Proceedings of the National Academy of Sciences*, vol. 76, pp. 2750–2754, **1979**. [Online]. Available: https://doi.org/10.1073/pnas.76.6.2750

[29] J. Israelachvili and H. Wennerström, "Role of hydration and water structure in biological and colloidal interactions," *Nature*, vol. 379, p. 219, **1996**. [Online]. Available: https://doi.org/10.1038/379219a0

[30] B. Kowalik, A. Schlaich, M. Kanduč, E. Schneck, and R. R. Netz, "Hydration Repulsion Difference between Ordered and Disordered Membranes Due to Cancellation of Membrane–Membrane and Water-Mediated Interactions," *The Journal of Physical Chemistry Letters*, pp. 2869–2874, **2017**. [Online]. Available: https://doi.org/10.1021/acs.jpclett.7b00977

[31] D. M. Leneveu, R. P. Rand, and V. A. Parsegian, "Measurement of forces between lecithin bilayers," *Nature*, vol. 259, pp. 601–603, **1976**. [Online]. Available: https://doi.org/10.1038/259601a0

[32] R. Lipowsky, "The conformation of membranes," *Nature*, vol. 349, p. 475, **1991**. [Online]. Available: https://doi.org/10.1038/349475a0

[33] K. B. Storey and J. M. Storey, "Freeze tolerance in animals," *Physiological Reviews*, vol. 68, pp. 27–84, **1988**. [Online]. Available: https://doi.org/10.1152/physrev.1988.68.1.27

[34] E. Sparr and H. Wennerström, "Responding Phospholipid Membranes—Interplay between Hydration and Permeability," *Biophysical Journal*, vol. 81, pp. 1014–1028, **2001**. [Online]. Available: https://doi.org/10.1016/S0006-3495(01)75759-1

[35] P. M. Elias, "Epidermal barrier function: intercellular lamellar lipid structures, origin, composition and metabolism," *Journal of Controlled Release*, vol. 15, pp. 199–208, **1991**. [Online]. Available: https://doi.org/10.1016/0168-3659(91)90111-P

[36] R. L. Owen, J. K. Strasters, and E. D. Breyer, "Lipid vesicles in capillary electrophoretic techniques: Characterization of structural properties and associated membrane-molecule interactions," *Electrophoresis*, vol. 26, pp. 735–751, **2005**. [Online]. Available: https://doi.org/10.1002/elps.200410288

[37] Y. Uematsu, D. J. Bonthuis, and R. R. Netz, "Nanomolar Surface-Active Charged Impurities Account for the Zeta Potential of Hydrophobic Surfaces," *Langmuir*, vol. 36, pp. 3645–3658, **2020**. [Online]. Available: https://doi.org/10.1021/acs.langmuir.9b03795

[38] H.-C. Flemming and J. Wingender, "The biofilm matrix," *Nature Reviews Microbiology*, vol. 8, no. 9, pp. 623–633, **sep 2010**. [Online]. Available: http://www.nature.com/articles/nrmicro2415

[39] O. Lieleg, I. Vladescu, and K. Ribbeck, "Characterization of Particle Translocation through Mucin Hydrogels," *Biophysical Journal*, vol. 98, pp. 1782–1789, **2010**. [Online]. Available: https://doi.org/10.1016/j.bpj.2010.01.012

[40] D. J. Thornton and J. K. Sheehan, "From mucins to mucus: toward a more coherent understanding of this essential barrier." *Proceedings of the American Thoracic Society*, vol. 1, pp. 54–61, **2004**.

[41] M. A. Hollingsworth and B. J. Swanson, "Mucins in cancer: protection and control of the cell surface," *Nature Reviews Cancer*, vol. 4, pp. 45–60, **2004**. [Online]. Available: https://doi.org/10.1038/nrc1251

[42] M. E. V. Johansson, "Fast Renewal of the Distal Colonic Mucus Layers by the Surface Goblet Cells as Measured by In Vivo Labeling of Mucin Glycoproteins," *PLoS ONE*, vol. 7, p. e41009, **2012**. [Online]. Available: https://doi.org/10.1371/journal.pone.0041009

[43] X. Zhang, J. Hansing, R. R. Netz, and J. E. DeRouchey, "Particle Transport through Hydrogels Is Charge Asymmetric," *Biophysical Journal*, vol. 108, pp. 530–539, **2015**. [Online]. Available: https://doi.org/10.1016/j.bpj.2014.12.009

[44] J. Hansing, C. Ciemer, W. K. Kim, X. Zhang, J. E. DeRouchey, and R. R. Netz, "Nanoparticle filtering in charged hydrogels: Effects of particle size, charge asymmetry and salt concentration," *The European Physical Journal E*, vol. 39, p. 53, **2016**. [Online]. Available: https://doi.org/10.1140/epje/i2016-16053-2

[45] J. Hansing and R. R. Netz, "Particle Trapping Mechanisms Are Different in Spatially Ordered and Disordered Interacting Gels," *Biophysical Journal*, vol. 114, pp. 2653–2664, **2018**. [Online]. Available: https://doi.org/10.1016/j.bpj.2018.04.041

[46] J. Hansing, J. R. Duke, E. B. Fryman, J. E. DeRouchey, and R. R. Netz, "Particle Diffusion in Polymeric Hydrogels with Mixed Attractive and Repulsive Interactions," *Nano Letters*, vol. 18, pp. 5248–5256, **2018**. [Online]. Available: https://doi.org/10.1021/acs.nanolett.8b02218

[47] M. Dawson, E. Krauland, D. Wirtz, and J. Hanes, "Transport of Polymeric Nanoparticle Gene Carriers in Gastric Mucus," *Biotechnology Progress*, vol. 20, pp. 851–857, **2004**. [Online]. Available: https://doi.org/10.1021/bp0342553

[48] J. N. Wilking, V. Zaburdaev, M. De Volder, R. Losick, M. P. Brenner, and D. A. Weitz, "Liquid transport facilitated by channels in Bacillus subtilis biofilms," *Proceedings of the National Academy of Sciences*, vol. 110, pp. 848–852, **2013**. [Online]. Available: https://doi.org/10.1073/pnas.1216376110

[49] J. R. Lawrence, G. M. Wolfaardt, and D. R. Korber, "Determination of Diffusion Coefficients in Biofilms by Confocal Laser Microscopy," *Applied and Environmental Microbiology*, vol. 60, pp. 1166–1173, **1994**. [Online]. Available: https://aem.asm.org/content/60/4/1166

[50] A. P. Sassi, A. J. Shaw, Sang Min Han, H. W. Blanch, and J. M. Prausnitz, "Partitioning of proteins and small biomolecules in temperature- and pH-sensitive hydrogels," *Polymer*, vol. 37, pp. 2151–2164, **1996**. [Online]. Available: https://doi.org/10.1016/0032-3861(96)85860-5

[51] A. Herrmann, S. Rödiger, C. Schmidt, P. Schierack, and U. Schedler, "Spatial Separation of Microbeads into Detection Levels by a Bioorthogonal Porous Hydrogel for Size-Selective Analysis and Increased Multiplexity," *Analytical Chemistry*, vol. 91, pp. 8484–8491, **2019**. [Online]. Available: https://doi.org/10.1021/acs.analchem.9b01586

[52] M. Furter, M. E. Sellin, G. C. Hansson, and W.-D. Hardt, "Mucus Architecture and Near-Surface Swimming Affect Distinct Salmonella Typhimurium Infection Patterns along the Murine Intestinal Tract," *Cell Reports*, vol. 27, pp. 2665–2678.e3, **2019**. [Online]. Available: https://doi.org/10.1016/j.celrep.2019.04.106

[53] S. B. Lohan, S. Saeidpour, M. Colombo, S. Staufenbiel, M. Unbehauen, A. Wolde-Kidan, R. R. Netz, R. Bodmeier, R. Haag, C. Teutloff, R. Bittl, and M. C. Meinke, "Nanocrystals for Improved Drug Delivery of Dexamethasone in Skin Investigated by EPR Spectroscopy," *Pharmaceutics*, vol. 12, p. 400, **2020**. [Online]. Available: https://doi.org/10.3390/pharmaceutics12050400

[54] P. Dey, T. Schneider, L. Chiappisi, M. Gradzielski, G. Schulze-Tanzil, and R. Haag, "Mimicking of Chondrocyte Microenvironment Using In Situ Forming Dendritic Polyglycerol Sulfate-Based Synthetic Polyanionic Hydrogels," *Macromolecular Bioscience*, vol. 16, pp. 580–590, **2016**. [Online]. Available: https://doi.org/10.1002/mabi.201500377

[55] M. A. Branch, T. F. Coleman, and Y. Li, "A Subspace, Interior, and Conjugate Gradient Method for Large-Scale Bound-Constrained Minimization Problems," *SIAM Journal on Scientific Computing*, vol. 21, pp. 1–23, **1999**. [Online]. Available: https://doi.org/10.1137/S1064827595289108

[56] H. Risken and T. Frank, *The Fokker-Planck Equation: Methods of Solution and Applications*, ser. Springer Series in Synergetics. Springer Berlin Heidelberg, 2012.

[57] P. Gribbon and T. E. Hardingham, "Macromolecular Diffusion of Biological Polymers Measured by Confocal Fluorescence Recovery after Photobleaching," *Biophysical Journal*, vol. 75, pp. 1032–1039, **1998**. [Online]. Available: https://doi.org/10.1016/S0006-3495(98)77592-7

[58] Y. Cheng, R. K. Prud'homme, and J. L. Thomas, "Diffusion of Mesoscopic Probes in Aqueous Polymer Solutions Measured by Fluorescence Recovery after Photobleaching," *Macromolecules*, vol. 35, pp. 8111–8121, **2002**. [Online]. Available: https://doi.org/10.1021/ma0107758

[59] Z. Bu and P. S. Russo, "Diffusion of Dextran in Aqueous (Hydrox-ypropyl)cellulose," *Macromolecules*, vol. 27, pp. 1187–1194, **1994**. [Online]. Available: https://doi.org/10.1021/ma00083a017

[60] M. Rubinstein and R. H. Colby, *Polymer Physics.* OUP Oxford, 2003.

[61] R. R. Netz and D. Andelman, "Neutral and charged polymers at interfaces," *Physics Reports*, vol. 380, pp. 1–95, **2003**. [Online]. Available: https://doi.org/10.1016/S0370-1573(03)00118-2

[62] J. Hansing and R. R. Netz, "Hydrodynamic Effects on Particle Diffusion in Polymeric Hydrogels with Steric and Electrostatic Particle–Gel Interactions," *Macromolecules*, vol. 51, pp. 7608–7620, **2018**. [Online]. Available: https://doi.org/10.1021/acs.macromol.8b01494

[63] E. Axpe, D. Chan, G. S. Offeddu, Y. Chang, D. Merida, H. L. Hernandez, and E. A. Appel, "A Multiscale Model for Solute Diffusion in Hydrogels," *Macromolecules*, vol. 52, pp. 6889–6897, **2019**. [Online]. Available: https://doi.org/10.1021/acs.macromol.9b00753

[64] Y.-Y. Wang, S. K. Lai, J. S. Suk, A. Pace, R. Cone, and J. Hanes, "Addressing the PEG Mucoadhesivity Paradox to Engineer Nanoparticles that "Slip" through the Human Mucus Barrier," *Angewandte Chemie International Edition*, vol. 47, pp. 9726–9729, **2008**. [Online]. Available: https://doi.org/10.1002/anie.200803526

[65] M. Kanduč and R. R. Netz, "From hydration repulsion to dry adhesion between asymmetric hydrophilic and hydrophobic surfaces," *Proceedings of the National Academy of Sciences*, vol. 112, pp. 12 338–12 343, **2015**. [Online]. Available: https://doi.org/10.1073/pnas.1504919112

[66] E. Schneck, F. Sedlmeier, and R. R. Netz, "Hydration repulsion between biomembranes results from an interplay of dehydration and depolarization," *Proceedings of the National Academy of Sciences*, vol. 109, pp. 14 405–14 409, **2012**. [Online]. Available: https://doi.org/10.1073/pnas.1205811109

[67] M. Moore, "Symmetrical Intersections of Right Circular Cylinders," *The Mathematical Gazette*, vol. 58, p. 181, **1974**. [Online]. Available: https://doi.org/10.2307/3615957

[68] S. Liese, M. Gensler, S. Krysiak, R. Schwarzl, A. Achazi, B. Paulus, T. Hugel, J. P. Rabe, and R. R. Netz, "Hydration Effects Turn a Highly Stretched Polymer from an Entropic into an Energetic Spring," *ACS Nano*, vol. 11, pp. 702–712, **2017**. [Online]. Available: https://doi.org/10.1021/acsnano.6b07071

[69] J. C. Giddings, E. Kucera, C. P. Russell, and M. N. Myers, "Statistical theory for the equilibrium distribution of rigid molecules in inert porous networks.

Exclusion chromatography," *The Journal of Physical Chemistry*, vol. 72, pp. 4397–4408, **1968**. [Online]. Available: https://doi.org/10.1021/j100859a008

[70] J. M. Diamond and Y. Katz, "Interpretation of nonelectrolyte partition coefficients between dimyristoyl lecithin and water," *The Journal of Membrane Biology*, vol. 17, pp. 121–154, **1974**. [Online]. Available: https://doi.org/10.1007/BF01870176

[71] H. Zhou and S. B. Chen, "Brownian dynamics simulation of tracer diffusion in a cross-linked network," *Physical Review E*, vol. 79, p. 021801, **2009**. [Online]. Available: https://doi.org/10.1103/PhysRevE.79.021801

[72] A. Godec, M. Bauer, and R. Metzler, "Collective dynamics effect transient subdiffusion of inert tracers in flexible gel networks," *New Journal of Physics*, vol. 16, p. 092002, **2014**. [Online]. Available: https://doi.org/10.1088/1367-2630/16/9/092002

[73] P. Kumar, L. Theeyancheri, S. Chaki, and R. Chakrabarti, "Transport of probe particles in a polymer network: effects of probe size, network rigidity and probe–polymer interaction," *Soft Matter*, vol. 15, pp. 8992–9002, **2019**. [Online]. Available: https://doi.org/10.1039/C9SM01822K

[74] H. F. M. Mohamed, Y. Kobayashi, C. S. Kuroda, and A. Ohira, "Effects of Ion Exchange on the Free Volume and Oxygen Permeation in Nafion for Fuel Cells," *The Journal of Physical Chemistry B*, vol. 113, pp. 2247–2252, **2009**. [Online]. Available: https://doi.org/10.1021/jp808960w

[75] N. Jordan, J. Newton, J. Pearson, and A. Allen, "A novel method for the visualization of the in situ mucus layer in rat and man," *Clinical Science*, vol. 95, pp. 97–106, **1998**. [Online]. Available: https://doi.org/10.1042/cs0950097

[76] C. Atuma, V. Strugala, A. Allen, and L. Holm, "The adherent gastrointestinal mucus gel layer: thickness and physical state in vivo," *American Journal of Physiology-Gastrointestinal and Liver Physiology*, vol. 280, pp. G922–G929, **2001**. [Online]. Available: https://doi.org/10.1152/ajpgi.2001.280.5.G922

[77] L. Huang and K. Nishinari, "Interaction between poly(ethylene glycol) and water as studied by differential scanning calorimetry," *Journal of Polymer Science, Part B: Polymer Physics*, vol. 39, pp. 496–506, **2001**. [Online]. Available: https://doi.org/10.1002/1099-0488(20010301)39:5%3C496::AID-POLB1023%3E3.0.CO;2-H

[78] T. Shikata, R. Takahashi, and A. Sakamoto, "Hydration of Poly(ethylene oxide)s in Aqueous Solution As Studied by Dielectric Relaxation Measurements," *The Journal of Physical Chemistry B*, vol. 110, pp. 8941–8945, **2006**. [Online]. Available: https://doi.org/10.1021/jp060356i

[79] U. Kaatze, O. Gottmann, R. Podbielski, R. Pottel, and U. Terveer, "Dielectric relaxation in aqueous solutions of some oxygen-containing linear hydrocarbon polymers," *The Journal of Physical Chemistry*, vol. 82, pp. 112–120, **1978**. [Online]. Available: https://doi.org/10.1021/j100490a025

[80] T. W. N. Bieze, A. C. Barnes, C. J. M. Huige, J. E. Enderby, and J. C. Leyte, "Distribution of Water around Poly(ethylene oxide): A Neutron Diffraction Study," *The Journal of Physical Chemistry*, vol. 98, pp. 6568–6576, **1994**. [Online]. Available: https://doi.org/10.1021/j100077a024

[81] W. Żwirbla, A. Sikorska, and B. B. Linde, "Ultrasonic investigations of water mixtures with polyethylene glycols 200, 400 and ethylene glycol," *Journal of Molecular Structure*, vol. 743, pp. 49–52, **2005**. [Online]. Available: https://doi.org/10.1016/j.molstruc.2005.02.019

[82] C. Branca, S. Magazù, G. Maisano, F. Migliardo, P. Migliardo, and G. Romeo, "Hydration Study of PEG/Water Mixtures by Quasi Elastic Light Scattering, Acoustic and Rheological Measurements," *The Journal of Physical Chemistry B*, vol. 106, pp. 10 272–10 276, **2002**. [Online]. Available: https://doi.org/10.1021/jp014345v

[83] J. Ulminus, H. Wennerstrom, G. Lindblom, and G. Arvidson, "Deuteron nuclear magnetic resonance studies of phase equilibriums in a lecithin-water system," *Biochemistry*, vol. 16, pp. 5742–5745, **1977**. [Online]. Available: https://doi.org/10.1021/bi00645a014

[84] B. Kowalik, T. Schubert, H. Wada, M. Tanaka, R. R. Netz, and E. Schneck, "Combination of MD Simulations with Two-State Kinetic Rate Modeling Elucidates the Chain Melting Transition of Phospholipid Bilayers for Different Hydration Levels," *The Journal of Physical Chemistry B*, vol. 119, pp. 14 157–14 167, **2015**. [Online]. Available: https://doi.org/10.1021/acs.jpcb.5b05501

[85] P. H. Yancey, "Organic osmolytes as compatible, metabolic and counteracting cytoprotectants in high osmolarity and other stresses," *Journal of Experimental Biology*, vol. 208, pp. 2819–2830, **2005**. [Online]. Available: https://doi.org/10.1242/jeb.01730

[86] G. O. Kirst, "Salinity Tolerance of Eukaryotic Marine Algae," *Annual Review of Plant Physiology and Plant Molecular Biology*, vol. 41, pp. 21–53, **1990**. [Online]. Available: https://doi.org/10.1146/annurev.pp.41.060190.000321

[87] I. J. Vereyken, V. Chupin, A. Islamov, A. Kuklin, D. K. Hincha, and B. de Kruijff, "The Effect of Fructan on Membrane Lipid Organization and Dynamics in the Dry State," *Biophysical Journal*, vol. 85, pp. 3058–3065, **2003**. [Online]. Available: https://doi.org/10.1016/S0006-3495(03)75104-2

[88] K. N. Barton, M. M. Buhr, and J. S. Ballantyne, "Effects of urea and trimethylamine N-oxide on fluidity of liposomes and membranes of an elasmobranch," *American Journal of Physiology-Regulatory, Integrative and Comparative Physiology*, vol. 276, pp. R397–R406, **1999**. [Online]. Available: https://doi.org/10.1152/ajpregu.1999.276.2.R397

[89] U.-B. Ramløy, "Aspects of natural cold tolerance in ectothermic animals," *Human Reproduction*, vol. 15, pp. 26–46, **2000**. [Online]. Available: https://doi.org/10.1093/humrep/15.suppl_5.26

[90] M. Hara and A. Verkman, "Glycerol replacement corrects defective skin hydration, elasticity, and barrier function in aquaporin-3-deficient mice," *Proceedings of the National Academy of Sciences*, vol. 100, pp. 7360–7365, **2003**. [Online]. Available: https://doi.org/10.1073/pnas.1230416100

[91] A. V. Rawlings, I. R. Scott, C. R. Harding, and P. A. Bowser, "Stratum Corneum Moisturization at the Molecular Level," *Journal of Investigative Dermatology*, vol. 103, pp. 731–740, **1994**. [Online]. Available: https://www.sciencedirect.com/science/article/pii/S0022202X94904472

[92] S. Björklund, J. M. Andersson, Q. D. Pham, A. Nowacka, D. Topgaard, and E. Sparr, "Stratum corneum molecular mobility in the presence of natural moisturizers," *Soft Matter*, vol. 10, pp. 4535–4546, **2014**. [Online]. Available: https://doi.org/10.1039/C4SM00137K

[93] C. Katagiri, J. Sato, J. Nomura, and M. Denda, "Changes in environmental humidity affect the water-holding property of the stratum corneum and its free amino acid content, and the expression of filaggrin in the epidermis of hairless mice," *Journal of Dermatological Science*, vol. 31, pp. 29–35, **2003**. [Online]. Available: https://doi.org/10.1016/S0923-1811(02)00137-8

[94] S. Kezic, G. O'Regan, N. Yau, A. Sandilands, H. Chen, L. Campbell, K. Kroboth, R. Watson, M. Rowland, W. Irwin McLean *et al.*, "Levels of filaggrin degradation products are influenced by both filaggrin genotype and atopic dermatitis severity," *Allergy*, vol. 66, pp. 934–940, **2011**. [Online]. Available: https://doi.org/10.1111/j.1398-9995.2010.02540.x

[95] J. H. Crowe, L. M. Crowe, and D. Chapman, "Preservation of Membranes in Anhydrobiotic Organisms: The Role of Trehalose," *Science*, vol. 223, pp. 701–703, **1984**. [Online]. Available: https://doi.org/10.1126/science.223.4637.701

[96] F. O. Costa-Balogh, H. Wennerström, L. Wadsö, and E. Sparr, "How Small Polar Molecules Protect Membrane Systems against Osmotic Stress: The Urea-Water- Phospholipid System," *The Journal of Physical Chemistry B*, vol. 110, pp. 23 845–23 852, **2006**. [Online]. Available: https://doi.org/10.1021/jp0632440

[97] A. Nowacka, S. Douezan, L. Wadsö, D. Topgaard, and E. Sparr, "Small polar molecules like glycerol and urea can preserve the fluidity of lipid bilayers under dry conditions," *Soft Matter*, vol. 8, pp. 1482–1491, **2012**. [Online]. Available: https://doi.org/10.1039/C1SM06273E

[98] S. Sukenik, S. Dunsky, A. Barnoy, I. Shumilin, and D. Harries, "TMAO mediates effective attraction between lipid membranes by partitioning unevenly between bulk and lipid domains," *Physical Chemistry Chemical Physics*, vol. 19, pp. 29 862–29 871, **2017**. [Online]. Available: https://doi.org/10.1039/C7CP04603K

[99] E. Schneck, F. Sedlmeier, and R. R. Netz, "Hydration repulsion between biomembranes results from an interplay of dehydration and depolarization," *Proceedings of the National Academy of Sciences*, vol. 109, pp. 14 405–14 409, **2012**. [Online]. Available: https://doi.org/10.1073/pnas.1205811109

[100] M. Kanduč, A. Schlaich, A. H. de Vries, J. Jouhet, E. Maréchal, B. Demé, R. R. Netz, and E. Schneck, "Tight cohesion between glycolipid membranes results from balanced water–headgroup interactions," *Nature Communications*, vol. 8, p. 14899, **2017**. [Online]. Available: https://doi.org/10.1038/ncomms14899

[101] N. Markova, E. Sparr, L. Wadsö, and H. Wennerström, "A Calorimetric Study of Phospholipid Hydration. Simultaneous Monitoring of Enthalpy and Free Energy," *The Journal of Physical Chemistry B*, vol. 104, pp. 8053–8060, **2000**. [Online]. Available: https://doi.org/10.1021/jp001020q

[102] R. A. Robinson and R. H. Stokes, *Electrolyte Solutions: Second Revised Edition*, ser. Dover Books on Chemistry Series.   Dover Publications, Incorporated, 1959.

[103] M. J. Abraham, T. Murtola, R. Schulz, S. Páll, J. C. Smith, B. Hess, and E. Lindahl, "Gromacs: High performance molecular simulations through multi-level parallelism from laptops to supercomputers," *SoftwareX*, vol. 1-2, pp. 19–25, **2015**. [Online]. Available: https://doi.org/10.1016/j.softx.2015.06.001

[104] O. Berger, O. Edholm, and F. Jähnig, "Molecular Dynamics Simulations of a Fluid Bilayer of Dipalmitoylphosphatidylcholine at Full Hydration, Constant Pressure, and Constant Temperature," *Biophysical Journal*, vol. 72, pp. 2002–13, **1997**. [Online]. Available: https://doi.org/10.1016/S0006-3495(97)78845-3

[105] H. J. C. Berendsen, J. R. Grigera, and T. P. Straatsma, "The missing term in effective pair potentials," *The Journal of Physical Chemistry*, vol. 91, pp. 6269–6271, **1987**. [Online]. Available: https://doi.org/10.1021/j100308a038

[106] E. Schneck, D. Horinek, and R. R. Netz, "Insight into the Molecular Mechanisms of Protein Stabilizing Osmolytes from Global Force-Field Variations," *The Journal of Physical Chemistry B*, vol. 117, pp. 8310–8321, **2013**. [Online]. Available: https://doi.org/10.1021/jp400790f

[107] S. Weerasinghe and P. E. Smith, "A Kirkwood-Buff Derived Force Field for Mixtures of Urea and Water," *The Journal of Physical Chemistry B*, vol. 107, pp. 3891–3898, **2003**. [Online]. Available: https://doi.org/10.1021/jp022049s

[108] L. X. Dang, "Mechanism and Thermodynamics of Ion Selectivity in Aqueous Solutions of 18-Crown-6 Ether: A Molecular Dynamics Study," *Journal of the American Chemical Society*, vol. 117, pp. 6954–6960, **1995**. [Online]. Available: https://doi.org/10.1021/ja00131a018

[109] J. B. Klauda, R. M. Venable, J. A. Freites, J. W. O'Connor, D. J. Tobias, C. Mondragon-Ramirez, I. Vorobyov, A. D. MacKerell, and R. W. Pastor, "Update of the CHARMM All-Atom Additive Force Field for Lipids: Validation on Six Lipid Types," *The Journal of Physical Chemistry B*, vol. 114, pp. 7830–7843, **2010**. [Online]. Available: https://doi.org/10.1021/jp101759q

[110] R. M. Venable, Y. Luo, K. Gawrisch, B. Roux, and R. W. Pastor, "Simulations of Anionic Lipid Membranes: Development of Interaction-Specific Ion Parameters and Validation Using NMR Data," *The Journal of Physical Chemistry B*, vol. 117, pp. 10 183–10 192, **2013**. [Online]. Available: https://doi.org/10.1021/jp401512z

[111] W. L. Jorgensen, J. Chandrasekhar, J. D. Madura, R. W. Impey, and M. L. Klein, "Comparison of simple potential functions for simulating liquid water," *The Journal of Chemical Physics*, vol. 79, pp. 926–935, **1983**. [Online]. Available: https://doi.org/10.1063/1.445869

[112] S. R. Durell, B. R. Brooks, and A. Ben-Naim, "Solvent-Induced Forces between Two Hydrophilic Groups," *The Journal of Physical Chemistry*, vol. 98, pp. 2198–2202, **1994**. [Online]. Available: https://doi.org/10.1021/j100059a038

[113] G. Bussi, D. Donadio, and M. Parrinello, "Canonical sampling through velocity rescaling," *Journal of Chemical Physics*, vol. 126, p. 014101, **2007**. [Online]. Available: https://doi.org/10.1063/1.2408420

[114] H. J. C. Berendsen, J. P. M. Postma, W. F. van Gunsteren, A. DiNola, and J. R. Haak, "Molecular dynamics with coupling to an external bath," *The Journal of Chemical Physics*, vol. 81, pp. 3684–3690, **1984**. [Online]. Available: https://doi.org/10.1063/1.448118

[115] T. Darden, D. York, and L. Pedersen, "Particle mesh Ewald: An N·log(N) method for Ewald sums in large systems," *The Journal of Chemical Physics*, vol. 98, pp. 10 089–10 092, **1993**. [Online]. Available: https://doi.org/10.1063/1.464397

[116] B. Widom, "Some Topics in the Theory of Fluids," *The Journal of Chemical Physics*, vol. 39, p. 2808, **1963**. [Online]. Available: https://doi.org/10.1063/1.1734110

[117] C. H. Bennett, "Efficient estimation of free energy differences from Monte Carlo data," *Journal of Computational Physics*, vol. 22, pp. 245–268, **1976**. [Online]. Available: https://doi.org/10.1016/0021-9991(76)90078-4

[118] T.-Y. Lin and S. N. Timasheff, "Why do some organisms use a urea-methylamine mixture as osmolyte? Thermodynamic compensation of urea and trimethylamine N-oxide interactions with protein," *Biochemistry*, vol. 33, pp. 12 695–12 701, **1994**. [Online]. Available: https://doi.org/10.1021/bi00208a021

[119] L. J. Lis, M. McAlister, N. Fuller, R. P. Rand, and V. A. Parsegian, "Interactions between neutral phospholipid bilayer membranes." *Biophysical Journal*, vol. 37, pp. 657–665, **1982**. [Online]. Available: https://www.ncbi.nlm.nih.gov/pmc/articles/PMC1328851/

[120] A. Schlaich, B. Kowalik, M. Kanduč, E. Schneck, and R. R. Netz, "Physical mechanisms of the interaction between lipid membranes in the aqueous environment," *Physica A: Statistical Mechanics and its Applications*, vol. 418, pp. 105–125, **2015**. [Online]. Available: https://doi.org/10.1016/j.physa.2014.06.088

[121] R. A. Böckmann, A. Hac, T. Heimburg, and H. Grubmüller, "Effect of Sodium Chloride on a Lipid Bilayer," *Biophysical Journal*, vol. 85, pp. 1647–1655, **2003**. [Online]. Available: https://doi.org/10.1016/S0006-3495(03)74594-9

[122] A. Catte, M. Girych, M. Javanainen, C. Loison, J. Melcr, M. S. Miettinen, L. Monticelli, J. Määttä, V. S. Oganesyan, O. H. S. Ollila, J. Tynkkynen, and S. Vilov, "Molecular electrometer and binding of cations to phospholipid bilayers," *Physical Chemistry Chemical Physics*, vol. 18, pp. 32 560–32 569, **2016**. [Online]. Available: https://doi.org/10.1039/C6CP04883H

[123] E. S. Courtenay, M. W. Capp, C. F. Anderson, and M. T. Record, "Vapor Pressure Osmometry Studies of Osmolyte-Protein Interactions: Implications for the Action of Osmoprotectants in Vivo and for the Interpretation of "Osmotic Stress" Experiments in Vitro," *Biochemistry*, vol. 39, pp. 4455–4471, **2000**. [Online]. Available: https://doi.org/10.1021/bi992887l

[124] R. H. Stokes, "Thermodynamics of Aqueous Urea Solutions," *Australian Journal of Chemistry*, vol. 20, pp. 2087–2100, **1967**. [Online]. Available: https://doi.org/10.1071/CH9672087

[125] A. Lang, "Osmotic coefficients and water potentials of sodium chloride solutions from 0 to 40C," *Australian Journal of Chemistry*, vol. 20, p. 2017, **1967**. [Online]. Available: https://doi.org/10.1071/CH9672017

[126] N. Kučerka, S. Tristram-Nagle, and J. F. Nagle, "Structure of Fully Hydrated Fluid Phase Lipid Bilayers with Monounsaturated Chains," *Journal of Membrane Biology*, vol. 208, pp. 193–202, **2006**. [Online]. Available: https://doi.org/10.1007/s00232-005-7006-8

[127] G. Pabst, A. Hodzic, J. Štrancar, S. Danner, M. Rappolt, and P. Laggner, "Rigidification of Neutral Lipid Bilayers in the Presence of Salts," *Biophysical Journal*, vol. 93, pp. 2688–2696, **2007**. [Online]. Available: https://doi.org/10.1529/biophysj.107.112615

[128] R. Vácha, S. W. Siu, M. Petrov, R. A. Böckmann, J. Barucha-Kraszewska, P. Jurkiewicz, M. Hof, M. L. Berkowitz, and P. Jungwirth, "Effects of Alkali Cations and Halide Anions on the DOPC Lipid Membrane," *The Journal of Physical Chemistry A*, vol. 113, pp. 7235–7243, **2009**. [Online]. Available: https://doi.org/10.1021/jp809974e

[129] H. I. Petrache, T. Zemb, L. Belloni, and V. A. Parsegian, "Salt screening and specific ion adsorption determine neutral-lipid membrane interactions." *Proceedings of the National Academy of Sciences*, vol. 103, pp. 7982–7, **2006**. [Online]. Available: https://doi.org/10.1073/pnas.0509967103

[130] E. Leontidis, A. Aroti, L. Belloni, M. Dubois, and T. Zemb, "Effects of Monovalent Anions of the Hofmeister Series on DPPC Lipid Bilayers Part II: Modeling the Perpendicular and Lateral Equation-of-State," *Biophysical Journal*, vol. 93, pp. 1591–1607, **2007**. [Online]. Available: https://doi.org/10.1529/biophysj.107.109264

[131] L. Sapir and D. Harries, "Is the depletion force entropic? Molecular crowding beyond steric interactions," *Current Opinion in Colloid and Interface Science*, vol. 20, pp. 3–10, **2015**. [Online]. Available: https://doi.org/10.1016/j.cocis.2014.12.003

[132] A. I. Greenwood, S. Tristram-Nagle, and J. F. Nagle, "Partial molecular volumes of lipids and cholesterol," *Chemistry and Physics of Lipids*, vol. 143, pp. 1–10, **2006**. [Online]. Available: https://doi.org/10.1016/j.chemphyslip.2006.04.002

[133] E. Carafoli, "Calcium signaling: A tale for all seasons," *Proceedings of the National Academy of Sciences*, vol. 99, pp. 1115–1122, **2002**. [Online]. Available: https://doi.org/10.1073/pnas.032427999

[134] X. Shi, Y. Bi, W. Yang, X. Guo, Y. Jiang, C. Wan, L. Li, Y. Bai, J. Guo, Y. Wang, X. Chen, B. Wu, H. Sun, W. Liu, J. Wang, and C. Xu, "Ca2+ regulates T-cell receptor activation by modulating the charge property of lipids," *Nature*, vol. 493, pp. 111–115, **2013**. [Online]. Available: https://doi.org/10.1038/nature11699

[135] S. A. Tatulian, "Binding of alkaline-earth metal cations and some anions to phosphatidylcholine liposomes," *European Journal of Biochemistry*, vol. 170, pp. 413–420, **1987**. [Online]. Available: https://doi.org/10.1111/j.1432-1033.1987.tb13715.x

[136] K. Satoh, "Determination of binding constants of Ca2+, Na+, and Cl- ions to liposomal membranes of dipalmitoylphosphatidylcholine at gel phase by particle electrophoresis," *Biochimica et Biophysica Acta (BBA) - Biomembranes*, vol. 1239, pp. 239–248, **1995**. [Online]. Available: https://doi.org/10.1016/0005-2736(95)00154-U

[137] C. Altenbach and J. Seelig, "Calcium binding to phosphatidylcholine bilayers as studied by deuterium magnetic resonance. Evidence for the formation of a calcium complex with two phospholipid molecules," *Biochemistry*, vol. 23, pp. 3913–3920, **1984**. [Online]. Available: https://doi.org/10.1021/bi00312a019

[138] B. Klasczyk, V. Knecht, R. Lipowsky, and R. Dimova, "Interactions of Alkali Metal Chlorides with Phosphatidylcholine Vesicles," *Langmuir*, vol. 26, pp. 18 951–18 958, **2010**. [Online]. Available: https://doi.org/10.1021/la103631y

[139] K. Makino, T. Yamada, M. Kimura, T. Oka, H. Ohshima, and T. Kondo, "Temperature- and ionic strength-induced conformational changes in the lipid head group region of liposomes as suggested by zeta potential data," *Biophysical Chemistry*, vol. 41, pp. 175–183, **1991**. [Online]. Available: https://doi.org/10.1016/0301-4622(91)80017-L

[140] V. Knecht, Z. A. Levine, and P. T. Vernier, "Electrophoresis of neutral oil in water," *Journal of Colloid and Interface Science*, vol. 352, pp. 223–231, **2010**. [Online]. Available: https://doi.org/10.1016/j.jcis.2010.07.002

[141] H. Egawa and K. Furusawa, "Liposome Adhesion on Mica Surface Studied by Atomic Force Microscopy," *Langmuir*, vol. 15, pp. 1660–1666, **1999**. [Online]. Available: https://doi.org/10.1021/la980923w

[142] F. Pincet, S. Cribier, and E. Perez, "Bilayers of neutral lipids bear a small but significant charge," *The European Physical Journal B*, vol. 11, pp. 127–130, **1999**. [Online]. Available: https://doi.org/10.1007/BF03219162

[143] K. Roger and B. Cabane, "Why Are Hydrophobic/Water Interfaces Negatively Charged?" *Angewandte Chemie International Edition*, vol. 51, pp. 5625–5628, **2012**. [Online]. Available: https://doi.org/10.1002/anie.201108228

[144] A. Maali, R. Boisgard, H. Chraibi, Z. Zhang, H. Kellay, and A. Würger, "Viscoelastic Drag Forces and Crossover from No-Slip to Slip Boundary Conditions for Flow near Air-Water Interfaces," *Physical Review Letters*, vol. 118, p. 084501, **2017**. [Online]. Available: https://doi.org/10.1103/PhysRevLett.118.084501

[145] Y. Uematsu, D. J. Bonthuis, and R. R. Netz, "Charged Surface-Active Impurities at Nanomolar Concentration Induce Jones–Ray Effect," *The Journal of Physical Chemistry Letters*, vol. 9, pp. 189–193, **2018**. [Online]. Available: https://doi.org/10.1021/acs.jpclett.7b02960

[146] Y. Uematsu, D. J. Bonthuis, and R. R. Netz, "Impurity effects at hydrophobic surfaces," *Current Opinion in Electrochemistry*, vol. 13, pp. 166–173, **2019**. [Online]. Available: https://doi.org/10.1016/j.coelec.2018.09.003

[147] T. T. Duignan and X. S. Zhao, "Impurities Limit the Capacitance of Carbon-Based Supercapacitors," *The Journal of Physical Chemistry C*, vol. 123, pp. 4085–4093, **2019**. [Online]. Available: https://doi.org/10.1021/acs.jpcc.8b12031

[148] A. P. Carpenter, E. Tran, R. M. Altman, and G. L. Richmond, "Formation and surface-stabilizing contributions to bare nanoemulsions created with negligible surface charge," *Proceedings of the National Academy of Sciences*, vol. 116, pp. 9214–9219, **2019**. [Online]. Available: https://doi.org/10.1073/pnas.1900802116

[149] V. Knecht, B. Klasczyk, and R. Dimova, "Macro- versus Microscopic View on the Electrokinetics of a Water–Membrane Interface," *Langmuir*, vol. 29, pp. 7939–7948, **2013**. [Online]. Available: https://doi.org/10.1021/la400342m

[150] D. J. Bonthuis, S. Gekle, and R. R. Netz, "Profile of the Static Permittivity Tensor of Water at Interfaces: Consequences for Capacitance, Hydration Interaction and Ion Adsorption," *Langmuir*, vol. 28, pp. 7679–7694, **2012**. [Online]. Available: https://doi.org/10.1021/la2051564

[151] A. A. Kornyshev, W. Schmickler, and M. A. Vorotyntsev, "Nonlocal electrostatic approach to the problem of a double layer at a metal-electrolyte interface," *Physical Review B*, vol. 25, pp. 5244–5256, **1982**. [Online]. Available: https://doi.org/10.1103/PhysRevB.25.5244

[152] D. J. Bonthuis, D. Horinek, L. Bocquet, and R. R. Netz, "Electrokinetics at Aqueous Interfaces without Mobile Charges," *Langmuir*, vol. 26, pp. 12 614–12 625, **2010**. [Online]. Available: https://doi.org/10.1021/la9034535

[153] C. Malmberg and A. Maryott, "Dielectric constant of water from 0 to 100 C," *Journal of Research of the National Bureau of Standards*, vol. 56, p. 1, **1956**. [Online]. Available: https://doi.org/10.6028/jres.056.001

[154] K. E. Bett and J. B. Cappi, "Effect of Pressure on the Viscosity of Water," *Nature*, vol. 207, pp. 620–621, **1965**. [Online]. Available: https://doi.org/10.1038/207620a0

[155] R. R. Netz, D. Jan Bonthuis, and Y. Uematsu, "Interfacial layer effects on surface capacitances and electro-osmosis in electrolytes," *Philosophical Transactions of the Royal Society A: Mathematical, Physical and Engineering Sciences*, vol. 374, p. 20150033, **2016**. [Online]. Available: https://doi.org/10.1098/rsta.2015.0033

[156] Y. Uematsu, R. R. Netz, and D. J. Bonthuis, "Analytical Interfacial Layer Model for the Capacitance and Electrokinetics of Charged Aqueous

Interfaces," *Langmuir*, vol. 34, pp. 9097–9113, **2018**. [Online]. Available: https://doi.org/10.1021/acs.langmuir.7b04171

[157] E. Hawlicka, "Self-Diffusion of Sodium, Chloride and Iodide Ions in Acetonitrile-Water Mixtures," *Zeitschrift für Naturforschung A*, vol. 42, pp. 1014–1016, **1987**. [Online]. Available: https://doi.org/10.1515/zna-1987-0915

[158] P. Loche, C. Ayaz, A. Schlaich, D. J. Bonthuis, and R. R. Netz, "Breakdown of Linear Dielectric Theory for the Interaction between Hydrated Ions and Graphene," *The Journal of Physical Chemistry Letters*, vol. 9, pp. 6463–6468, **2018**. [Online]. Available: https://doi.org/10.1021/acs.jpclett.8b02473

[159] P. Loche, C. Ayaz, A. Wolde-Kidan, A. Schlaich, and R. R. Netz, "Universal and Nonuniversal Aspects of Electrostatics in Aqueous Nanoconfinement," *The Journal of Physical Chemistry B*, vol. 124, p. 4365–4371, **2020**. [Online]. Available: https://doi.org/10.1021/acs.jpcb.0c01967

[160] D. J. Price and C. L. Brooks, "A modified TIP3P water potential for simulation with Ewald summation," *The Journal of Chemical Physics*, vol. 121, pp. 10 096–10 103, **2004**. [Online]. Available: https://doi.org/10.1063/1.1808117

[161] A. Schlaich, E. W. Knapp, and R. R. Netz, "Water Dielectric Effects in Planar Confinement," *Physical Review Letters*, vol. 117, p. 048001, **2016**. [Online]. Available: https://doi.org/10.1103/PhysRevLett.117.048001

[162] M. A. González and J. L. F. Abascal, "The shear viscosity of rigid water models," *The Journal of Chemical Physics*, vol. 132, p. 096101, **2010**. [Online]. Available: https://doi.org/10.1063/1.3330544

[163] C. Sendner, D. Horinek, L. Bocquet, and R. R. Netz, "Interfacial Water at Hydrophobic and Hydrophilic Surfaces: Slip, Viscosity, and Diffusion," *Langmuir*, vol. 25, pp. 10 768–10 781, **2009**. [Online]. Available: https://doi.org/10.1021/la901314b

[164] A. Schlaich, J. Kappler, and R. R. Netz, "Hydration Friction in Nanoconfinement: From Bulk via Interfacial to Dry Friction," *Nano Letters*, vol. 17, pp. 5969–5976, **2017**. [Online]. Available: https://doi.org/10.1021/acs.nanolett.7b02000

[165] J. Lyklema, S. Rovillard, and J. De Coninck, "Electrokinetics: The Properties of the Stagnant Layer Unraveled," *Langmuir*, vol. 14, pp. 5659–5663, **1998**. [Online]. Available: https://doi.org/10.1021/la980399t

[166] A. Crespy, A. Bolève, and A. Revil, "Influence of the Dukhin and Reynolds numbers on the apparent zeta potential of granular porous media," *Journal of Colloid and Interface Science*, vol. 305, pp. 188–194, **2007**. [Online]. Available: https://doi.org/10.1016/j.jcis.2006.09.038

[167] S. Li, P. Leroy, F. Heberling, N. Devau, D. Jougnot, and C. Chiaberge, "Influence of surface conductivity on the apparent zeta potential of calcite," *Journal of Colloid and Interface Science*, vol. 468, pp. 262–275, **2016**. [Online]. Available: https://doi.org/10.1016/j.jcis.2016.01.075

[168] A. Schlaich, A. P. dos Santos, and R. R. Netz, "Simulations of Nanoseparated Charged Surfaces Reveal Charge-Induced Water Reorientation and Nonadditivity of Hydration and Mean-Field Electrostatic Repulsion," *Langmuir*, vol. 35, pp. 551–560, **2019**. [Online]. Available: https://doi.org/10.1021/acs.langmuir.8b03474

[169] P. Maity, B. Saha, G. S. Kumar, and S. Karmakar, "Effect of counterions on the binding affinity of Na+ ions with phospholipid membranes," *RSC Advances*, vol. 6, pp. 83 916–83 925, **2016**. [Online]. Available: https://doi.org/10.1039/C6RA17056K

[170] M. Předota, M. L. Machesky, and D. J. Wesolowski, "Molecular Origins of the Zeta Potential," *Langmuir*, vol. 32, pp. 10 189–10 198, **2016**. [Online]. Available: https://doi.org/10.1021/acs.langmuir.6b02493

[171] Z. Brkljača, D. Namjesnik, J. Lützenkirchen, M. Předota, and T. Preočanin, "Quartz/Aqueous Electrolyte Solution Interface: Molecular Dynamic Simulation and Interfacial Potential Measurements," *The Journal of Physical Chemistry C*, vol. 122, pp. 24 025–24 036, **2018**. [Online]. Available: https://doi.org/10.1021/acs.jpcc.8b04035

[172] D. Biriukov, P. Fibich, and M. Předota, "Zeta Potential Determination from Molecular Simulations," *The Journal of Physical Chemistry C*, vol. 124, pp. 3159–3170, **2020**. [Online]. Available: https://doi.org/10.1021/acs.jpcc.9b11371

[173] P. Mark and L. Nilsson, "Structure and dynamics of liquid water with different long-range interaction truncation and temperature control methods in molecular dynamics simulations," *Journal of Computational Chemistry*, vol. 23, pp. 1211–1219, **2002**. [Online]. Available: https://doi.org/10.1002/jcc.10117

[174] A. Melcrová, S. Pokorna, S. Pullanchery, M. Kohagen, P. Jurkiewicz, M. Hof, P. Jungwirth, P. S. Cremer, and L. Cwiklik, "The complex nature of calcium cation interactions with phospholipid bilayers," *Scientific Reports*, vol. 6, p. 38035, **2016**. [Online]. Available: https://doi.org/10.1038/srep38035

Abstract

The properties of biological interfaces play a role in all processes where organisms interact with their environment. The mucus barrier encountered in higher organisms is a prominent example of such an interface and regulates passage of nutrients and pathogens. On a molecular level, cellular membranes composed of lipid bilayers represent another fundamental biological interface, which is almost always in contact with solutions containing ions or other solutes. This thesis studies the properties of these two interfaces and the interactions with their environment.

First, the barrier properties of an uncharged mucus analogous hydrogel are analyzed based on non-normalized experimental concentration profiles of penetrating tracer molecules. For this, a numerical model of the diffusion process is developed that allows for the extraction of diffusion constants of the tracer particles in the bulk solution and in the hydrogel, as well as free energy differences from which partition coefficients are computed. The computational extraction method is validated by comparison of the obtained diffusion constants with results from experiments and with scaling laws from polymer theory. Based on the extracted partition coefficients a free volume model is developed, which takes into account the tracer and hydrogel flexibility. The model suggests a broad pore size distribution of the unordered hydrogel, in which the larger pores are found to predominantly determine the partitioning process, a phenomenon which might be general to unordered biological hydrogels like mucus.

The second part of this thesis covers the interactions of lipid bilayers in contact with solutions containing different co-solutes or ions, which are analyzed using atomistic molecular dynamics simulations. The *hydration repulsion* of lipid bilayers, commonly observed for nanometer separations, is found to be universally increased by the presence of co-solutes. This effect is quantitatively reproduced from experiments, thus validating the modeling approach. The added repulsion is in a next step modeled as an osmotic pressure afforded by the co-solutes and further augmented by the incorporation of solute-solute and solute-lipid interactions. Finally, ionic adsorption to the lipid interface is investigated in detail by computation of the surface potential obtained from a combination of equilibrium and non-equilibrium simulations in the presence of an electric field. By developing an electrostatic continuum model, which additionally incorporates the presence of minute amounts of negatively charged surface active impurities, initially counterintuitive experimental data is unified for the first time with simulation results. The assumption of contaminations existing in experiments has previously explained a range of other puzzling surface properties and is found to also allow for in detail modeling of electrophoresis experiments on lipid bilayers in ionic solutions.

Zusammenfassung

Die Eigenschaften von biologischen Grenzflächen spielen bei allen Prozessen eine Rolle, bei denen Organismen mit ihrer Umwelt interagieren. Die Barriere der Schleimhaut in höher entwickelten Organismen, welche die Aufnahme von Nährstoffen reguliert und Krankheitserreger abhält, ist ein bekanntes Beispiel für eine solche Grenzfläche. Auf molekularer Ebene stellen Zellmembranen, die aus Lipiddoppelschichten bestehen und meist umgeben von Lösungen sind, eine weitere fundamentale biologische Grenzfläche dar. In dieser Arbeit werden die Eigenschaften dieser beiden Grenzflächen und die Wechselwirkungen mit ihren Umgebungen untersucht.

Im ersten Teil werden die Barriereeigenschaften eines ungeladenen Hydrogels anhand von experimentell gemessenen Tracer-Konzentrationsprofilen untersucht. Hierfür wird zunächst ein numerisches Modell des Diffusionsprozesses entwickelt, welches die Bestimmung von Partitionskoeffizienten sowie Diffusionskonstanten der Tracerpartikel in der Lösung und im Hydrogel ermöglicht. Nach Validierung der Methode, wird, basierend auf den extrahierten Partitionskoeffizienten, ein Modell für die Verteilung der Tracermoleküle konzipiert. Dieses Modell deutet auf eine breite Verteilung der Porengrößen im Hydrogel hin, wobei die größeren Poren entscheidender für die Partitionierung zu seien scheinen. Diese Beobachtung könnte auch für andere ungeordnete biologische Hydrogele wie Schleim zutreffen.

Im zweiten Teil dieser Arbeit werden mit Hilfe von atomistischen Molekulardynamiksimulationen die Wechselwirkungen von Lipiddoppelschichten in Lösungen, die verschiedene Co-Solute oder Ionen enthalten, untersucht. Es stellt sich heraus, dass die Hydratationsabstoßung von Lipiddoppelschichten, durch die Anwesenheit von Co-Soluten generell erhöht wird. Diese zusätzliche Abstoßung wird in einem nächsten Schritt als Solutspezifischer osmotischer Druck modelliert und durch die Einbeziehung von Solut-Solut- und Solut-Lipid-Wechselwirkungen weiter präzisiert. Schlussendlich wird die Ionenadsorption an der Lipidgrenzfläche mittels Berechnung des Oberflächenpotentials, welches aus einer Kombination von Gleichgewichts–und Nicht–Gleichgewichtssimulationen in Gegenwart eines elektrischen Feldes bestimmt wird, analysiert. Durch die Entwicklung eines elektrostatischen Kontinuumsmodells, das zusätzlich die Anwesenheit kleinster Mengen negativ geladener, oberflächenaktiver Verunreinigungen mit einbezieht, werden bis dato kontraintuitive experimentelle Daten mit unseren Simulationsergebnissen vereinheitlicht. Die Annahme von in Experimenten vorhandenen Verunreinigungen hat bereits eine Reihe anderer rätselhafter Oberflächeneigenschaften erklärt und ermöglicht nun auch eine detaillierte Beschreibung von Elektrophorese-Experimenten an Lipiddoppelschichten.

Selbstständigkeitserklärung

Hiermit erkläre ich gegenüber der Freien Universität Berlin, dass ich in der vorliegenden Dissertationsschrift mit dem Titel

Solutes and Ions at Biological Interfaces: Interactions and Kinetics

die Vorgaben guter wissenschaftlicher Praxis gemäß der Empfehlung der Konferenz der Fachbereiche Physik der Freien Universität Berlin eingehalten habe. Ich erkläre, dass ich die vorliegende Dissertationsschrift selbständig angefertigt und hierfür keine anderen als die angegebenen Hilfsmittel und Quellen verwendet habe. Die Arbeit ist frei von Plagiaten. Alle Ausführungen, die wörtlich oder inhaltlich aus anderen Schriften entnommen sind, habe ich als solche kenntlich gemacht. Diese Dissertation wurde in gleicher oder ähnlicher Form noch in keinem früheren Promotionsverfahren eingereicht. Mit einer Prüfung meiner Arbeit durch ein Plagiatsprüfungsprogramm erkläre ich mich einverstanden.

Berlin, den 23. Oktober 2021

Name: Wolde-Kidan
Vorname: Amanuel

Danksagung

Ich möchte mich hiermit ausdrücklich bei allen Personen bedanken, die mir beim Anfertigen dieser Doktorarbeit geholfen haben. Insbesondere meinem Doktorvater Prof. Roland Netz gebührt mein Dank für die Betreuung meiner wissenschaftlichen Arbeiten, den mir überlassenen Freiheiten während meiner Forschung, sowie für das Ermöglichen der vielen Kollaborationen mit Forschungsaufenthalten und Konferenzbesuchen im Ausland.

Ich möchte mich ebenfalls bei meinen Koautoren für die angenehme Kooperation und die erfolgreiche Zusammenarbeit bedanken und habe hier besonders die Arbeit mit Prof. Emanuel Schneck, Douwe Bonthuis und Anna Herrmann genossen.

Auch bei allen Mitgliedern der AG Netz möchte ich mich für die kollegiale Arbeitsatmosphäre bedanken und insbesondere Sina Zendehroud, Bernhard Mitterwallner und Anton Klimek danke ich für die freundschaftlichen Momente im Büro, in Zeiten in denen die Arbeit im Home Office noch eine Ausnahme war.

Zu guter Letzt bedanke ich mich bei meiner Familie und meinen Freunden für ihre aufbauenden Worte während der stressigeren Zeiten der Promotion. Ganz besonders danke ich meiner Schwester und meiner Mutter für ihre Unterstützung in all meinen verschiedenen Lebensphasen.